Western Graduate&PostdoctoralStudies

Western University
Scholarship@Western

Electronic Thesis and Dissertation Repository

4-18-2019 10:00 AM

Calculating the Dimensionality of the Brain, and Other Applications of an Optimized Generalized Ising Model in Predicting Brain's Spontaneous Functions

Pubuditha M. Abeyasinghe
The University of Western Ontario

Supervisor
Soddu, Andrea
The University of Western Ontario

Graduate Program in Physics
A thesis submitted in partial fulfillment of the requirements for the degree in Doctor of Philosophy
© Pubuditha M. Abeyasinghe 2019

Follow this and additional works at: https://ir.lib.uwo.ca/etd

Part of the Computational Neuroscience Commons, and the Statistical, Nonlinear, and Soft Matter Physics Commons

Recommended Citation

Abeyasinghe, Pubuditha M., "Calculating the Dimensionality of the Brain, and Other Applications of an Optimized Generalized Ising Model in Predicting Brain's Spontaneous Functions" (2019). *Electronic Thesis and Dissertation Repository*. 6124.
https://ir.lib.uwo.ca/etd/6124

This Dissertation/Thesis is brought to you for free and open access by Scholarship@Western. It has been accepted for inclusion in Electronic Thesis and Dissertation Repository by an authorized administrator of Scholarship@Western. For more information, please contact wlswadmin@uwo.ca.

Abstract

Understanding a system as complex as the human brain is a very demanding task. Directly working with structural and functional neuroimaging data has led to most of the understanding we have gained about the human brain. However, performing only the direct statistical comparisons on the empirical function and the structure does not fully explain the observed long-range functional correlations. Therefore, implementations of mathematical models to gain further understanding of the relationship between the structure and function of the brain is critical. Additionally, spontaneous functions of the brain can only be predicted using computer simulated models; which will be pivotal for studying the patients with accidental brain injuries. Therefore, this research aims to present an optimized computer simulated model not only to further understand the structure-function relationship of the brain, but also to predict the functional changes when anatomy is altered.

Based on prior work, 2-dimensional classical Ising model stands out among the other models in modeling the functions of the brain due to its simplicity. Hence, a 2-dimentional Ising model was simulated on a structural connectome (generalized Ising model) that acts as a proxy for the anatomical connectivity in the brain. Simulations allowed the prediction of functional connectivity using the structure, at criticality. It also enabled the introduction of a novel methodology to calculate the "dimensionality" of the brain. Our results showed the dimensionality of a healthy brain is two when it is defined using the information flow in the brain. Further research illustrated the dependency of dimensionality on the diffusion tractography method used to obtain the structural connectome. It was also concluded that an optimized generalized Ising model has to be simulated using a structural connectome generated by deterministic tractography to acquire the best predictions of empirical function. Additional investigations into a more generalized version of the Ising model—Potts model with different number of spin states—illustrated that increasing the number of spin states does not increase the predictability. It also supported the hypothesis that the model could be simulating the digi-

tal nature of direct neural activity rather than the indirect activity measured by brain imaging.

Keywords: 2D classical Ising model, Generalized Ising model, Structural connectivity, Functional connectivity, Human brain, Structure-function relationship of the brain, Computer simulations, Dimensionality, Tractography, Potts model

Co-Authorship Statement

The three papers that constitute this thesis were co-authored with various collaborators. For all three projects in Chapter 2, 3 and 4, I am the principal author. I wrote all the papers with inputs from my collaborators. The projects were initiated on ideas originating with Dr. Andrea Soddu, who is a co-author. The main MATLAB code that was used for the projects 1 and 2 was generated in our lab and the necessary modifications were done by me. Fortran code that was used for the third project was developed by Dr. Francisco Lima who is also a co-author. My tasks were modifying the numerical code, developing the dimensionality calculation methodology, running simulations, performing calculations, and analyzing the resulting data. Dr. Andrea Soddu helped in the interpretation of the results of all the projects while Dr. Raimundo Costa, who is also a co-author, helped in interpreting the results for the third project. Dr. Marco Aiello and Dr. Carlo Cavaliere performed the imaging data handling, preprocessing and tractography for all the projects and helped with manuscript editing for project 2. Demetrius R de Paula, Sina Khajehabdollahi and Dr. Sree Ram Valluri were involved in manuscript editing for the first project. Dr. Adrian M Oven who is a co-author in all the projects provided partial funding to support this work.

Dedicated to

my mother, Padmakanthi Kahaduwa,

the strongest woman I have ever seen

and I aspire to be!

my father, Wasantha Abeyasignhe,

the one who showed me the power of silent love!

all the teachers I met in my life including

the ones who taught me that the knowledge is power,

the ones who encouraged me to be better than I was yesterday

the ones who inspired me by saying that "I am going to fail!"

Acknowledgments

I am grateful to the Universe for every person and everything it brought upon my life, directing me towards great successes, profound knowledge and all the experiences, good or bad from the very first day of this amazing journey of life.

I am grateful for the support of many people in numerous ways during my graduate studies and throughout my life. Without their help, this day would not have been a success.

First and foremost, I would like to extend my heartfelt gratitude towards my supervisor, Dr. Andrea Soddu for the immense guidance, support, encouragement and care he has shown since the day I started my graduate studies at Western. He was there to support me when I was in doubt and he was there to applause at every little bit of my success throughout the past six years. Under his supervision, I learned how to be successful in my professional life, and also how to accept my mistakes, learn from them and not to be any tougher on myself than I should. During the time I spend in his group, I learned an uncountable number of life lessons that let me push my boundaries to lengths that I had never imagined before. I am forever in debt to Andrea for the changes, improvements, experiences I was exposed to in my life during the time at Western which were only possible because he accepted me as a graduate student. Only second to my immediate family, he is the main person who shaped me to be who I am today. A single word can't express my gratitude, but *Grazie* Andrea. I must say that it was a privilege to be guided by you. Besides my supervisor, I would like to thank the rest of my advisory committee for their great advices and invaluable support. Thank you for all the discussions we had during meetings to improve the quality of my work.

Furthermore, I would like to express my sincere gratitude towards all of our collaborators who have helped me, especially in preprocessing the brain imaging data (Dr. Marco Aiello and Dr. Carlo Cavaliere) and manuscript editing. I would also like to extend my appreciation to the internship advisers and collaborators in Brazil (Dr. Raimundo de Costa) as well as in Netherlands (Dr. Christian Beckmann and Dr. Llera Arenas (Alberto)) for dedicating invaluable time

and resources to share their knowledge with me. I would also like to thank our group members, present and former (Dr. Tushar Das, Demetrius R Paula, Marwa Dewage, Sina Khajehabdollahi, Nasim Mortza and Sivayini Kandeepan). Thank you for all of your fruitful discussions which were very helpful in improving my work further, and also thank you for the inspiration you all have given me in many different ways.

Moreover, I would like to convey a special thanks to my best friend back home, Maheshi, for being beside me through thick and thin despite the thousands of miles between us. Also, I extend my sincere gratitude towards my other best friend who is also my research partner, Siva for trying to play the roles of my parents and my sister as close as possible, and for being my best friend, my shoulder to cry on, all at once. I would especially like to thank the two of you for showing me the true meaning of the saying *"family is not defined only by last name or by blood; it's defined by commitment and by love"*.

My gratitude is extended further to all of my Sri Lankan friends in London for playing their parts in my journey during the past couple of years. A special thanks goes to everyone in the Physics and Astronomy family, for all the support provided throughout my journey.

Finally, I would like to convey my gratitude towards my family for accepting me for who I am and for being close to my heart every step of the way. Amma (mother) and Thaththa (father) thank you for giving me the chance to see the lights of this world. Thank you for all the sacrifices you made and the hard work you put into building a wonderful future for us. Most importantly, thank you for bringing us up to be good human beings above everything else. Further, I would like to thank my sister, the best listener and the critic in my life, for making sure that I felt her presence even though we were thousands of miles apart. She is someone who can hear everything I don't say. Akka (sister), I am forever grateful to you for being the best big sister I could ask for. I would also like to thank my two brothers, the eldest brother for all the enthusiasm shown and encouragement provided for my work even for my slightest success, and the second elder brother for making me realize the true meaning of life. I would also like to thank one of my biggest fans of all time, my adorable nephew, for reminding me

every day that he is going to look up to me when he is in need of inspiration to do great things in his life. I would especially like to thank the love of my life, my other biggest fan, for seeing something in me that even I could not see. You are encouraging me to expand my boundaries with great enthusiasm and immense love every single day. Thank you for all your love, care, support and the understanding.

Contents

Abstract ii

Co-Authorship Statement v

Acknowledgements vii

List of Figures xv

List of Tables xxiv

1 Introduction 1

1.1 Fundamentals 2

1.1.1 Neurons 2

1.1.2 Connectivity 4

Structural connectivity 5

Functional connectivity 5

1.2 Magnetic Resonance Imaging (MRI) 6

1.2.1 Diffusion Tensor Imaging (DTI) 6

1.2.2 Resting State Functional Magnetic Resonance Imaging (rs-fMRI) . . . 7

1.3 Mathematical modelling 9

1.3.1 Simulating the 2D classical Ising model 11

1.3.2 Simulating the generalized Ising model 13

1.4 "Dimensionality" of the brain 14

1.5 Chapter preview 18

Bibliography **20**

2 Role of Dimensionality in Predicting the Spontaneous Behavior of the Brain using the Classical Ising Model and the Ising Model Implemented on the Structural Connectome **26**

2.1 Introduction 26

2.2 Materials and methods 30

2.2.1 Acquisition and preprocessing of data 30

Subjects 30

Ethic statement 30

Acquisition and preprocessing of data 30

2.2.2 2D Ising Model and the generalized Ising model 31

Computer simulations 31

2.2.3 Analysis 32

Preliminary analysis 32

Analyzing the behavior at the criticality using the critical exponents . . 33

2.2.4 Results 34

Preliminary analysis 34

2.2.5 Discussion 41

2.2.6 Conclusion 45

Bibliography **46**

3 Deterministic or Probabilistic Tractography? **50**

3.1 Introduction 50

3.1.1 Diffusion tractography 50

3.1.2 Computational modelling 52

3.2 Methodology . . . 55
3.2.1 Data acquisition, preprocessing and tractography . . . 55
Subjects . . . 55
Ethic statement . . . 56
Functional MRI (fMRI) . . . 56
Diffusion MRI . . . 56
3.2.2 Data preparation and simulations . . . 57
Data preparation . . . 57
Model simulations . . . 57
3.2.3 Analysis . . . 58
3.3 Results . . . 59
3.4 Discussion . . . 66
3.5 Conclusion . . . 71

Bibliography **72**

4 Will a Potts Model with q > 2 States Simulated on a Structural Connectome be Able to Better Predict the Spontaneous Fluctuations of the Brain? **79**

4.1 Introduction . . . 79
4.2 Methodology . . . 82
4.2.1 Data acquisition and preprocessing . . . 82
Subjects . . . 82
Ethics statement . . . 82
Acquisition and preprocessing . . . 82
4.2.2 Model simulations . . . 83
4.2.3 Analysis . . . 85
4.3 Results . . . 86
4.4 Discussion . . . 92

4.5 Conclusion 94

Bibliography **96**

5 Discussion and Future Work **100**

5.1 Discussion 100

5.2 Future work 104

5.2.1 Application of the generalized Ising model to patients with brain injuries 105

5.2.2 Dimensionality calculation of any complex network 106

Bibliography **107**

A Appendices: Chapter 2 **111**

A.1 2D Classical Ising model 111

A.2 Critical exponents and scaling relations 115

A.3 Labels of 84 parcellations of the brain 118

A.4 Supplementary figures 120

A.4.1 Distance between the correlation dictributions 120

A.4.2 Inter-subject variance of T_c and T_{min} 120

A.4.3 Further study of the difference in T_c 121

A.4.4 Global degree as a function of temperature 123

Bibliography **124**

B Appendices: Chapter 3 **125**

B.1 Calculating the Dimensionality of a System Using the Results of Generalized Ising Model Simulations 125

B.2 Additional Results of the Initial Analysis of Tractography 127

B.3 Additional Results of the RSN analysis 132

Bibliography **137**

C Appendices: Chapter 4 **138**

C.1 Supplementary figures 138

Curriculum Vitae **155**

List of Figures

1.1 (a) Parts of a neuron [5], (b) Axial view of the brain as observed by structural brain imaging 3

1.2 Four different views of the 84 parcellated regions in the brain created by the AAL2 atlas. Each color represents a different region 4

1.3 Hemodynamic response function at the onset of an external stimulus [22] . . . 8

1.4 Representation of a 2D lattice arrangement. The nearest neighbors of the green color lattice site are represented in red 12

1.5 Representation of the equilibrium spin configuration for $T < T_c$, $T = T_c$ and $T > T_c$ for a two-dimensional lattice arrangement. Blue color is for the up spins $(+1)$ and yellow color is for the down spins (-1) 13

1.6 Correlation as a function of distance at the critical temperature for the generalized Ising model 17

2.1 Summarized representation of the analysis carried out. We obtained the structural and functional data separately from brain imaging techniques. Then, the structural connectivity was used as the input of the generalized Ising model. Using this input, the generalized Ising model was simulated for different temperatures and each time the output was compared with the empirical functional data obtained from fMRI 29

2.2 Thermodynamic properties of the 2D classical Ising model with 9×9 lattice size and the generalized Ising model as a function of temperature. Red dashed line indicates the critical temperature and the red solid lines represent the plots after fitting the given equations to calculate the critical exponents 34
2.3 Correlation at four different temperatures for the classical Ising model and the generalized Ising model with the correlation of the empirical data 36
2.4 Distribution of the correlation at four different temperatures for the classical Ising model and the generalized Ising model with the distribution of correlation of the empirical data 37
2.5 Histogram of T_c and T_{min} together with the fitted distributions for the generalized Ising model in 10 independent simulations 37
2.6 Average degree as a function of positive and negative thresholds for the classical Ising model and the generalized Ising model together with the average degree of the empirical correlation network 38
2.7 Connectivity graphs for the generalized Ising model for four temperatures, and the connectivity graph of the empirical network. The size of the nodes represents the degree such that larger the size, higher the degree 39
2.8 Correlation function versus distance and correlation length versus temperature for the 2D classical Ising model and the generalized Ising model. Red solid line represents plots after fitting the given equations (Appendix A.2). In the top panel, the dashed line represents the correlation function at the critical temperature 40
2.9 Energy, specific heat, magnetization, susceptibility, degree, and the cumulative degree of (a) the generalized Ising model and (b) the 2D classical Ising model as a function of temperature 44

3.1 Summarized methodology 55
3.2 Structural connectivity matrices 60

3.3 Summary of the analysis. (a) Average susceptibility as a function of temperature, (b) Distance between the simulated correlations and the empirical correlation as a function of temperature, (c) Correlation coefficient between the simulated correlations and the empirical correlations as a function of temperature, (d) (e) (f) (h) matrix representations of the correlation at T_c, T_{min} and T_{max} and empirical correlation respectively, (g) distribution of T_c, T_{min} and T_{max} within the group of 69 subjects 61

3.4 Average correlation coefficients (without using any threshold) between the simulated data (at Tc, Tmin and Tmax) and the empirical functional connectivity along with the correlation coefficient between the empirical structural connectivity and the empirical functional connectivity. * = 0.01< p < 0.05, ** = 0.001 < p < 0.01 and *** = p < 0.001 63

3.5 Auditory network (AUD), Sensorimotor network (Sen), Visual lateral and medial networks (VL, VM) obtained from (a) the simulated correlations (at T_c) and (b) the empirical correlations 64

3.6 Default mode network (DMN), Salience network (Sal), External control network left and right (ECNL, ECNR) obtained from (a) the simulated correlations (at T_c) and (b) the empirical correlations 64

3.7 Mean correlation coefficients between the simulated data (at T_c) and the empirical functional connectivity as a function of threshold. Shaded area represents the standard deviation 65

3.8 Dimensionality and sparsity for different tractography methods 66

3.9 Correlation function at T_c as a function of distance for different tractography methods together with their respective dimensionality 67

4.1 Simulated time series for different number of spin states together with the empirical time series. Plots represent the time series of a randomly selected region (40^{th} region for all cases). Number of time points shown (600) are half of the actual number of time points available 81

4.2 Thermodynamic properties for Potts models with different spin states. Red lined in the susceptibility plot indicates the temperature that gives the maximum susceptibility for different simulations 86

4.3 (a) Distance between the simulated and the empirical correlation matrices as a function of temperature (b) correlation between the simulated and the empirical correlation matrices at a function of temperature. Vertical dashed lines represent T_{min} and T_{max} respectively 87

4.4 Correlation matrices at T_c for q = 2, 3, 4, 5, 6, 8 and 10 together with the empirical correlation matrix and the distribution of the correlations of each system with different number of spin states 88

4.5 Simulated time series for left precuneus (yellow) and the left inferior parietal region (blue) (spatial positions are indicated on the brain in left) for seven different simulations along with that of the empirical data. Presented correlations are the correlations between the two time series 89

4.6 Brain maps of the default mode network for the simulated data at T_c for seven different systems together with the brain map of the empirical data 90

4.7 Average time series for the DMN is presented in green while the time series of the region that has the highest correlation with the average time series is presented in orange for all the models and the empirical data 91

4.8 Correlation coefficient between the empirical correlation and the simulated correlations (at T_c, T_{min} and T_{max}) for the Potts models with different number of spin states 92

A.1 Representation of a 2D lattice arrangement. Each lattice site has a spin, either up or down. The nearest neighbours of the green lattice site are represented in red 112

A.2 Representation of the equilibrium spin configuration for (a) $T < T_c$, (b) $T = T_c$ and (c) $T > T_c$ for a two-dimensional lattice arrangement. Red color is for the up spins (+1) and blue color is for the down spins (−1) [3] 114

A.3 Distance between the correlation distributions as a function of temperature for the 2D classical Ising model and the generalized Ising mode. Red vertical line corresponds to the critical temperature T_c 120

A.4 Distribution of T_c and T_{min} for 69 subjects 121

A.5 Structural connectivity matrix of the generalized Ising model, an intermediate structural connectivity and the structural connectivity used for the 2D classical Ising model 122

A.6 Critical temperature versus sparsity of the connectivity matrices. Point A represents the sparsity of the generalized Ising model and point B the 2D classical Ising model 122

A.7 Global degree as a function of temperature for the 2D classical Ising model and the Generalized Ising model. Black horizontal line represents the global degree for the empirical functional connectivity. Red vertical line represents the critical temperature for each case 123

B.1 (a) Average susceptibility as a function of temperature, (b) Distance between the simulated correlations and the empirical correlation as a function of temperature, (c) Correlation coefficient between the simulated correlations and the empirical correlations as a function of temperature, (d) (e) (f) (h) matrix representations of the correlation at T_c, T_{min} and T_{max} and empirical correlation respectively, (g) distribution of T_c, T_{min} and T_{max} within the group of 69 subjects 127

B.2 (a) Average susceptibility as a function of temperature, (b) Distance between the simulated correlations and the empirical correlation as a function of temperature, (c) Correlation coefficient between the simulated correlations and the empirical correlations as a function of temperature, (d) (e) (f) (h) matrix representations of the correlation at T_c, T_{min} and T_{max} and empirical correlation respectively, (g) distribution of T_c, T_{min} and T_{max} within the group of 69 subjects 128

B.3 (a) Average susceptibility as a function of temperature, (b) Distance between the simulated correlations and the empirical correlation as a function of temperature, (c) Correlation coefficient between the simulated correlations and the empirical correlations as a function of temperature, (d) (e) (f) (h) matrix representations of the correlation at T_c, T_{min} and T_{max} and empirical correlation respectively, (g) distribution of T_c, T_{min} and T_{max} within the group of 69 subjects 129

B.4 (a) Average susceptibility as a function of temperature, (b) Distance between the simulated correlations and the empirical correlation as a function of temperature, (c) Correlation coefficient between the simulated correlations and the empirical correlations as a function of temperature, (d) (e) (f) (h) matrix representations of the correlation at T_c, T_{min} and T_{max} and empirical correlation respectively, (g) distribution of T_c, T_{min} and T_{max} within the group of 69 subjects 130

B.5 (a) Average susceptibility as a function of temperature, (b) Distance between the simulated correlations and the empirical correlation as a function of temperature, (c) Correlation coefficient between the simulated correlations and the empirical correlations as a function of temperature, (d) (e) (f) (h) matrix representations of the correlation at T_c, T_{min} and T_{max} and empirical correlation respectively, (g) distribution of T_c, T_{min} and T_{max} within the group of 69 subjects 131

B.6 Auditory network (Aud), Sensorimotor network (Sen), Visual lateral, medial networks (VL, VM) obtained from the simulated (at T_c) and the empirical correlations. RSNs for other tractography methods are presented in Appendix C . . 132

B.7 Default mode network (DMN), Salience network (Sal), External control network left and right (ECNL, ECNR) 132
B.8 Auditory network (Aud), Sensorimotor network (Sen), Visual lateral, medial networks (VL, VM) obtained from the simulated (at T_c) and the empirical correlations. RSNs for other tractography methods are presented in Appendix C . . 133
B.9 Default mode network (DMN), Salience network (Sal), External control network left and right (ECNL, ECNR) 133
B.10 Auditory network (Aud), Sensorimotor network (Sen), Visual lateral, medial networks (VL, VM) obtained from the simulated (at T_c) and the empirical correlations. RSNs for other tractography methods are presented in Appendix C . . 134
B.11 Default mode network (DMN), Salience network (Sal), External control network left and right (ECNL, ECNR) 134
B.12 Auditory network (Aud), Sensorimotor network (Sen), Visual lateral, medial networks (VL, VM) obtained from the simulated (at T_c) and the empirical correlations. RSNs for other tractography methods are presented in Appendix C . . 135
B.13 Default mode network (DMN), Salience network (Sal), External control network left and right (ECNL, ECNR) 135
B.14 Auditory network (Aud), Sensorimotor network (Sen), Visual lateral, medial networks (VL, VM) obtained from the simulated (at T_c) and the empirical correlations. RSNs for other tractography methods are presented in Appendix C . . 136
B.15 Default mode network (DMN), Salience network (Sal), External control network left and right (ECNL, ECNR) 136

C.1 Brain maps for the auditory network from simulated data at T_c for seven models together with the brain map for the empirical data 139
C.2 Average time series for the DMN is presented in green while the time series of the region that has the highest correlation with the average time series is presented in orange for all the models and the empirical data 140

C.3 Brain maps for the executive control network left from simulated data at T_c for seven models together with the brain map for the empirical data 141
C.4 Average time series for the DMN is presented in green while the time series of the region that has the highest correlation with the average time series is presented in orange for all the models and the empirical data 142
C.5 Brain maps for the executive control network right from simulated data at T_c for seven models together with the brain map for the empirical data 143
C.6 Average time series for the DMN is presented in green while the time series of the region that has the highest correlation with the average time series is presented in orange for all the models and the empirical data 144
C.7 Brain maps for the salience network from simulated data at T_c for seven models together with the brain map for the empirical data 145
C.8 Average time series for the DMN is presented in green while the time series of the region that has the highest correlation with the average time series is presented in orange for all the models and the empirical data 146
C.9 Brain maps for the sensorimotor network from simulated data at T_c for seven models together with the brain map for the empirical data 147
C.10 Average time series for the DMN is presented in green while the time series of the region that has the highest correlation with the average time series is presented in orange for all the models and the empirical data 148
C.11 Brain maps for the visual lateral network from simulated data at T_c for seven models together with the brain map for the empirical data 149
C.12 Average time series for the DMN is presented in green while the time series of the region that has the highest correlation with the average time series is presented in orange for all the models and the empirical data 150
C.13 Brain maps for the visual medial network from simulated data at T_c for seven models together with the brain map for the empirical data 151

C.14 Average time series for the DMN is presented in green while the time series of the region that has the highest correlation with the average time series is presented in orange for all the models and the empirical data 152
C.15 Brain maps for the visual occipital network from simulated data at T_c for seven models together with the brain map for the empirical data 153
C.16 Average time series for the DMN is presented in green while the time series of the region that has the highest correlation with the average time series is presented in orange for all the models and the empirical data 154

List of Tables

2.1 Sub-critical, critical and super-critical temperatures of the generalized Ising model and the 2D classical Ising model 35

2.2 Critical exponents and the dimensionality of the 2D classical Ising model and the generalized Ising model 39

3.1 Average T_c, T_{min} and T_{max} for different methods 62

3.2 p - values from the pairwise t-test to compare T_c, T_{min} and T_{max} 62

4.1 Average T_c, T_{min} and T_{max} for different simulations 88

Chapter 1

Introduction

The human brain, one of the most fascinating objects in the universe is home of billions of neurons. Carrying such a large number of neurons creates a platform to have very complex interactions among the neurons. Thus, it's an extremely complex system to study, and, owing to this complexity, we do not yet fully understand most of the human brain's functions. This complexity must be understood before we may be able to answer more fundamental questions of human behavior. As a step towards understanding this complexity, establishing the relationship between the structure and function of the brain is important, and large amounts of research resources have recently been directed to this goal [1, 2].

There are two different approaches to studying the relationship between the structure and function of the human brain. The first uses statistical methods to directly compare the resting state functional connectivity patterns with the structural architecture. Analysis by this method has demonstrated a significant connection between the brain's structure and function [2]. However, this analysis does not fully describe the reasons for the presence of functional correlations between regions which are not structurally connected (large-scale long-range connectivity). In an attempt to explain this behavior, mathematical models have been introduced. In addition to explaining relationships that are identified by statistical methods but not understood, mathematical models can also predict the behavior caused by changes in structure [3]. Computational

modelling allows researchers to perform virtual experiments by controlling input parameter(s) (structural connectivity) to understand the impact of their changes upon output (functional connectivity), in experiments which would be infeasible in reality. For this reason, we are implementing a generalization of the well-known 2-dimensional (2D) Classical Ising model of the human brain, which will be explained in detail in Section 1.3.

The main goal of this thesis is to develop an optimized generalized Ising model which can predict the spontaneous fluctuations of the brain from its underlying structural architecture. Simultaneously, we hope to use the model to better understand the relationship between the anatomical structure and functional connectivity. Furthermore, using the generalized Ising model, we aspire to introduce a novel methodology to calculate the "dimensionality" of the brain's network.

1.1 Fundamentals

1.1.1 Neurons

Being the commanding center of the body, the brain consumes 30% - 50% of the body's energy. This energy is used by billions of neurons within the brain. The *Neuron* is the basic working unit of the brain (Figure 1.1 (a)) and specializes in transmitting information to other types of neurons or cells in the body. As shown in Figure 1.1 (a), a single neuron contains the cell body, axon, axon terminals and dendrites. In human brain, billions of neurons are spatially distributed such that the communication between different regions of the brain through neurons is most efficient [4]. Hence, grey matter—which includes the cell bodies—is located in the outer-most layer of the cortex, while white matter (collection of axons) is located in the inner layer and surrounded by grey matter (Figure 1.1 (b)).

When neurons are excited from an external signal, they release a combination of chemical compounds called *neurotransmitters* from the axon terminals. Neurons that are connected to the axon terminals through the dendrites pick up the modulated signal and passes it on to other

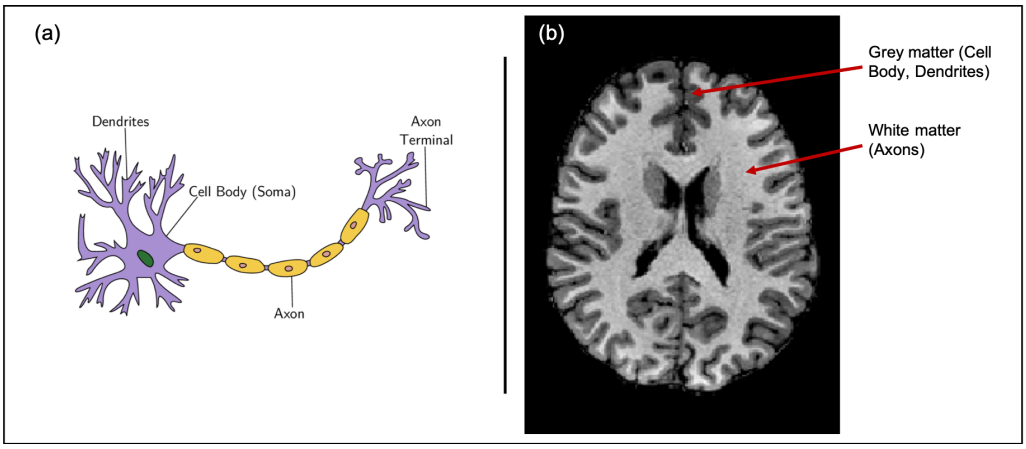

Figure 1.1: (a) Parts of a neuron [5], (b) Axial view of the brain as observed by structural brain imaging

neurons. Characteristics of the signal/spike are embedded in the neurotransmitters and hence different types of signals can be mediated through distinctive types of neurotransmitters to communicate with spatially separated brain regions that are specialized in performing unique tasks [6].

Magnetic resonance imaging does not record brain signals from single neurons, but rather records brain signals per voxel (which is a volumetric pixel). There are hundred thousands of voxels which together cover the whole brain, cortical, and sub-cortical areas. One voxel contains hundreds of neurons, and the observed signal is the average signal over all the neurons in that voxel. Since neurons do not function as individual elements but as collective units which perform sensorimotor and cognitive tasks, voxel-wise imaging data is compatible to explain brain activity. However, performing analysis at the voxel level is time consuming, and the type of the analysis that is being carried out may not require such a large resolution. Hence, the idea of defining non-overlapping regions of interests (ROIs) using prior functional or anatomical information was introduced [7]. Consideration of ROIs instead of single voxels was motivated by the technique itself, in order to reduce the complexity of measuring activity and performing realistic computations. Different parcellation schemes are used at different scales [8]. Work described in this thesis will be based on AAL2 (Automated Anatomical Labelling) parcellation

atlas available in FMRI Software Library (FSL) with 84 ROIs [9] as illustrated in Figure 1.2. A complete list of the 84 regions is presented in Chapter 2, Appendix A.3.

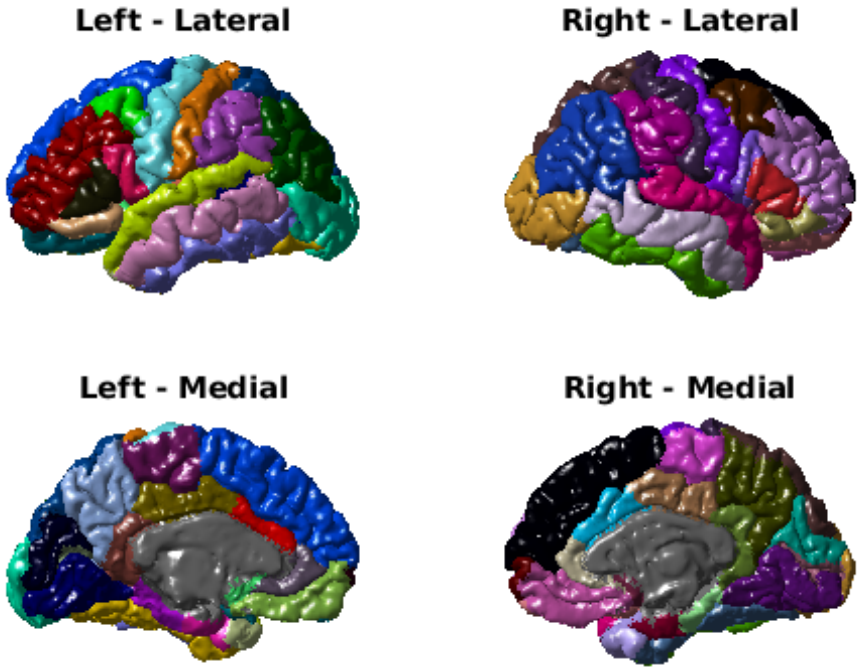

Figure 1.2: Four different views of the 84 parcellated regions in the brain created by the AAL2 atlas. Each color represents a different region

1.1.2 Connectivity

There are three main types of brain connectivity, anatomical/structural connectivity, functional connectivity, and effective connectivity. Functional connectivity and structural connectivity are the two most fundamental connectivity types, while *effective connectivity* refers to the connectivity that depends on causal interactions between the functional and structural connectivity [10]. Of these three connectivity types, the only type that physically exists is structural connectivity, which can be verified via anatomy. In contrast, functional and effective connectivity are statistically defined concepts using observations from brain imaging, but are not present as physical entities.

Structural connectivity

Structural connectivity of the brain refers to brain anatomy or the white matter tracts. It can be obtained using Diffusion Tensor Imaging (DTI), which will be discussed in detail in Section 1.2.1. *White matter* is defined as bundles of axons [11], and it creates a pathway for electrical signals to pass through from one region to another. These pathways inherit different characteristics depending upon the region of the brain in which they are located, the functionality of their brain regions, or even due to individuality. In some situations, while two ROIs are very close to each other spatially, there may be minimal or no anatomical connection at all between them. In other situations, two ROIs can be structurally well connected with many white matter tracts between them, even though the ROIs are spatially far apart.

Functional connectivity

Functional connectivity of the brain refers to the functionally integrated relationship between spatially separated regions. It was introduced to describe the functional strengths between the interactions of ROIs. Analyzing the functional connectivity in the brain helps identify the patterns of correlations between brain signals that are generated due to neural activity. However, the presence of functional connectivity between two ROIs does not necessarily imply that those two regions are directly structurally connected. Functional correlations can arise not only due to the direct structural connections between the origin and the destination regions, but also due to the communication pathways that pass through a number of other regions before travelling from the origin to the destination. Therefore, causal inferences cannot be made using only the functional connectivity [12].

Functional connectivity is measured using either the covariance or the correlations of the signals between brain regions, which can be obtained using functional Magnetic Resonance Imaging (fMRI) (discussed in detail in Section 1.2.2). Correlation provides a quantitative relationship between the variables to indicate how strongly the variables are related. On the other hand, covariance measures the extent to which the variables are varying together. Correlations

among pairs of ROIs are considered in our study, which provides us with a quantitative measure of the relationship between the regions.

1.2 Magnetic Resonance Imaging (MRI)

Magnetic Resonance Imaging (MRI) is a non-invasive medical imaging technique that constructs three-dimensional images of different physiological processes within the body. It was first introduced in neuroscience research to map the brain under stimulations, and has benefited physicians and researches in diagnosing diseases, monitoring the effects of treatments, identifying the causes for pathological situations, and in many other ways. MRI technology has advanced over the years into different types of MRI imaging techniques, which cover a range of imaging modalities serving different purposes and offering improved performance and cost efficiencies.

MRI was further developed using different types of technologies to not only image the structural component of the body, but to also image its spontaneous fluctuations in different physiological processes. DTI and fMRI are two types of such unique techniques that have been developed to image the anatomical structure and the spontaneous fluctuations of the brain, respectively.

1.2.1 Diffusion Tensor Imaging (DTI)

DTI is an imaging technique developed to understand the anatomical structure of the human brain. It is a non-invasive method which allows identification of the location and orientation of white matter in the brain [13, 14, 15] by recording the diffusion of water molecules. It is known that the water molecules in the brain are more prone to move along the axons than across them. Hence, DTI images the diffusion of water molecules to map the connection pathways in the brain.

Mapping the pathways of the brain's communication using these diffusion images has be-

come an important tool in understanding the brain function. It provides a measure of the macroscopic structure of brain tissues, which has initiated the introduction and development of algorithms to compare local diffusion properties in different brains. Different types of statistical algorithms have been used to estimate the pathways followed by white matter fiber tracts. The process of estimating fiber tracts from the images is called "tractography". Probabilistic tractography and deterministic tractography are two basic tractography methods that have been used to estimate the white matter tracts [16]. We investigated the effects of these methods on the estimation of white matter tracts or the structural connectivity, and how these differences affect the generalized Ising model simulations (results are presented in Chapter 3).

1.2.2 Resting State Functional Magnetic Resonance Imaging (rs-fMRI)

fMRI is a non-invasive technique introduced in early 1990s which links brain functions to blood flow in the brain. fMRI has had a significant impact on research in neuroscience. The most common type of fMRI imaging technique is the Blood Oxygen Level Dependent (BOLD) signal. The BOLD signal does not measure the neuronal activity directly; rather, it measures it indirectly through measurements of the ratio of oxygenated and deoxygenated hemoglobin [17, 18, 19]. Basic principle of the BOLD signal is that when the neuronal activity is increased in one region of the brain in response to a stimulus, the cerebral blood flow towards that region is increased. When the cerebral blood flow increases, the level of oxygenated hemoglobin increases relative to deoxygenated hemoglobin in that region. Since oxygenated and deoxygenated hemoglobin have different magnetic properties, changes in the hemoglobin levels of these two types allow the detection of the differences in blood flow using fMRI [20].

Increase in blood flow can also be quantified by the Hemodynamic Response Function (HRF), which shows a spike of intense neural activity and then returns to the stable state once the needs of neural activity are met. The HRF is characterized by a curve that peaks with a time delay of 4-5s compared to the neuronal stimuli (Figure 1.3). It provides the relationship between the BOLD signal and the neural activity. By convolving the HRF with a function

that reflects the theoretically expected neuronal activity, the BOLD signal can be inferred. Moreover, hemodynamic response lasts for a very short period of time, making a direct fMRI measurement impractical [21].

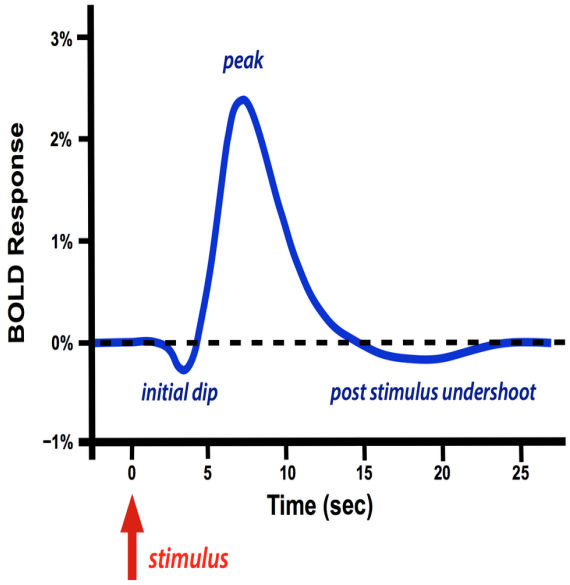

Figure 1.3: Hemodynamic response function at the onset of an external stimulus [22]

rs-fMRI refers to the acquisition of spontaneous brain activity without the presence of any task related stimuli (when the brain is at "rest"). This approach is useful to understand the functional organization of the brain as well as to investigate the alterations in the brain caused by a brain injury or a disorder. The first paper with rs-fMRI was published by Biswal and colleagues [23], where they concluded that the acquired data represent actual brain signals coming from functional networks and not entirely from noise as was believed. Since then, rs-fMRI has become a rapidly growing avenue of studying the spontaneous fluctuations of the brain. In comparison to task-based fMRI, rs-fMRI is convenient from the participant's perspective as well as the researcher's perspective—in both preparing for the experiment and in the analysis—if the objective of the study is not to study a particular functionality of the brain (such as motor or visual activities).

1.3 Mathematical modelling

Computational models of dynamical systems such as the brain allow to estimate quantitative behavior without disturbing biological functions. It also allows us to predict functional changes in any given hypothetical situation. These kinds of studies are very useful in clinical practices as well as in research, in order to gain a better understanding of the functionality of self-organized critical systems such as the brain. Thus, there are several models that are being used to explain the relationship between the structure and function of the brain: these include the Kuramoto model, the neural mass model, and the 2-dimensional classical Ising model.

The Kuramoto model studies the synchronization between neuronal populations that can produce self-sustained oscillations. It has been used to study the dynamics of a cortical network driven by a set of oscillators with their own natural frequencies. These frequencies were assumed to be in gamma-frequency range [24]. Simulations of the model incorporated the structural connectivity of the brain as well as the time delays. Dynamics of the Kuramoto model can be changed by controlling a single parameter—the coupling strengths between the oscillators—which is driven by the structural connectivity. As the coupling strength increases starting from a low value or decreases from a high value, the system experiences a phase transition where it passes through the critical regime [25, 26, 27, 28]. At this criticality the Kuramoto model exhibits behaviors that self-organized systems habitually exhibit without the effect of a controlling parameter, such as the emergence of a power law behavior in the system. Cabral et al. concluded that the resting state brain activity is driven by the slow oscillations of the degree of synchronization in the structural connectivity [24].

Additionally, the neural mass model is also being used to explain the dynamics of the brain. It simulates a system of interconnected excitatory and inhibitory neurons, which are connected through a structural connectivity matrix depicting the firing rate of the neuronal masses. It describes the average activity of subsystems using dynamical state variables such as the mean membrane potential of neuron masses, the average number of inhibitory interneurons, and the open potassium ion channels. In addition to these three main parameters, there

are multiple microscopic quantities that are used to model the dynamics of the neural masses. By studying the evolution of these variables, researchers try to build a relationship between the structure and the function of the brain [29, 30, 31]. Using the neural mass model, it was shown that short range functional networks obtained from neural activity could be predicted using the underlying structural connectivity [30]. Furthermore, it was also observed that there were strong functional connections between regions that are not directly structurally connected. Even though functional connectivity can be explained by part through the direct comparisons [32], it was concluded that inferencing about the complete functional connectivity directly using the structure is unreasonable [29].

In contrast to the neural mass model and the Kuramoto model, 2D classical Ising model is a very simple model with only one controlling parameter: the temperature of the heat bath. When the temperature increases, the system undergoes a phase transition from an ordered phase to a disordered phase passing the critical regime. At the critical temperature it has also been shown to exhibit properties of self-organized criticality including a power low behavior of the functional connectivity as well as a balance between integration and segregation of the system [33]. The 2D classical Ising model—which predicted the global dynamics of the brain function despite having not integrated any information from the brain—was later generalized using the structural connectome of the brain [34, 35, 36, 37].

In [34], Deco et al. generated artificial networks with different coupling strengths and network properties upon which to simulate the Ising model. A comparison between an Ising model implemented on a structural connectome of the brain and on these artificially generated networks via entropy of the system lead to the conclusion that the empirical functional connectivity can be best predicted through the Ising model using a structural connectome that preserves scale free network properties. Further research into generalization of the Ising model explored its ability to predict the empirical functions by estimating information transfer [35]. Marinazzo et al. concluded that the criticality can be characterized by the maximum information transfer in the simulations. Later, Stramaglia et al. [36] also simulated an Ising model on

the structural connectome and compared the differences observed in wakefulness and anesthesia. When the subject is anesthetized, structural connectivity is unchanged while the functional connectivity changes compared to a healthy brain. By observing the simulations of an Ising model to predict the brain activity in anaesthesia, Stramaglia et al. discovered that while the wakefulness can be predicted at the criticality of the model, functions of an anesthetized brain can be predicted at a temperature that is different from the critical temperature.

1.3.1 Simulating the 2D classical Ising model

The 2D Classical Ising model was developed by Ernest Ising [38] to explain the phase transition of ferromagnets at their critical temperatures. It is a very simple model with only one fitting parameter, the temperature, yet by virtue of its simplicity it has been able to capture the battle between integration and segregation in brain functionality [33].

The physical system is represented by a square lattice configuration in the Ising model. Each lattice site has a spin 's' which could take only two possible values, either up (+1) or down (−1) (Figure 1.4). This configuration is kept in a thermal bath of temperature T. Interactions between the spins are always influenced by this temperature and allow the system to reach an equilibrium energy state starting from a random spin configuration, while also yielding different equilibrium spin configurations at different temperatures.

Energy of this spin system at any state x in the absence of an external magnetic field can be calculated using Equation 1.1:

$$E(x) = -J \sum_{\{i,j=1\}}^{N} S_i S_j \tag{1.1}$$

where J is the coupling constant, s_i and s_j represent the spins of the i^{th} and j^{th} sites respectively, and N is the number of lattice sites. Only the nearest neighbor interactions are considered together with equal coupling (J = 1) for 2D Ising model simulations.

At equilibrium, thermodynamic properties such as magnetization (M), magnetic suscepti-

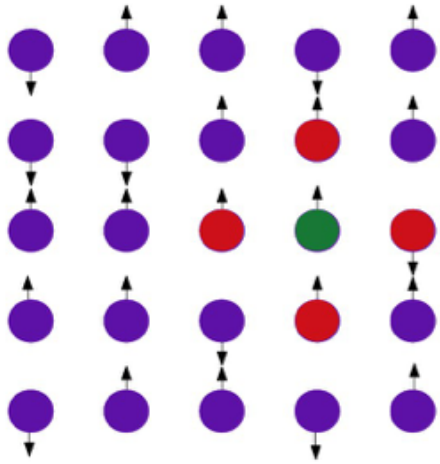

Figure 1.4: Representation of a 2D lattice arrangement. The nearest neighbors of the green color lattice site are represented in red

bility (χ) and the specific heat (C_v) of the system can be calculated using Equations 1.2, 1.3 and 1.4 respectively. Magnetization is simply an order parameter which explains the state of the spin system, which may be in either an ordered state or a disordered state. Magnetic susceptibility is the derivative of magnetization and captures the changes of magnetization. This is used to identify the critical temperature of the spin system by noting the temperature which maximizes the susceptibility. Specific heat tells us how much does the energy of the spin system changes with changing temperature.

$$M = \frac{1}{N}|\sum_{i=1}^{N} S_i| \tag{1.2}$$

$$\chi = \frac{1}{T}[\left\langle M^2 \right\rangle - \langle M \rangle^2] \tag{1.3}$$

$$C_v = \frac{1}{T^2}[\left\langle E^2 \right\rangle - \langle E \rangle^2] \tag{1.4}$$

In a 2D lattice configuration, there are two extreme equilibrium configurations of spins: one for sub-critical temperatures and another for super-critical temperatures. When the tem-

perature is very low (sub-critical), all the spins prefer to be aligned along the same direction (minimizing the energy of the system), with very large clusters of the same spin (ordered) (Figure 1.5 a), resulting in high magnetization. On the other end, when the temperature is very high (super-critical), the spins are a mixture of up spins as well as down spins (disordered) (Figure 1.5 c) which will result in zero magnetization. In between these two extremes, there exists a critical temperature (T_c) where the system exhibits transition from ordered phase to the disordered phase (Figure 1.5 b). Additionally, the system acquires its maximum susceptibility at T_c and even a tiny perturbation introduced by a single spin flip can change the entire system by spreading the effect over the entire configuration rapidly [39, 40]. As described, the system could exhibit completely different properties which depend only upon the temperature of the system.

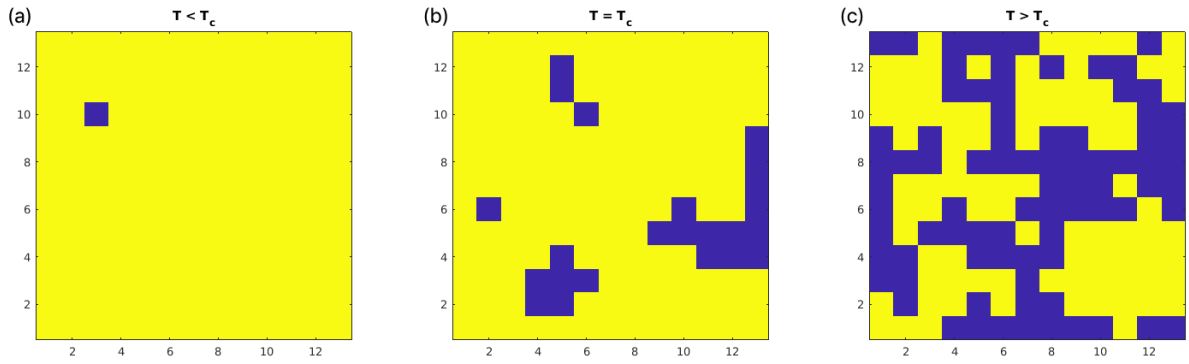

Figure 1.5: Representation of the equilibrium spin configuration for T < T_c, T = T_c and T > T_c for a two-dimensional lattice arrangement. Blue color is for the up spins (+1) and yellow color is for the down spins (−1)

1.3.2 Simulating the generalized Ising model

The generalized Ising model was influenced by the 2D classical Ising model and was introduced by Marinazzo et al. [35]. In our research we are further investigating the use of the generalized Ising model to better predict the relationship between the structure and function of the brain. Generalized Ising model was simulated on a random lattice and we assume that all the spin sites

are interacting with all the other spin sites with different interaction strengths instead of taking only the nearest neighbor coupling (as in the 2D classical Ising model). In the random spin configuration each spin site represents one region of the brain. The interaction strength between the spin sites (or brain regions) is introduced into the model using the structural connectivity of the brain. Therefore, Equation 1.1 changes to Equation 2.1 for the generalized Ising model simulations where J_{ij} represents the coupling strength between the i^{th} and j^{th} sites. Note that the summation is over all regions.

$$E(x) = -\sum_{i,j=1}^{N} J_{ij} S_i S_j \tag{1.5}$$

1.4 "Dimensionality" of the brain

In the mathematicians' point of view, dimensionality refers to a property of space [41] and provides substantial information about how many directions in space we can move. When developing the concept of dimensionality for the brain, one can simply use the general idea of information flow. To balance the integration and segregation, different regions that are specialized in different functions need to keep a steady flow of information or an information flux throughout the brain which can be hypothesized as equivalent to the electric flux due to a point charge in space. In the case of charged particle, electric flux can be calculated using Gauss's law [42] (Equation 1.6) where $\mathbf{E}$ is the electric field, ρ is the charge density and ϵ_0 is the permittivity of space.

$$\int_s \mathbf{E} \cdot d\mathbf{S} = \frac{1}{\epsilon_0} \int_v \rho \, dV \tag{1.6}$$

If a charged particle is in a 2-dimensional space, Equation 1.6 can be simplified to Equation 1.7; while if it is in 3-dimensional space, it can be simplified to Equation 1.8 assuming that the distance r is sufficiently large compared to the size of the point charge. Comparing Equations 1.7 and 1.8, the method to generalize the calculation of electric field for any dimen-

sional space is apparent as illustrated in Equation 1.9, which explains the dependency between the electric field due to a point charge and the dimensions of space where, r is the distance to a point in space from the point charge, Q is the enclosed charge and d is the dimensionality.

$$\begin{aligned} E \cdot 2\pi r &= \frac{Q}{\epsilon_0} \\ E_{2D} &\propto \frac{1}{r} \end{aligned} \tag{1.7}$$

$$\begin{aligned} E \cdot 4\pi r^2 &= \frac{Q}{\epsilon_0} \\ E_{3D} &\propto \frac{1}{r^2} \end{aligned} \tag{1.8}$$

$$\boxed{E \propto \frac{1}{r^{d-1}}} \tag{1.9}$$

When the dimensionality of the space is unknown, it can be easily estimated by measuring and plotting the electric field at different distances and fitting Equation 1.9. In other words, dimensionality of the space will tell us how the electric field due to a point charge will decay in space with respect to the distance. For higher dimensionality, there are substantially more directions in which the field can propagate, resulting in a faster decay. Similar to most of the objects or systems that are in classical existence, the dimensionality of the human brain is three, which is generally defined using its characteristics in physical space. However, when the information transfer in the brain is considered, one can ask if its dimensionality remain three. Can we define dimensionality using the information transfer, considering a phenomena similar to the decay of the electric field of a point charge (rather than the physical characteristics), and do so in a meaningful manner which infers more attributes of the system?

In neuroimaging, most common factor that is involved in any definition of dimensionality is the rate of neural activity or the empirical functionality of the brain that depends upon the rate of neural activity [43, 44, 45, 46]. Since empirical functional connectivity is a time-dependent statistical definition that actually does not exist as a physical quantity, dimensionality of the system will also be time-dependent whilst defined using the functional connectivity. It can

change when the functional connectivity changes, despite the fact that the anatomy of the brain is well defined and time-independent. Therefore, empirical functional connectivity dependency of dimensions is not favorable in establishing a definition for dimensionality which could be used to infer further properties of the brain. Hence, we propose a novel method to calculate the "dimensionality" of the brain via the generalized Ising model that primarily depends only upon the structural connectome.

To calculate the dimensionality, the minimum path length between different pairs of regions in the brain was calculated by defining the distance between regions as in Equation 1.10, where d_{ij} is the distance between the i^{th} and j^{th} region, while J_{ij} is the coupling strength (normalized number of fibers) between the i^{th} and j^{th} region.

$$d_{ij} = \frac{1}{J_{ij}} \tag{1.10}$$

By introducing this concept, distance is defined such that the higher the number of fibers between a pair of regions, the shorter the distance between them even though the two regions may be far apart in physical space. Conversely, however close two regions are in physical space, they can be far apart if there are only a few numbers of fibers between them.

In addition to that, correlation function among brain regions provides a quantitative measure of the similarity of signal forms and can be thought of as equivalent to the electric field as discussed in the example above. Correlation among regions depends upon dimensionality of the space and hence knowing the dimensionality will allow the estimation of correlations. While the empirical functional correlations are obtained using fMRI technique, simulated functional correlations can be obtained from the generalized Ising model, which also depend only on the structural connectome. Simulated functional correlations combined with the concept of distance resulted in a plot which shows the variation of correlation as a function of distance as illustrated in Figure 1.6.

As discussed in [47, 48], correlation can be explained using Equation 1.11 where r is the distance, ξ is the correlation length [48], d is dimensionality, η is the critical exponent of

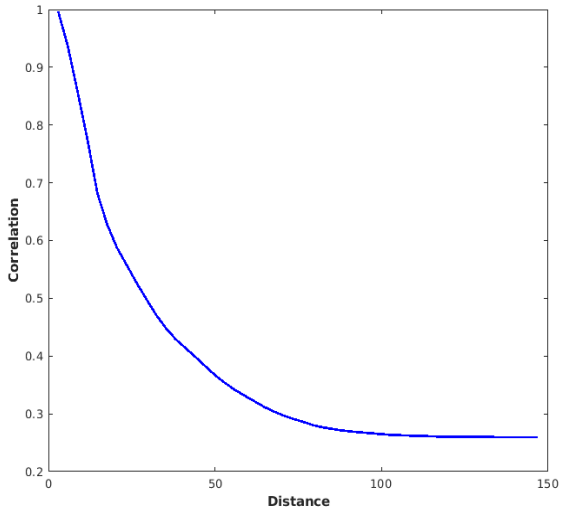

Figure 1.6: Correlation as a function of distance at the critical temperature for the generalized Ising model

correlation length and $P_0 = d - 2 - \eta$, a function of dimensionality and η which then simplifies to Equation 1.12 at the critical temperature. Equation 1.12 can be seen as an equivalent to the form of Equation 1.9 given that $r > \xi$.

$$G(r) \simeq \frac{exp(\frac{-r}{\xi})}{r^{d-2+\eta}} = \frac{exp(\frac{-r}{\xi})}{r^{P_0}} \tag{1.11}$$

$$(@T_c) \quad \boxed{G(r) \simeq \frac{1}{r^{P_0}}} \tag{1.12}$$

Following Equation 1.12 it can be noted that the higher the dimensionality, the faster the decay of correlation with distance, corresponding to the behavior of the electric field as a function of distance in Equation 1.9. Dimensionality captures the essence of information flow in terms of correlations between pairs of regions such that when dimensionality increases, the number of highly correlated nearest neighbors also increases, producing a rapid decay of the correlation function with increasing distance. On the other hand, when dimensionality decreases, the number of highly correlated nearest neighbors decreases while the significance

of correlation between distant neighbors increases, resulting in a slow decay of the correlation. Additionally, dimensionality of the brain also accounts for the inertia between brain regions to exchange information with distant pairs in contrast to the nearest neighbors.

Dimensionality calculated using this method can only be changed due to the changes in the structural connectome, which will change the sampling of distances. In such a situation where the structural connectome changes, simulated functional correlations will also change as the model is driven by the structural connectome. The correspondence between the structural connectome and the simulated function as well as dimensionality provide opportunities to use these relationships to build a tool to better identify and understand the functions not only in a healthy brain, but also in pathological situations.

1.5 Chapter preview

In chapter two (published in *Brain Connectivity* [37]) we compare the 2D classical Ising model and the generalized Ising model, and we present a novel approach to calculate the "dimensionality" of the brain. Our results for the 2D classical Ising model agree with previous work while findings for the generalized Ising model conclude that the dimensionality of the brain is two.

In chapter three (manuscript in preparation for submission to *Brain Structure and Function*) we discuss DTI tractography in order to optimize the generalized Ising model simulations. Six different tractography methods have been studied compared via the generalized Ising model in order to find the best tractography method to be used in the simulations. Our results demonstrated that the deterministic tractography without FA produces the correlation matrix that gives the best prediction of the empirical correlation matrix. It also provides quantitative evidence to illustrate the advantages of using the generalized Ising model to predict the spontaneous fluctuations of the brain using the structural connectome. Additionally, we show the effects of different structural connectome on dimensionality of the brain, which depend on the differences in tractography methods.

In chapter four (manuscript in preparation) we examine a generalized Potts model with seven different cases with different number of spin states as 2, 3, 4, 5, 6, 8 and 10. Since the generalized Ising model has only two state spins and has been able to predict the functional correlation matrix of the brain, it only made sense to see whether we can optimize the model by simulating it with a higher number of spin states than two. The hypothesis tested was that when the number of states increases, the prediction of the empirical functional connectivity matrix will improve. However, we concluded that this is not the case with the generalized Potts model simulations. Furthermore, we concluded that the best prediction of the empirical functional correlation matrix is produced by a 2 state Potts model (or an Ising model) simulated on a structural connectome, which could be due to the fact that the simulations may be predicting the digital nature of direct neural activity rather than the BOLD signal itself as was hypothesized.

Chapter five contains an overall discussion of the thesis together with future research directions. First, we will discuss the applications of an optimized generalized Ising model to patients with brain injuries and how this research will contribute to the improvement of these patients' brain functions. Furthermore, we are generalizing the method of calculating the dimensionality of the brain to calculate dimensionality of any given network given its connectivity structure. We aim to illustrate how this novel approach of calculating dimensionality can be beneficial in any network analysis.

Bibliography

[1] Robert Vianello, Carmen Domene, and Janez Mavri. The use of multiscale molecular simulations in understanding a relationship between the structure and function of biological systems of the brain: the application to monoamine oxidase enzymes. *Frontiers in neuroscience*, 10:327, 2016.

[2] Letícia S Czepielewski, Lei Wang, Clarissa S Gama, and Deanna M Barch. The relationship of intellectual functioning and cognitive performance to brain structure in schizophrenia. *Schizophrenia bulletin*, 43(2):355–364, 2017.

[3] Giuseppe Tenti, Siv Sivaloganathan, and James M Drake. Mathematical modeling of the brain: Principles and challenges. *Neurosurgery*, 62(5):1146–1157, 2008.

[4] Eugene Ludwig and Josef Klingler. *Atlas Serabia Humani: The Inner Structure of the Brain*. Kerger, 1956.

[5] Trevor Bekolay. Learning in large-scale spiking neural networks. Master's thesis, University of Waterloo, 2011.

[6] John G Nicholls, A Robert Martin, Bruce G Wallace, and Paul A Fuchs. *From neuron to brain*, volume 271. Sinauer Associates Sunderland, MA, 2001.

[7] Guillaume Flandin, Ferath Kherif, Xavier Pennec, Denis Riviere, Nicholas Ayache, and J-B Poline. Parcellation of brain images with anatomical and functional constraints for fmri data analysis. In *Biomedical Imaging, 2002. Proceedings. 2002 IEEE International Symposium on*, pages 907–910. IEEE, 2002.

[8] Alan C Evans, Andrew L Janke, Louis Collins, and Sylvain Baillet. Brain templates and atlases. *Neuroimage*, 62(2):911–922, 2012.

[9] Edmund T Rolls, Marc Joliot, and Nathalie Tzourio-Mazoyer. Implementation of a new

parcellation of the orbitofrontal cortex in the automated anatomical labeling atlas. *Neuroimage*, 122:1–5, 2015.

[10] Olaf Sporns. Brain connectivity. *Scholarpedia*, 2(10):4695, 2007.

[11] R Douglas Fields. White matter matters. *Scientific American*, 298(3):54–61, 2008.

[12] Angela D Friederici. The neurobiology of language comprehension. In *Language comprehension: A biological perspective*, pages 265–304. Springer, 1999.

[13] DG Taylor and MC Bushell. The spatial mapping of translational diffusion coefficients by the nmr imaging technique. *Physics in Medicine & Biology*, 30(4):345, 1985.

[14] Denis Le Bihan, Jean-Francois Mangin, Cyril Poupon, Chris A Clark, Sabina Pappata, Nicolas Molko, and Hughes Chabriat. Diffusion tensor imaging: concepts and applications. *Journal of Magnetic Resonance Imaging: An Official Journal of the International Society for Magnetic Resonance in Medicine*, 13(4):534–546, 2001.

[15] Susumu Mori. *Introduction to diffusion tensor imaging*. Elsevier, 2007.

[16] Maxime Descoteaux, Rachid Deriche, Thomas R Knosche, and Alfred Anwander. Deterministic and probabilistic tractography based on complex fibre orientation distributions. *IEEE transactions on medical imaging*, 28(2):269–286, 2009.

[17] Nikos K Logothetis. The underpinnings of the bold functional magnetic resonance imaging signal. *Journal of Neuroscience*, 23(10):3963–3971, 2003.

[18] Nikos K Logothetis. What we can do and what we cannot do with fmri. *Nature*, 453(7197):869, 2008.

[19] Geraint Rees, Karl Friston, and Christof Koch. A direct quantitative relationship between the functional properties of human and macaque v5. *Nature neuroscience*, 3(7):716, 2000.

[20] Scott H Faro and Feroze B Mohamed. *BOLD fMRI: A guide to functional imaging for neuroscientists*. Springer Science & Business Media, 2010.

[21] Karl J Friston, Peter Jezzard, and Robert Turner. Analysis of functional mri time-series. *Human brain mapping*, 1(2):153–171, 1994.

[22] Bold and brain activity. `http://mriquestions.com/does-boldbrain-activity.html`.

[23] Bharat B Biswal. Resting state fmri: a personal history. *Neuroimage*, 62(2):938–944, 2012.

[24] Joana Cabral, Morten L Kringelbach, and Gustavo Deco. Exploring the network dynamics underlying brain activity during rest. *Progress in neurobiology*, 114:102–131, 2014.

[25] Gustavo Deco, Viktor Jirsa, Anthony R McIntosh, Olaf Sporns, and Rolf Kötter. Key role of coupling, delay, and noise in resting brain fluctuations. *Proceedings of the National Academy of Sciences*, pages pnas–0901831106, 2009.

[26] Ruben Schmidt, Karl JR LaFleur, Marcel A de Reus, Leonard H van den Berg, and Martijn P van den Heuvel. Kuramoto model simulation of neural hubs and dynamic synchrony in the human cerebral connectome. *BMC neuroscience*, 16(1):54, 2015.

[27] David Cumin and CP Unsworth. Generalising the kuramoto model for the study of neuronal synchronisation in the brain. *Physica D: Nonlinear Phenomena*, 226(2):181–196, 2007.

[28] Manfred G Kitzbichler, Marie L Smith, Søren R Christensen, and Ed Bullmore. Broadband criticality of human brain network synchronization. *PLoS computational biology*, 5(3):e1000314, 2009.

[29] CJ Honey, Olaf Sporns, Leila Cammoun, Xavier Gigandet, Jean-Philippe Thiran, Reto Meuli, and Patric Hagmann. Predicting human resting-state functional connectivity from

structural connectivity. *Proceedings of the National Academy of Sciences*, 106(6):2035–2040, 2009.

[30] Christopher J Honey, Rolf Kötter, Michael Breakspear, and Olaf Sporns. Network structure of cerebral cortex shapes functional connectivity on multiple time scales. *Proceedings of the National Academy of Sciences*, 104(24):10240–10245, 2007.

[31] Michael Breakspear, John R Terry, and Karl J Friston. Modulation of excitatory synaptic coupling facilitates synchronization and complex dynamics in a biophysical model of neuronal dynamics. *Network: Computation in Neural Systems*, 14(4):703–732, 2003.

[32] Arnaud Messé, David Rudrauf, Habib Benali, and Guillaume Marrelec. Relating structure and function in the human brain: relative contributions of anatomy, stationary dynamics, and non-stationarities. *PLoS computational biology*, 10(3):e1003530, 2014.

[33] Daniel Fraiman, Pablo Balenzuela, Jennifer Foss, and Dante R Chialvo. Ising-like dynamics in large-scale functional brain networks. *Physical Review E*, 79(6):061922, 2009.

[34] Gustavo Deco, Mario Senden, and Viktor Jirsa. How anatomy shapes dynamics: a semi-analytical study of the brain at rest by a simple spin model. *Frontiers in computational neuroscience*, 6:68, 2012.

[35] Daniele Marinazzo, Mario Pellicoro, Guo-Rong Wu, Leonardo Angelini, Jesus M Cortes, and Sebastiano Stramaglia. Information transfer of an ising model on a brain network. *BMC neuroscience*, 14(1):P376, 2013.

[36] Sebastiano Stramaglia, Mario Pellicoro, Leonardo Angelini, Enrico Amico, Hannelore Aerts, JM Cortés, Steven Laureys, and Daniele Marinazzo. Ising model with conserved magnetization on the human connectome: Implications on the relation structure-function in wakefulness and anesthesia. *Chaos: An Interdisciplinary Journal of Nonlinear Science*, 27(4):047407, 2017.

[37] Pubuditha M Abeyasinghe, Demetrius R de Paula, Sina Khajehabdollahi, Sree R Valluri, Adrian M Owen, and Andrea Soddu. Role of dimensionality in predicting the spontaneous behavior of the brain using the classical ising model and the ising model implemented on a structural connectome. *Brain connectivity*, 8(7):444–455, 2018.

[38] Stephen G Brush. History of the lenz-ising model. *Reviews of modern physics*, 39(4):883, 1967.

[39] Tushar K Das, Pubuditha M Abeyasinghe, JS Crone, Adam Sosnowski, Stevan Laureys, Adrian M Owen, and Andrea Soddu. Highlighting the structure-function relationship of the brain with the ising model and graph theory. *BioMed research international*, 2014, 2014.

[40] Dante R Chialvo. Emergent complex neural dynamics. *Nature physics*, 6(10):744, 2010.

[41] John N Warfield and AN Christakis. Dimensionality. *Systems Research*, 4(2):127–137, 1987.

[42] Edward M Purcell and Etats-Unis Physicien. *Electricity and magnetism*, volume 2. McGraw-Hill New York, 1965.

[43] Konstantinos I Diamantaras and Sun Y Kung. *Principal component neural networks: theory and applications*, volume 5. Wiley New York, 1996.

[44] Kechen Zhang and Terrence J Sejnowski. Neuronal tuning: To sharpen or broaden? *Neural computation*, 11(1):75–84, 1999.

[45] Stefano Fusi, Earl K Miller, and Mattia Rigotti. Why neurons mix: high dimensionality for higher cognition. *Current opinion in neurobiology*, 37:66–74, 2016.

[46] Rich Pang, Benjamin J Lansdell, and Adrienne L Fairhall. Dimensionality reduction in neuroscience. *Current Biology*, 26(14):R656–R660, 2016.

[47] H Eugene Stanley. *Phase transitions and critical phenomena*. Clarendon Press, Oxford, 1971.

[48] David P Landau and Kurt Binder. *A guide to Monte Carlo simulations in statistical physics*. Cambridge university press, 2014.

Chapter 2

Role of Dimensionality in Predicting the Spontaneous Behavior of the Brain using the Classical Ising Model and the Ising Model Implemented on the Structural Connectome

2.1 Introduction

The relationship between the spontaneous activity of the brain and its structural fiber distribution is a critical topic in neuroscience. This relationship will allow us to better understand the emergence of complex but flexible dynamics (brain functions) in the brain from its underlying structural network. The structure-function relationship is commonly investigated using two main approaches. First, statistical methods directly compare resting state functional connectivity patterns with the structure. Statistical comparisons lead to important results indicating the presence of a significant correlation between the anatomical fiber distribution and the func-

tional connectivity patterns [1, 2]. The other common approach to understand the structure-function relationship of the brain is by using simple mathematical models that could capture the complex dynamics of the brain.

There are several models which have been used to discuss the spontaneous behavior of the brain, including the Neural mass model, the Kuramoto model, and the well-known 2-dimensional (2D) classical Ising model. The Neural mass model and the Kuramoto model have been successful in providing evidence for the existence of a connection between the anatomical structure and the spontaneous fluctuations of the brain as captured by fMRI [3, 4, 5, 6, 7].

The classical Ising model was developed by Ernest Ising [8] to explain the phase transition to ferromagnetic behavior at a critical temperature. It has been used to investigate brain dynamics by [9]. The classical Ising model is a relatively simple model with only one fitting parameter, the temperature of the thermal bath, in which a lattice simulating the regions of a ferromagnet is immersed. Yet, by virtue of its simplicity it has been able to capture the integration and segregation behavior of spontaneous brain function [9] (for more details of the 2D classical Ising model see Appendix A.1). Blood Oxygen Level Dependent (BOLD) signal is the signal fMRI methods are sensitive to and are a convolved property of neuronal fluctuations in the brain. It is modelled with the Ising model using binary spin states. BOLD signals greater than a threshold will be represented by up spins and less than the threshold will be represented by down spins with the lattice sites counting the number of brain regions. With this analogy, the 2D classical Ising model was first used by Fraiman to predict the distribution of functional correlations in the brain. They found that the best prediction of the distribution of correlations was obtained from the model at the critical temperature while important deviations were observed for even small changes in temperature from criticality. Successful results of these comparisons have led to further investigations of the model to explain the structure-function relationship of the brain.

In a subsequent work, the 2D classical Ising model was generalized by Marinazzo et al., [10] by implementing the model on the structural connectome, in order to match each

region of the brain with a corresponding lattice site. Criticality was confirmed for the generalized model and, information transfer was found to be maximum at the critical temperature as well. The generalized Ising model was further studied by Stramaglia et al. by comparing correlation values and transfer entropy between simulated and functional empirical data [11]. Furthermore, Deco et al. studied an Ising model implemented on the structural connectome and compared with the implementations of the model on artificially created connectomes with differnet coupling strengths [7]. They investigated the entropy of the systems as a function of the coupling strength to conclude that the simulated system exhibits rich dynamics similar to the empirical functional connectivity when the structure is integrated as a scale-free network.

In this paper we compared the classical Ising model and the Ising model implemented on the structural connectome with respect to the empirical data demonstrating that both models exhibit similar functional patterns and global properties despite the intrinsic differences. If both models are in the same universality class (same critical exponents), then their similarity would not be surprising. To investigate the cause of their similarities, the critical exponents (explained below as well as in Appendix A.2) of both models were calculated and compared [12]. If we know the critical exponents of one system in a particular universality class, we can explain any other system in the same universality class, whose microscopic causes could be totally different from the known system. The critical exponents are said to explain the behavior of the system around the critical temperature. Greek letters β , γ , α , η and are used to represent the critical exponents of magnetizations, susceptibility, specific heat, correlation function [13] and correlation length [14] respectively. These critical exponents together with the dimensionality 'd' follow the scaling relations explained in Appendix A.2.

Dimensionality, together with the other critical exponents, is fundamental to understand the behavior of the system around criticality. Physiological changes of the brain, as for example induced by sleep, could be in fact explained by the model deviating from criticality. Dimensionality of a system has been found to be highly relevant for the system performance also in neural networks [15]. In their paper, they have concluded that different dynamics can be

observed in neural networks with different connectivity patterns coming from different dimensionality.

For the classical Ising model the dimensionality of the system is given by the number of dimensions of the lattice (d = 2 for a square lattice) and there is a well-defined relationship between the number of nearest neighbors in the lattice and the dimensionality (number of nearest neighbors = 2 × dimensionality). However, for the generalized Ising model the dimensionality of the system is not evident as for the classical case and in order to be extracted a new concept of distance needed to be introduced.

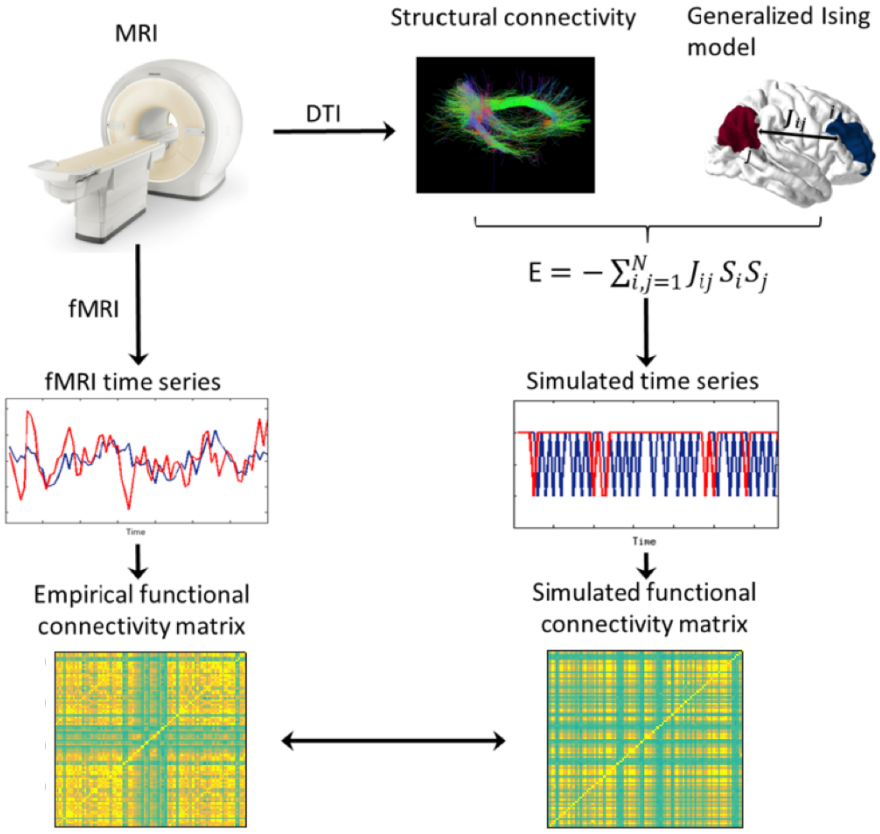

Figure 2.1: Summarized representation of the analysis carried out. We obtained the structural and functional data separately from brain imaging techniques. Then, the structural connectivity was used as the input of the generalized Ising model. Using this input, the generalized Ising model was simulated for different temperatures and each time the output was compared with the empirical functional data obtained from fMRI

The key components of the steps carried out are summarized in Figure 2.1. The orga-

nization of the paper is as follows. In the next section, we will introduce the methodology of calculating and comparing properties of the empirical functional connectivity with the ones generated from the numerical simulations of the classical Ising model and the generalized Ising model. Then we will explain the procedure we followed to calculate the critical exponents and the dimensionality of the models. Next, we will explain the main findings of the work that was carried out, which will be followed by discussion and conclusions.

2.2 Materials and methods

2.2.1 Acquisition and preprocessing of data

Subjects

A set of sixty-six healthy subjects, between 22 - 35 years old, were studied during wakefulness. Informed consent to participate in the study was obtained from every subject.

Ethic statement

The Ethics Committee of the Washington University and the University of Minnesota approved the study.

Acquisition and preprocessing of data

Structural and functional data were acquired at the Washington University - University of Minnesota Consortium of the Human Connectome Project (WU-Minn HCP). Details about the data acquisition and preprocessing can be found here [16, 17, 18, 19, 20, 21, 22, 23, 24]. Parcellation of the data was performed, using FSL, Freesurfer and MRTrix software with 84 individually labelled regions (a list of the labels is presented in Appendix A.3). Extraction of the structural connectivity matrix (J_{ij}) was performed using the MRTrix software.

2.2.2 2D Ising Model and the generalized Ising model

Computer simulations

An instance of the 2D Ising model is built starting with a random spin configuration on a square lattice of size L× L (= 9 × 9) which is in contact with a thermal bath of temperature T. For comparison purposes, a square lattice Ising model with a 9 × 9 lattice size was chosen, as it gives 81 spin sites (that is the closest number of sites to 84 we can acquire using a square lattice). For the generalized Ising model, a 1 × 84 array of random spins was used. Each spin can be in only one of two spin states (either up (+1) or down (-1)). The energy of this spin configuration at a state x, in the absence of an external magnetic field is given by;

$$E(x) = -\sum_{i,j=1}^{N} J_{ij} S_i S_j \tag{2.1}$$

where J_{ij} is the coupling between ith and jth region, si and sj represent the spins of the ith and jth region respectively and N = L × L. A matrix representing the coupling J_{ij} for the 2D Ising model has been created to encode nearest neighbor coupling with a coupling strength of one [9]. In contrast, another matrix representation of coupling J_{ij} for the generalized Ising model has been created using the connectivity matrix which was built from the Diffusion Tensor Image (DTI) acquisition. This matrix contains the number of fiber tracts between each pair of regions in the connectome which is being used to define the coupling strength. For the simulations of the model we normalized the average structural connectivity matrix (average over 69 subjects) such that the matrix elements will be between 0 and 1. A Metropolis Monte Carlo algorithm [25, 26] was used to simulate the system at each temperature. Metropolis Monte Carlo algorithm allows to generate an equilibrium spin configuration starting from a random spin configuration for each temperature (more details can be found in Appendix A.1). From the final output of the simulations, the correlation between the time evolutions of spins for each temperature was calculated using Equation 2.2,

$$corr = \frac{< s_i(t) \times s_j(t) > - < s_i(t) >< s_j(t) >}{\sigma_{s_i(t)} \times \sigma_{s_j(t)}} \tag{2.2}$$

where s_i and s_j stands for the spins of i^{th} and j^{th} regions, $\sigma^2_{s_i(t)} = < s_i^2(t) > - < s_i(i) >^2$ and $< . >$ is for the average over time.

Using this procedure, the correlations were generated by each model as a function of temperature. Afterwards, this procedure was repeated for both models to generate ten sets of data for each, always starting with a random spin configuration. Generating ten independent simulations further ensures that the Metropolis algorithm explores a variety of initial conditions and therefore increases the (statistical) accuracy of the results. MATLAB (https://www.mathworks.com/) was used for the computer simulations and analysis whereas RStudio (https://www.rstudio.com/) was used to generate graphs.

2.2.3 Analysis

Preliminary analysis

Analysis was performed over the average of ten data sets for both models. The thermodynamic properties were plotted as functions of temperature for the two models to obtain the critical temperature (Figure 2.2). The critical temperature can be obtained by locating the temperature which maximizes the magnetic susceptibility of the system (Equation 2.3) where χ is the magnetic susceptibility, T is the temperature and M is the magnetization [12]).

$$\chi = \frac{1}{T}[< M^2 > - < M >^2] \tag{2.3}$$

The empirical functional correlation matrix which is built by averaging the correlation matrices across the 66 healthy subjects was compared with the simulated correlation matrices (Figure 2.3) for further analysis. Additionally, the distribution of the correlation for the simulated data as well as for the empirical data was plotted in Figure 2.4.

Next, the distance between the simulated correlation distributions and the empirical correla-

tion distribution was calculated as a function of temperature and presented in Appendix A.4.1. The distance between the empirical and simulated correlation distributions is quantified using the Kolmogrove-Smirnov test (KS test) statistic [27]. To calculate the KS test statistic, empirical and the simulated correlations were plotted as cumulative plots in the same graph. Next, the maximum distance between these two plots was calculated. Temperatures which minimize this maximum distance (T_{min}) has been obtained for individual simulations. Distribution of T_{min} and Tc for the generalized Ising model is presented in Figure 2.5.

In order to calculate the global degree as a function of threshold, correlations were separated into positive and negative correlations. Then the global degree was calculated for the negative and positive thresholds separately for the 2D classical Ising model and the generalized Ising model and plotted in Figure 2.6 together with the global degree of the empirical data [28]. Taking the individual node degree into consideration, connectivity graphs are plotted for the generalized Ising model at four different temperatures and been compared with the graph of the empirical data (Figure 2.7).

Analyzing the behavior at the criticality using the critical exponents

The critical exponents and the dimensionality were calculated for the two models by following the procedure below. First, the critical exponents related to magnetization, susceptibility and specific heat were calculated by fitting Equation A.7 - A.11 (in Appendix A.2) to the respective plots in Figure 2.2. To find η and ν, following procedure was used:

Correlation function: First, a set of distances for both models were defined using the respective connectivity matrices. For the classical Ising model, the distances were the integers from 1 to 8, since the initial configuration was a 9×9 2D lattice. However, for the generalized Ising model the distance between two regions is defined as the reciprocal of the normalized number of fibers between the two regions ($d_{ij} = \frac{1}{J_{ij}}$). We binned the continuous distances to create a set of discrete groups. Then the correlation values between pairs at the same distance were averaged to get the average correlation as a function of distance. This calculation was

performed for each temperature (Figure 2.8). By fitting Equation A.14 (Appendix A.2) to the plot of correlation function versus the distance at the critical temperature, η was calculated. By subsequently using Equation A.13 to fit the correlation function at the critical temperature, a numerical value for the power of the denominator (= d - 2+ η) was then obtained. Using this fitted value and the calculated η at Tc the dimensionality of the classical Ising model as well as the generalized Ising model was finally extracted. Correlation length: Correlation length at each temperature was calculated by fitting Equation A.12 (Appendix A.2) to the correlation function versus the distance at each temperature. The correlation length was plotted as a function of temperature and fitted with Equation A.15 and A.16 (Appendix A.2) to find ν (Figure 2.8).

2.2.4 Results

Preliminary analysis

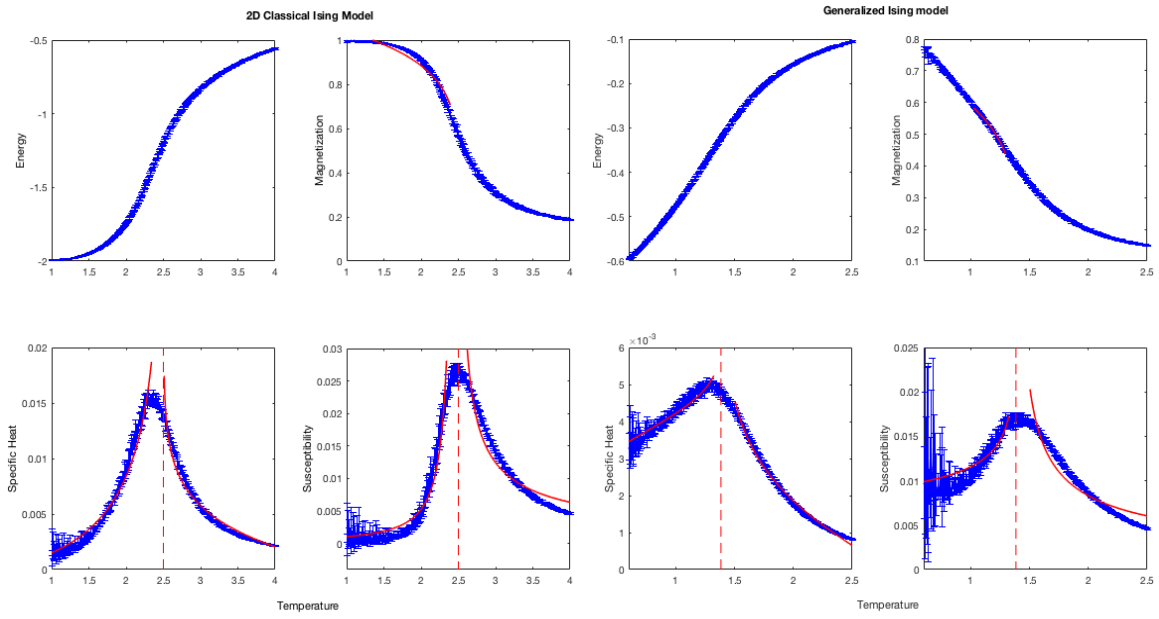

Figure 2.2: Thermodynamic properties of the 2D classical Ising model with 9×9 lattice size and the generalized Ising model as a function of temperature. Red dashed line indicates the critical temperature and the red solid lines represent the plots after fitting the given equations to calculate the critical exponents

The mean values of critical, sub-critical and super critical temperatures over the ten independent trials were obtained using the susceptibility plots in Figure 2.2 and are reported in Table 2.1 together with their standard deviations. The critical temperature value of the 2D Ising model agree with the critical temperature described in literature for the lattice size L = 9. In the generalized Ising model, the phase transition occurs at a lower temperature than that of the classical Ising model.

Table 2.1: Sub-critical, critical and super-critical temperatures of the generalized Ising model and the 2D classical Ising model

Model	$T < T_c$	$T = T_{min}$	$T = T_c$	$T > T_c$
Generalized Ising model	0.78 ± 0.02	1.21 ± 0.04	1.39 ± 0.02	1.98 ± 0.02
Classical Ising model	1.55 ± 0.10	2.53 ± 0.20	2.55 ± 0.10	3.55 ± 0.10

Correlations for four different temperatures are presented in Figure 2.3. At T_c the spatial pattern of the correlations in the generalized Ising model hold a similar spatial pattern to that of the empirical data. Distributions of the correlations for the selected four temperatures are plotted in Figure 2.4 along with the empirical data. For the classical Ising model correlation distributions showed difference between the empirical distribution and the simulated one at criticality, even if the critical temperature T_c or the slightly different value T_{min} gave a much better prediction with respect to sub or supercritical behavior. For the generalized Ising model the distribution of correlations at T_c and T_{min} and the distribution of correlations for the empirical data were not significantly different (p = 0.98) while the distributions at sub and supercritical temperatures were quite distant from the empirical distribution.

According to Figure 2.5, the variation of T_c (and T_{min}) is resulted due to the randomness of the initial spin configuration in the simulations. To illustrate the inter-subject variance of T_c (and T_{min}), distributions of T_c (and T_{min}) are presented in Appendix A.4.2. A two-sample t-test was performed to compare the T_{min} values with the T_c values in individual simulations. Results of the t-test together with Figure 2.5 concluded that T_{min} and T_c are significantly different for the generalized Ising model (p ¡0.001) but not significantly different for the 2D Ising model

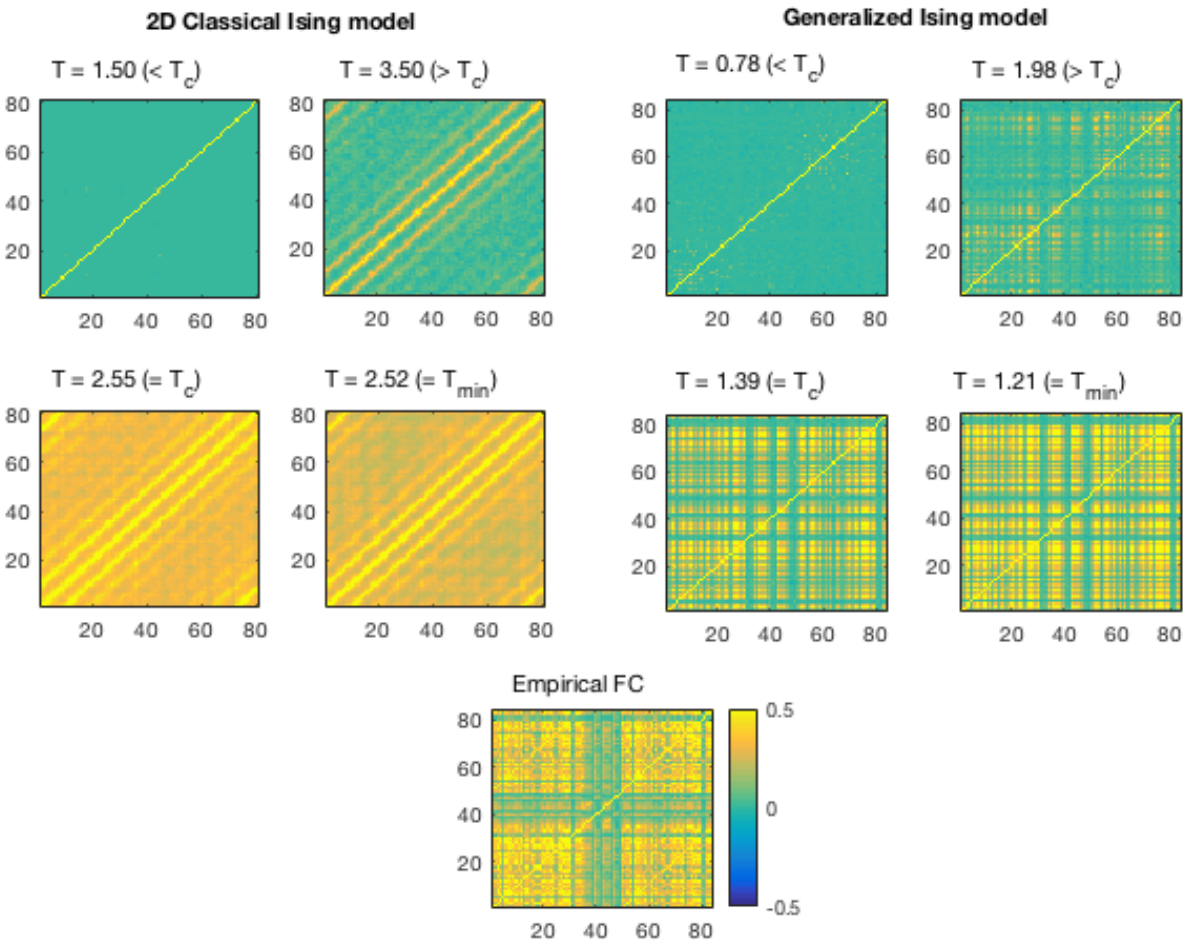

Figure 2.3: Correlation at four different temperatures for the classical Ising model and the generalized Ising model with the correlation of the empirical data

(with p = 0.4).

Graph theoretical analysis

In Figure 2.6, the global degree of the graphs was plotted as a function of negative and positive thresholds for both models. As observed in Figure 2.4 there are no negative correlations at T_c or at T_{min} for the classical Ising model. Therefore, in Figure 2.6 the degree cannot be plotted for the negative thresholds at T_c and T_{min} for the classical Ising model. Figure 2.7 represents the functional connectivity graphs for the data obtained from the generalized Ising

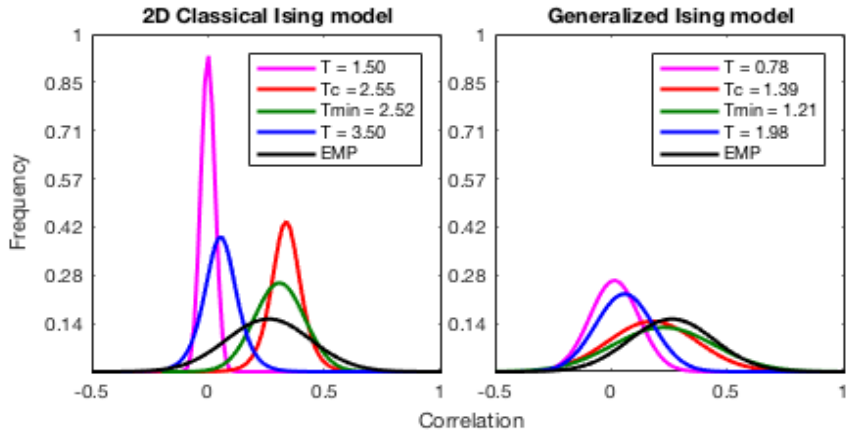

Figure 2.4: Distribution of the correlation at four different temperatures for the classical Ising model and the generalized Ising model with the distribution of correlation of the empirical data

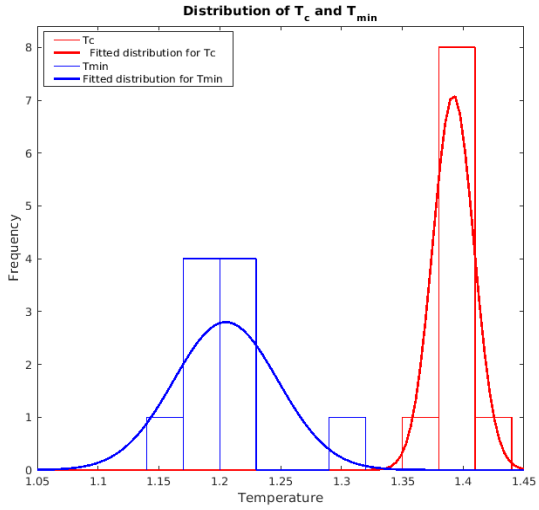

Figure 2.5: Histogram of T_c and T_{min} together with the fitted distributions for the generalized Ising model in 10 independent simulations

model simulations at sub-critical, critical, super-critical temperatures and T_{min} along with the connectivity graph of the empirical data. In these graphs, each point represents a brain region. It is evident that the connectivity in the network grows as the temperature goes from $T < T_c$ to T_c and again reduced from T_c to $T > T_c$, and shows similar patterns for T_c and T_{min}.

Analyzing the behavior at the criticality using the critical exponents

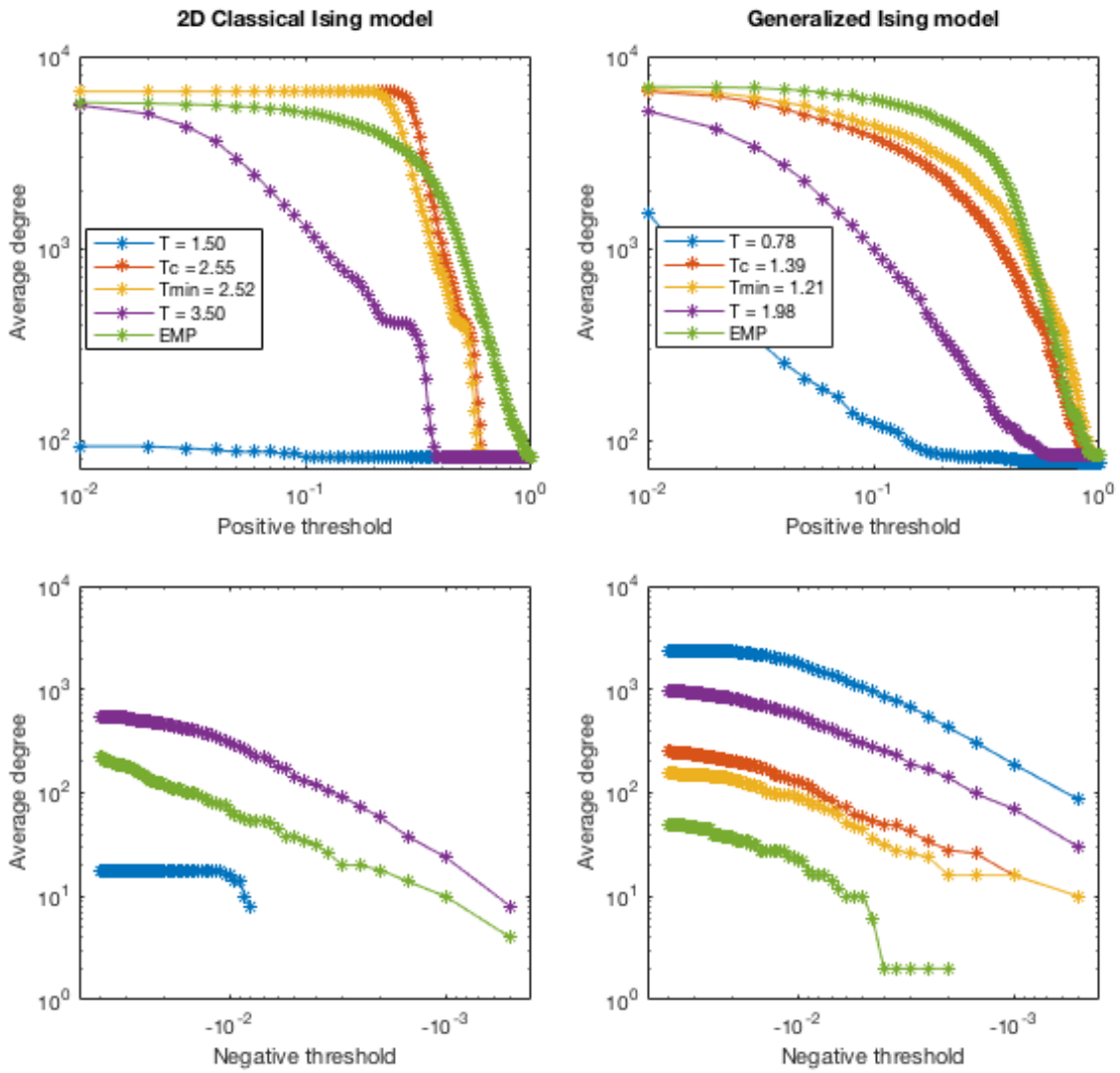

Figure 2.6: Average degree as a function of positive and negative thresholds for the classical Ising model and the generalized Ising model together with the average degree of the empirical correlation network

Figure 2.8 represents the correlation function and the correlation length plotted for the two models. These two plots were used to find the critical exponent and the dimensionality "d" of the models. The calculation of dimensionality for the classical Ising model confirmed the expected value of 2 (since we chose the square lattice Ising model in two dimensions) giving the value of 1.93 ± 0.59. The dimensionality of the generalized Ising model was calculated for the first time giving a value of 1.92 ±0.12 and proven equal to the classical Ising model value

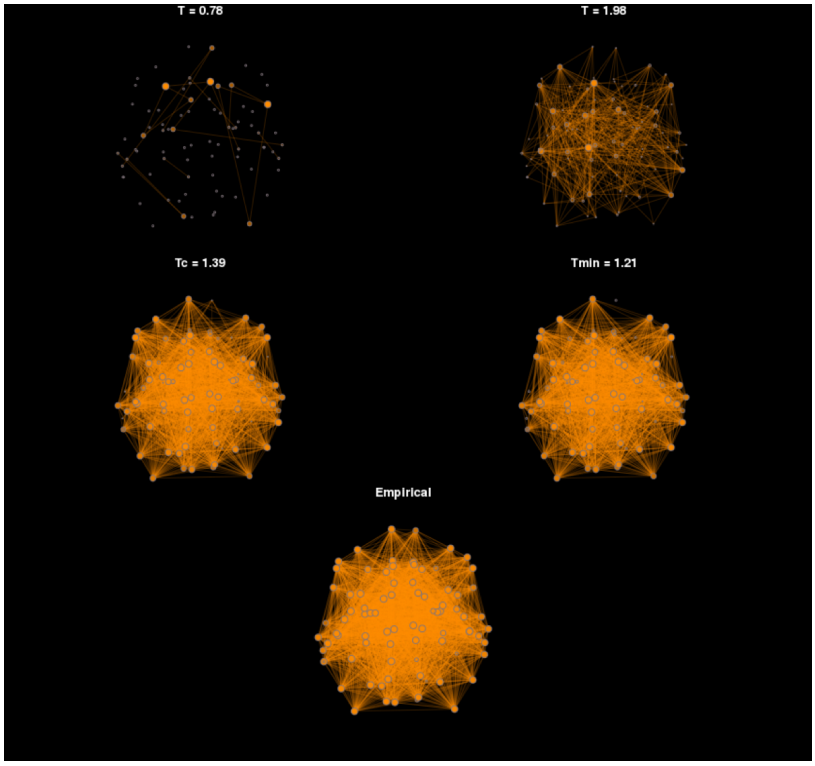

Figure 2.7: Connectivity graphs for the generalized Ising model for four temperatures, and the connectivity graph of the empirical network. The size of the nodes represents the degree such that larger the size, higher the degree

inside the fitting error. All the other critical exponents are reported in Table 2.2 together with the dimensionality for both models.

Critical exponent	**2D Classical Ising model**	**Generalized Ising model**
α (Specific heat)	1.49 ± 0.02	0.81 ± 0.01
β (Magnetization)	0.14 ± 0.01	0.21± 0.01
γ (Susceptibility)	0.61 ± 0.01	0.53± 0.01
η (Correlation function)	0.34 ± 0.01	0.46± 0.01
ν (Correlation length)	0.30 ± 0.01	0.63± 0.02
d (Dimensionality)	1.93 ± 0.59	1.92± 0.12

Table 2.2: Critical exponents and the dimensionality of the 2D classical Ising model and the generalized Ising model

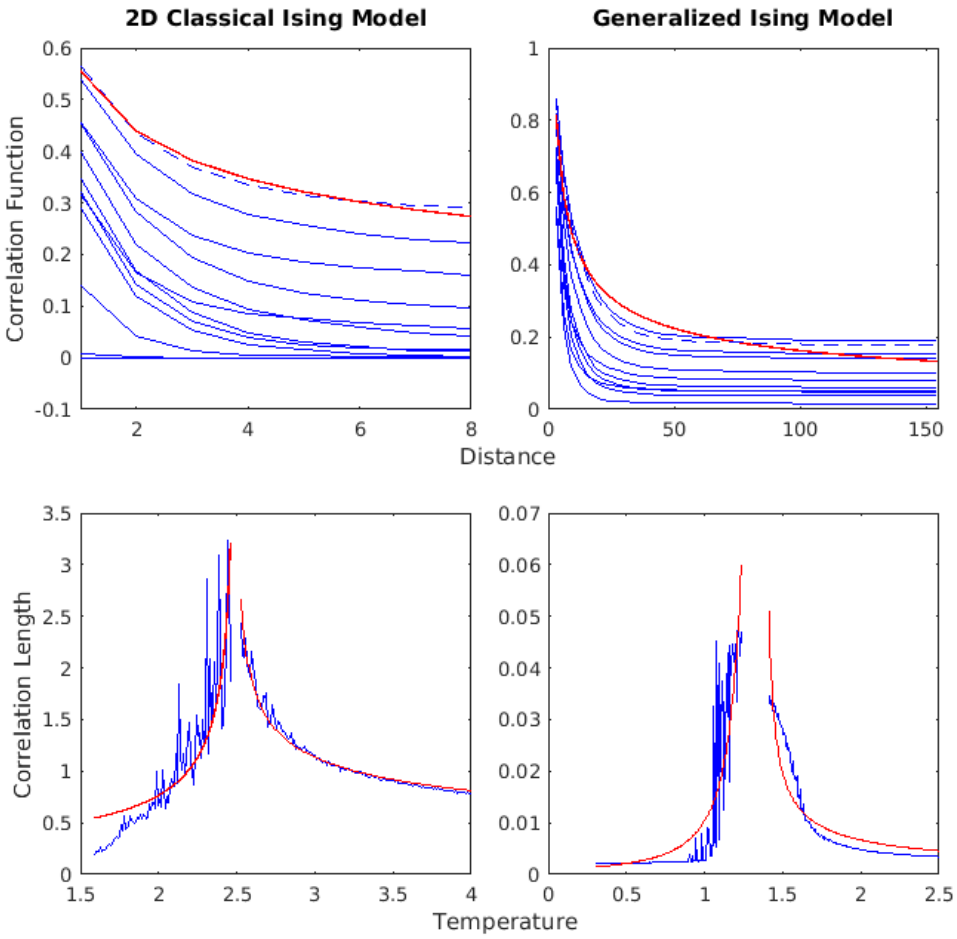

Figure 2.8: Correlation function versus distance and correlation length versus temperature for the 2D classical Ising model and the generalized Ising model. Red solid line represents plots after fitting the given equations (Appendix A.2). In the top panel, the dashed line represents the correlation function at the critical temperature

2.2.5 Discussion

The square lattice Ising model has been used in neuroscience to study brain functionality. Fraiman et al. showed that the distribution of correlations at T_c in the 2D classical Ising model has noticeable similarities to the distribution of correlations of the empirical data, even in the absence of information from the structural architecture of the brain [9]. Their conclusion together with several other studies supported the assumption of the presence of critical behavior in the brain network [10, 7, 11]. In this paper, as the first step we compared simulations of a 2D Ising model with those of the generalized Ising model by looking at the distributions of correlation values. The fact that for both models the mean of the correlation distribution values at the critical temperature is larger than the mean of the correlation distribution at sub-critical or super-critical temperatures is a well-known prediction of the Ising model in the classical version and was confirmed by our results for the generalized model. Correlation between the i^{th} and the j^{th} regions can be calculated using Equation 2.4 (where r_{ij} is the distance between region i and j, ζ is the correlation length, d is the dimensionality and η is the critical exponent of the correlation function), and is clearly shown from Figure 2.8.

$$corr_{ij} = \frac{exp(\frac{-r_{ij}}{\zeta})}{r^{(d-2+\eta)}} \tag{2.4}$$

At the critical temperature, because the correlation length (ζ) goes to infinity (in the infinite lattice size limit), the correlation will have a power low decay with the distance. On the contrary, at any other temperature, ζ will be finite and the correlation will have a combined exponential and power low decay. Therefore, outside of criticality correlation will drop faster with distance resulting in a lower average correlation value. For finite lattice size the difference between the mean of the distribution at criticality and outside criticality will be reduced with respect to the infinite lattice size limit.

In the generalized Ising model, the introduction of the coupling from the structural connectivity of the brain provided a one to one relationship between the brain regions and the lattice

sites. Each lattice site was connected with every other site with a given weight which was obtained from DTI as opposed to the 2D classical Ising model. One objective was to investigate behavior at the critical temperature with respect to these changes in the model. When the structure is introduced, we observed a shift in the critical temperature from 2.5 (2D Ising model) to 1.4 (generalized Ising model). An illustration of this change as a function of sparsity of the structural connectivity matrix is presented in Appendix A.4.3. We can conclude that the critical temperature depends not only on the size of the matrix but also on the sparsity of the connectivity matrix.

The temperature which minimizes the distance between the distributions of correlation (T_{min}) was significantly different from Tc for the generalized Ising model but not for the 2D classical Ising model. Global degree plotted as a function of the temperature (Appendix A.4.4) was maximized at a temperature which is not different from T_{min}. This fact suggests the usage of graph properties to extract T_{min} of the Ising model, either in the classical or generalized version as done by looking for the maximum of susceptibility. Figure 2.9 represents the possibility of finding a relationship between the graph properties and the thermodynamic properties of the Ising model. As the theory implies, the specific heat and the susceptibility measure the variation of energy and magnetization with temperature respectively. This was captured by calculating the cumulative integral of the specific heat and susceptibility of the generalized Ising model. Following the same procedure, the cumulative integral of the global degree was calculated, which resulted in the plot on the right-hand corner in the top panel of Figure 2.9. The new plotted quantity follows a similar behavior as the energy with temperature and could be linked to a fundamental property of graph theory.

Similar properties around criticality for both models justified the use of the same fitting functions, even if we needed to introduce a concept of distance for the generalized version in order to extract the correlation length. In fact, as shown in Figure 2.8 the behavior of the correlation versus distance for the generalized Ising model is well fitted by the same function as the classical model.

Having the same dimensionality can explain the observed similarities in global behavior of the two Ising models around the critical temperature such as the correlation values and global degree. Studying the behavior around criticality for complex systems like the Ising model which shows a phase transition, could be extremely important and performed with a similar strategy as the one followed in this paper by introducing an artificial concept of distance.

As the critical exponents (in Table 2.2) are different for the two models, it cannot be concluded that these models belong to the same universality class. The fact that the global properties of the models still followed a similar pattern is due to the fact that our calculated properties all depend on the correlation values which are controlled by the dimensionality d (equal in the two models) and the critical exponent η (0.34 for classical and 0.46 for generalized) (Appendix A.2, Equation A.12).

Our findings for the generalized Ising model could be of relevance to study for example the brain function of patients who suffer severe brain injury with disorders of consciousness in which usually both structural and functional connectivity are highly affected. Furthermore, for future studies, it will be highly relevant to see how the properties of the generalized Ising model change with respect to the size of the lattice. This would mean using different parcellation schemes, different size of the system, which is contrary to the classical Ising model will also result in the change of the structural connectivity matrix (J_{ij}) that will depend on the parcellation scheme used.

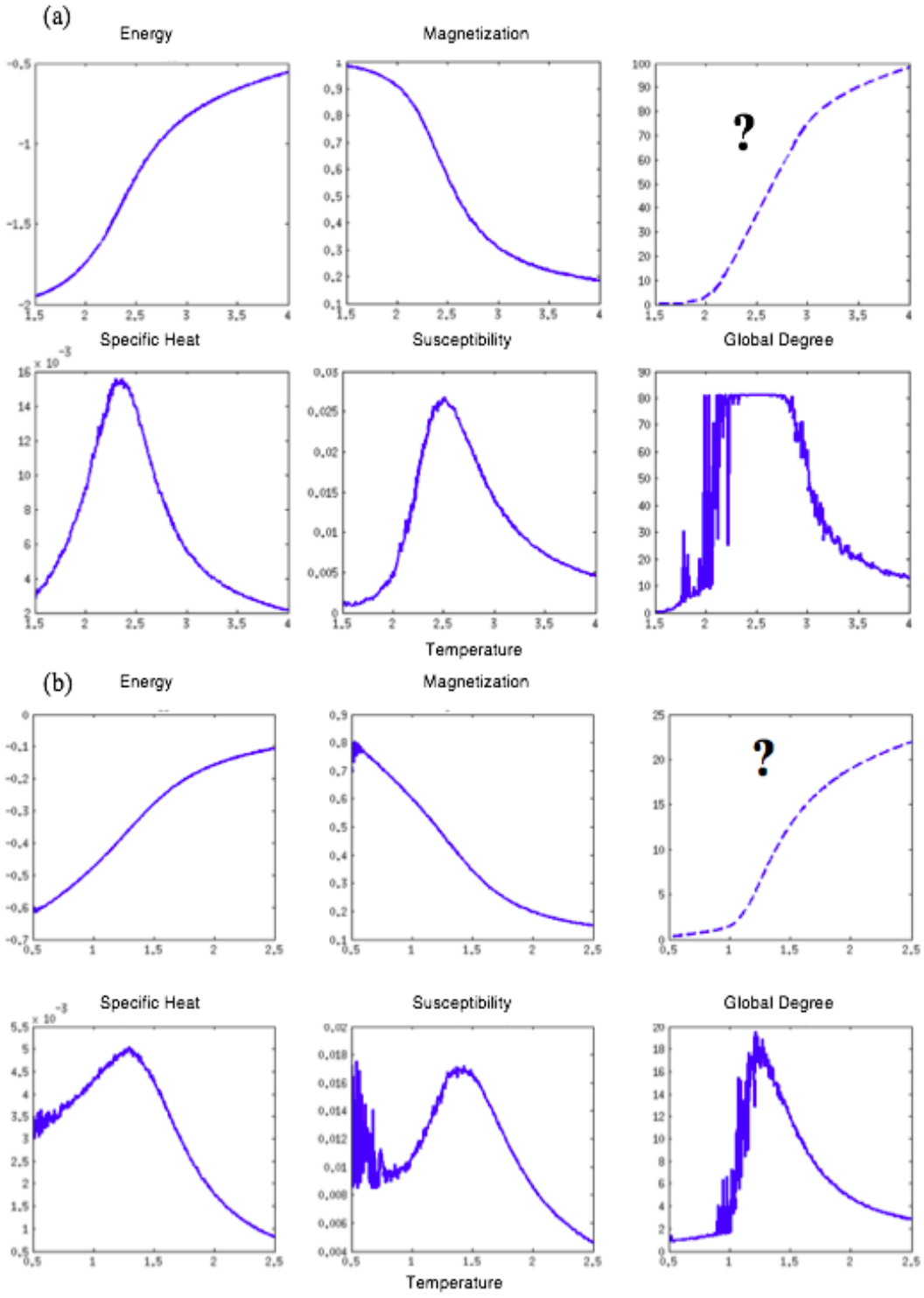

Figure 2.9: Energy, specific heat, magnetization, susceptibility, degree, and the cumulative degree of (a) the generalized Ising model and (b) the 2D classical Ising model as a function of temperature

2.2.6 Conclusion

Extending the 2D classical Ising model towards the generalized Ising model further permits to fit the empirical functional connectivity patterns. The introduction of structural data from the brain as an input into the Ising model gives the best fit to functional data at T_{min} which is significantly different from T_c in the direction of the sub-critical regime but not far from criticality. Since the critical exponents of the models are different it cannot be concluded that these two models belong to the same universality class. However, similarities observed in the global properties between the two models can be explained by the fact that they have the same dimensionality. Studying the behavior of the system around criticality could be used to better understand changes in spontaneous brain activity from the awake condition as observed in physiological states like sleep or as in pharmacologically induced conditions like under anaesthetics.

Acknowledgement

We would like to acknowledge the Human Connectome Project (HCP) for providing the data. In particular, the data were provided by the HCP, WU-Minn Consortium (Principal Investigators: David Van Essen and Kamil Ugurbil; 1U54MH091657) funded by the 16 NIH Institutes and Centres that support the NIH Blueprint for Neuroscience Research; and by the McDonnell Center for Systems Neuroscience at Washington University. Furthermore, we would like to extend the acknowledgement to Marco Aiello and Carlo Cavaliere from NAPLAB, Naples (Italy) for performing the parcellation of the preprocessed HCP data and for the extraction of the structural connectivity matrix from the DTI data.

Bibliography

[1] Pablo Barttfeld, Lynn Uhrig, Jacobo D Sitt, Mariano Sigman, Béchir Jarraya, and Stanislas Dehaene. Signature of consciousness in the dynamics of resting-state brain activity. *Proceedings of the National Academy of Sciences*, 112(3):887–892, 2015.

[2] Martijn P Van Den Heuvel and Hilleke E H Pol. Exploring the brain network: a review on resting-state fmri functional connectivity. *European neuropsychopharmacology*, 20(8):519–534, 2010.

[3] Olivier David, Diego Cosmelli, and Karl J Friston. Evaluation of different measures of functional connectivity using a neural mass model. *Neuroimage*, 21(2):659–673, 2004.

[4] CJ Honey, Olaf Sporns, Leila Cammoun, Xavier Gigandet, Jean-Philippe Thiran, Reto Meuli, and Patric Hagmann. Predicting human resting-state functional connectivity from structural connectivity. *Proceedings of the National Academy of Sciences*, 106(6):2035–2040, 2009.

[5] Juan A Acebrón, Luis L Bonilla, Conrad J P Vicente, Félix Ritort, and Renato Spigler. The kuramoto model: A simple paradigm for synchronization phenomena. *Reviews of modern physics*, 77(1):137, 2005.

[6] Michael Breakspear, Stewart Heitmann, and Andreas Daffertshofer. Generative models of cortical oscillations: neurobiological implications of the kuramoto model. *Frontiers in human neuroscience*, 4:190, 2010.

[7] Gustavo Deco, Mario Senden, and Viktor Jirsa. How anatomy shapes dynamics: a semi-analytical study of the brain at rest by a simple spin model. *Frontiers in computational neuroscience*, 6:68, 2012.

[8] Stephen G Brush. History of the lenz-ising model. *Reviews of modern physics*, 39(4):883, 1967.

[9] Daniel Fraiman, Pablo Balenzuela, Jennifer Foss, and Dante R Chialvo. Ising-like dynamics in large-scale functional brain networks. *Physical Review E*, 79(6):061922, 2009.

[10] Daniele Marinazzo, Mario Pellicoro, Guo-Rong Wu, Leonardo Angelini, Jesus M Cortes, and Sebastiano Stramaglia. Information transfer of an ising model on a brain network. *BMC neuroscience*, 14(1):P376, 2013.

[11] Sebastiano Stramaglia, Mario Pellicoro, Leonardo Angelini, Enrico Amico, Hannelore Aerts, JM Cortés, Steven Laureys, and Daniele Marinazzo. Ising model with conserved magnetization on the human connectome: Implications on the relation structure-function in wakefulness and anesthesia. *Chaos: An Interdisciplinary Journal of Nonlinear Science*, 27(4):047407, 2017.

[12] David P Landau and Kurt Binder. *A guide to Monte Carlo simulations in statistical physics*. Cambridge university press, 2014.

[13] Paul Expert, Renaud Lambiotte, Dante R Chialvo, Kim Christensen, Henrik J Jensen, David J Sharp, and Federico Turkheimer. Self-similar correlation function in brain resting-state functional magnetic resonance imaging. *Journal of The Royal Society Interface*, 8(57):472–479, 2010.

[14] Daniel Fraiman and Dante R Chialvo. What kind of noise is brain noise: anomalous scaling behavior of the resting brain activity fluctuations. *Frontiers in physiology*, 3:307, 2012.

[15] Francesco PU Severino, Jelena Ban, Qin Song, Mingliang Tang, Ginestra Bianconi, Guosheng Cheng, and Vincent Torre. The role of dimensionality in neuronal network dynamics. *Scientific reports*, 6:29640, 2016.

[16] Matthew F Glasser, Stamatios N Sotiropoulos, J Anthony Wilson, Timothy S Coalson, Bruce Fischl, Jesper L Andersson, Junqian Xu, Saad Jbabdi, Matthew Webster,

Jonathan R Polimeni, et al. The minimal preprocessing pipelines for the human connectome project. *Neuroimage*, 80:105–124, 2013.

[17] Mark Jenkinson, Christian F Beckmann, Timothy EJ Behrens, Mark W Woolrich, and Stephen M Smith. Fsl. *Neuroimage*, 62(2):782–790, 2012.

[18] Bruce Fischl. Freesurfer. *Neuroimage*, 62(2):774–781, 2012.

[19] Mark Jenkinson, Peter Bannister, Michael Brady, and Stephen Smith. Improved optimization for the robust and accurate linear registration and motion correction of brain images. *Neuroimage*, 17(2):825–841, 2002.

[20] Matthew F Glasser and David C Van Essen. Mapping human cortical areas in vivo based on myelin content as revealed by t1-and t2-weighted mri. *Journal of Neuroscience*, 31(32):11597–11616, 2011.

[21] Jesper LR Andersson, Stefan Skare, and John Ashburner. How to correct susceptibility distortions in spin-echo echo-planar images: application to diffusion tensor imaging. *Neuroimage*, 20(2):870–888, 2003.

[22] Jesper LR Andersson and Stamatios N Sotiropoulos. Non-parametric representation and prediction of single-and multi-shell diffusion-weighted mri data using gaussian processes. *Neuroimage*, 122:166–176, 2015.

[23] Jesper LR Andersson and Stamatios N Sotiropoulos. An integrated approach to correction for off-resonance effects and subject movement in diffusion mr imaging. *Neuroimage*, 125:1063–1078, 2016.

[24] David C Van Essen, Matthew F Glasser, Donna L Dierker, John Harwell, and Timothy Coalson. Parcellations and hemispheric asymmetries of human cerebral cortex analyzed on surface-based atlases. *Cerebral cortex*, 22(10):2241–2262, 2011.

[25] Nicholas Metropolis, Arianna W Rosenbluth, Marshall N Rosenbluth, Augusta H Teller, and Edward Teller. Equation of state calculations by fast computing machines. *The journal of chemical physics*, 21(6):1087–1092, 1953.

[26] Harvey Gould, Jan Tobochnik, Dawn C Meredith, Steven E Koonin, Susan R McKay, and Wolfgang Christian. An introduction to computer simulation methods: Applications to physical systems. *Computers in Physics*, 10(4):349–349, 1996.

[27] Frank J Massey Jr. The kolmogorov-smirnov test for goodness of fit. *Journal of the American statistical Association*, 46(253):68–78, 1951.

[28] Mikail Rubinov and Olaf Sporns. Complex network measures of brain connectivity: uses and interpretations. *Neuroimage*, 52(3):1059–1069, 2010.

Chapter 3

Deterministic or Probabilistic Tractography?

A comparison of Diffusion Tractography Methods in Simulating the Generalized Ising Model to Predict the Spontaneous Fluctuations of the Brain

3.1 Introduction

3.1.1 Diffusion tractography

Diffusion Tensor Imaging (DTI) is a Magnetic Resonance Imaging (MRI) technique that was developed in the early 1990s to characterize white matter tracts of the brain [1, 2]. White matter is composed of the axons of neurons, which are responsible for passing electrical signals between neurons [3]. Identifying the characteristics of white matter plays a pivotal role in research as well as is clinical diagnosis [4, 5]. DTI focuses on the random movements (diffusion) of water molecules in the brain. As water molecules are more free to move along fibers than across them, monitoring the movement of water molecules allows us to image their fiber paths. DTI has improved over the years, to the point where it is now the most com-

monly used imaging technique to estimate the orientation and location of white matter in the brain [6, 1, 7, 8]. While calculating the diffusion of water molecules using the diffusion tensor, another measure—namely, "Fractional Anisotropy (FA)" [9]—can be derived from DTI to calculate the directionality of the diffusion process. The FA is a scalar value between zero and one which provides a quantitative measure of anisotropy. FA has been used in various neuroscience research areas, such as the diagnosis of tumors, and the diagnosis of stroke patients states from FA's time-dependence [10, 11, 12, 13] to better diagnose the state of the patients. In [14] FA was used as a threshold to obtain the most likely fiber tracts from tractography. In this manuscript, we explore the use of FA not only as a weighting parameter of the connectome, but also, as a direct representation of the connectome in predicting the spontaneous fluctuations of the brain.

The process of estimating the orientation and location of white matter using brain images obtained by DTI is called 'tractography'. Tractography techniques play a pivotal role in generating a structural connectome. Probabilistic and deterministic tractography are two basic white matter tractography methods which allow non-invasive extraction of anatomical connectivity patterns [15, 16]. In deterministic tractography, one direction per voxel is assigned depending on the diffusivity constant; whereas in probabilistic tractography, a probability distribution of the directions is assigned. Once all the voxels have been assigned a direction from the diffusion of water molecules using the tractography method of choice, directions of all the voxels integrated together recovers the fiber tracts. This process results in a map of connectivity (connectome [17, 18]) which provides the number of fibers between each pair of voxels. There are a number of studies that compare the probabilistic tractography and the deterministic tractography such as [19, 15, 20], discussing both advantages and disadvantages of the two methods. However, there is an active debate over whether the deterministic tractography generates the streamlines of the human brain accurately enough, due to its higher number of false negatives [21, 22]. On the other hand, probabilistic tractography reduces some of the uncertainties associated with deterministic tractography by not directly finding the direction of a fiber, but by

giving the probability of its orientation for each voxel. In [20] it is shown that the probabilistic tractography is more useful in identifying cross-fiber connections, while the deterministic tractography can better identify long-range anatomical connections. Probabilistic tractography is prone to have a higher number of false positives, as it assigns a probability distribution of the direction rather than a single direction for the fiber. However, the selection of tractography method is highly subjective to the study in hand and remains a debated topic [22]. Choosing a particular tractography method indicates nothing but changing the structural connectome that will be used in the simulations. Therefore, our objective is to study the stability and the predictability of the generalized Ising model by selecting different types of structural connectivity matrices similar to what is presented in [23] for other models. We considered these differences that are under discussion and applied six different tractography techniques to generate structural connectomes. These structural connectomes were then used as input to simulate the generalized Ising model and predict the spontaneous activity of the brain.

3.1.2 Computational modelling

Emergence of the brain function from anatomical connections is still a very open area of research in neuroscience. Investigating the structure-function relationship is highly important to understanding large-scale neural mechanisms and how brain dynamics can be possibly affected by brain disorders [24]. In literature, different studies focus on the direct structure-function relationship of the brain [25, 26, 27]. Most of these studies have demonstrated a significant relation between the anatomical and the functional connectivity patterns by performing statistical analysis. These studies consider the full brain as well as its network representation. Of course, different statistical findings depend upon the method by which the functional connectivity patters are extracted. Pearson product-moment coefficient and partial correlation—or any other statistical approach like Recursive Feature Elimination (RFE) [28]—will extract different correlation patterns and will consequently capture different features of the anatomical distribution. Introducing computational models (in parallel to direct comparisons) can provide added

value to better understand how functional patterns are supported by anatomy.

Among the recent computer modelling approaches proposed in the literature [29, 30, 31], one of the well-known models that has been shown to predict functional connectivity using the anatomical structure is the generalized Ising model [29, 32, 33, 34]. The generalized Ising model is an Ising model simulated on a structural connectome. Prior to the generalization of the model, a 2-dimensional classical Ising model was first introduced by Ernest Ising to illustrate the behavior of ferromagnets [24], and was later used to predict the global behavor of the brain's functional connectome [35]. The Ising model was then generalized to predict the spontaneous activity of the human brain [29, 32, 33, 34]. The classical Ising model was generalized using the structural connectome of the brain in light of discovering a relationship between the anatomical structure and its functional counterpart.

Deco et al. [29] were the first to implement an Ising model on a structural connectome obtained using deterministic tractography. By studying the entropy of a spin system using an empirical structural connectome as well as artificially created structural connectomes, they concluded that the simulated system can predict the empirical functional connectivity in the form of pairwise correlations when the structural connectome is scale-free. Studies of the generalized Ising model were further extended by Marinazzo et al. [32], where they simulated the Ising model using a structural connectome generated by deterministic tractography following the exact procedure as discussed in [36]. Nevertheless, by calculating the information transfer of the model and investigating the emergence of correlation-based network structures through the model, they showed that the critical state of the generalized Ising model is characterized by possessing maximum information flow. Later in [33], the Ising model was implemented again on a structural connectome that was generated using deterministic tractography, in order to compare the spin correlations between the simulated and the empirical functional data through transfer entropy of healthy subjects as well as at anaesthetic conditions. Their findings confirmed that the brain dynamics under anaesthesia cannot be explained by the criticality of the model, but by a deviation from criticality. Even if the structural connectivity is unchanged,

the correlation between population of neurons is profoundly altered under anesthesia. The loss of these correlations escapes the intrinsic hypothesis of the Ising model. In fact, criticality is an intrinsic property of the Ising model and to the structural connectivity and in this case departs from the functional connectivity at the critical temperature. Most recently, in our previous work [34] we compared a 2D classical Ising model with the generalized Ising model. The generalized Ising model was simulated on a structural connectome generated by probabilistic tractography and was studied further using graph-theoretical properties to find structure-function relationship. In conclusion, we demonstrated that studying the behavior of the generalized Ising model around criticality can help understand more characteristics of the system, and in doing so we introduced a novel methodology to calculate the "dimensionality" of the brain (as presented in Appendix C.1.

While all these studies successfully explained the predictability of the empirical functional correlations using the generalized Ising model with different matrices in different perspectives, there is a lack of knowledge of the effects of tractography on the predictions. Because the structural connectome in the only input of the generalized Ising model, the source of coupling strengths, and the topological reference, it is essential to investigate its properties. Therefore, in this manuscript we investigate the effects of probabilistic and deterministic tractography methods with/without FA on generating the structural connectomes. The comparisons are performed via the simulations of the generalized Ising model.

The main focus of our work is to identify the tractography method which provides the best structural connectome for use in the generalized Ising model simulations, which can, in turn, obtain the strongest prediction of the spontaneous fluctuations of the brain. We also seek to demonstrate the improvements realized by the generalized Ising model in predicting functional connectivity, as measured by Pearson product-moment coefficient.

3.2 Methodology

Methodology is summarized in Figure 3.1 and explained further below.

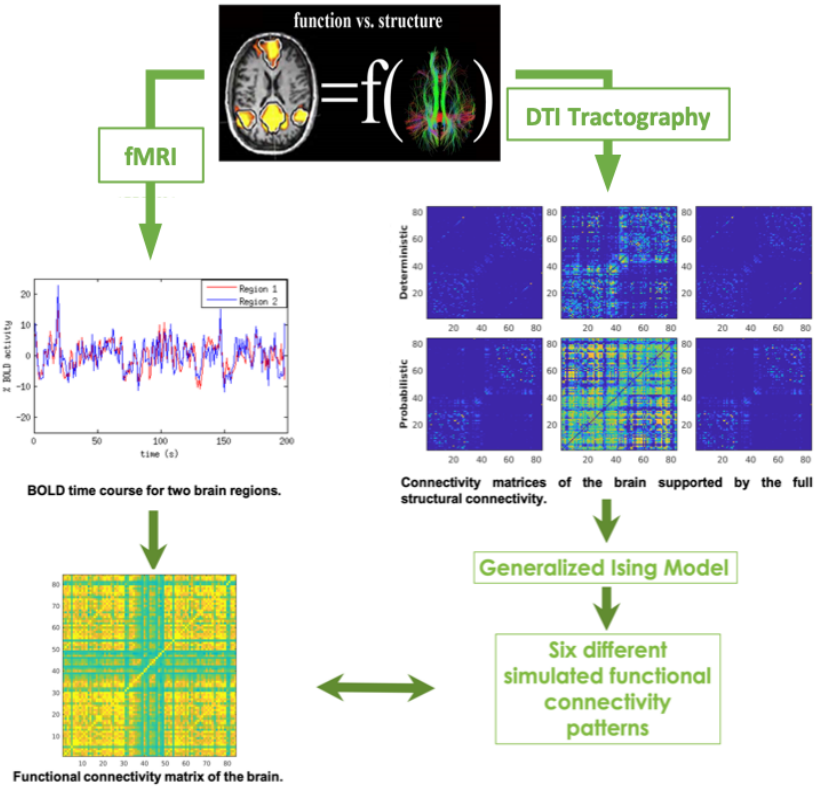

Figure 3.1: Summarized methodology

3.2.1 Data acquisition, preprocessing and tractography

Subjects

A set of sixty-nine healthy subjects, aged between 22 and 35 (with 41 women), were studied during wakefulness. Informed consent to participate in the study was obtained from every subject.

Ethic statement

The Ethics Committee of the Washington University and the University of Minnesota approved the study.

Functional MRI (fMRI)

Resting state fMRI images were acquired using high resolution 3T MR scans at the Washington University - University of Minnesota Consortium of the Human Connectome Project (WU-Minn HCP) [37, 38, 39, 40, 41, 42, 43]. Preprocessing of the data was performed using HCP pipelines, which implements Minimal Preprocessing Pipelines (MPP) [37] and single and multi-runICAF IX cleaning of MRI data. Minimal high pass filtering was applied with a cut-off of 2000s to perform temporal filtering [44]. Preprocessed data were parcellated into 84 regions using the AAL2 atlas FreeSurfer (a list of the labels is presented in Chapter 2, Appendix A.3). Next, a Blood Oxygen Level Dependent (BOLD) time series was extracted for each region. Pearson product-moment coefficient between each pair of time series was calculated, which provided the empirical correlation matrix (referred to later in the paper as the empirical functional correlation matrix). The parcellation procedure was performed using FSL, Freesurfer and MR-Trix toolbox; while the correlation calculation was performed using MATLAB (https://www.mathworks.com/).

Diffusion MRI

Diffusion weighted images were acquired using high resolution 3T MR scans at the Washington University - University of Minnesota Consortium of the Human Connectome Project (WU-Minn HCP). All processing steps for tractography reconstruction and generation of structural connectivity matrices were performed with MRTrix toolbox, version 3.0, considering anatomical information carried out from freesurfer parcellation for cortical regions, and estimates from FSLs FIRST tool for subcortical areas. To increase the biological accuracy of the reconstructions, processing steps taking advantage of the Anatomically-Constrained

Tractography (ACT) framework [45] were performed. Two different streamlines reconstruction approaches—probabilistic and deterministic [46]—have been performed on a Multi-Shell, Multi-Tissue Constrained Spherical Deconvolution fiber orientation distribution model [47, 48]. Reconstruction constraints were: maximum streamline length equal to 25 centimeters, streamlines seeds belonging to segmented white matter, and one million reconstructed streamlines per subject. All streamlines were mapped to the parcellated image to produce a structural connectome (which will hereafter be referred to as structural connectivity matrices), considering the number of streamlines as structural connectivity weight. In addition, fractional anisotropy (FA) derived from conventional diffusion tensor tractography at b-value 3000, has been mapped across probabilistic and deterministic streamlines, providing FA matrices that can be used as a proxy for structural connections integrity.

3.2.2 Data preparation and simulations

Data preparation

The generalized Ising model was implemented on six different input matrices (per subject) which were generated as follows. The first two matrices were generated by counting the fiber tracts between each pair of regions at b-value 3000 for probabilistic tractography and deterministic tractography. Secondly, FA matrix was used as a weighting parameter of the diffusion tractography for both tractography methods where the fiber counts were multiplied by the FA to generate the next set of matrices. Additionally, the generalized Ising model was implemented using just the FA matrices as inputs only for the comparison.

Model simulations

The generalized Ising model was simulated starting with a random spin configuration of size 1×L (L = 84). The spin configuration was placed in contact with a thermal bath of temperature T. Each spin could be in only one of the two spin states (either up (+1) or down (-1)). Not only

the equilibrium spin configuration but also thermodynamic properties of the system changes with respect to the temperature. The energy of this spin configuration can be calculated in the absence of an external magnetic field by Equation 3.1,

$$E = -\sum_{i,j=1}^{N} J_{ij} S_i S_j \tag{3.1}$$

where J_{ij} is the coupling between the i^{th} and j^{th} regions, S_i and S_j represent the spins of the i^{th} and j^{th} region respectively, and N = 84. Normalized structural connectivity matrices which were obtained from different tractography methods were used as the coupling J_{ij}. Generalized Ising model simulations were performed for each subject over a range of temperatures using Metropolis Monte Carlo algorithm (see further details of the simulations in [34]). Each simulation resulted in a time series for each of the spin site, permitting the calculation of a simulated correlation matrix using Pearson product-moment coefficient. Simulations were performed using six different J_{ij}s per subject by varying the temperature of the heat bath, which resulted in six categories of simulated data for 69 subjects. MATLAB code developed in-house (in MATLAB 2018b) (https://www.mathworks.com/) was used for all computer simulations.

3.2.3 Analysis

Analysis was performed at the subject level and average results (over the 69 subjects) were plotted. For the preliminary analysis, thermodynamic properties such as the magnetization, magnetic susceptibility, energy and the specific heat were calculated for the different generalized Ising model simulations. The magnetic susceptibility peak was used to identify the critical temperature (T_c) of the system.

For each category of simulations, the distance and the correlation coefficient between the simulated correlation distributions and the empirical correlation distribution were calculated as functions of temperature per subject. T_{min}, the temperature that minimizes the distance, and T_{max}, the temperature that maximizes the correlation coefficient, were obtained. A pairwise

t-test was performed in order to examine the significance of T_c, T_{min} and T_{max}. Next, the simulated correlation matrices at T_c, T_{min} and T_{max} were compared with the empirical correlation matrix. Additionally, emergence of the Resting State Networks (RSNs) [49, 50] were studied by comparing the RSNs with simulated data and empirical data. Furthermore, the correlation coefficients between the simulated data and the empirical data at T_c, T_{min} and T_{max} as well as the correlation coefficients between the empirical J_{ij}'s (structural connectivity matrices) and the empirical functional connectivity was plotted. The correlation coefficient was studied as a function of the threshold in all cases. Moreover, dimensionality of the six generalized Ising models (as explained in Appendix C.1) and the sparsity (ratio between the number of zero elements to all possible zeros in the matrix) of the corresponding J_{ij}s were calculated and compared across each set of data. Subsequently, simulated correlation was plotted as a function of the distance per tractography method.

3.3 Results

Figure 3.2 represents the input structural connectivity matrices for different tractography methods, mainly divided in to two categories as deterministic and probabilistic tractography. Structural connectomes generated by probabilistic tractography are distinguishable due to the lower sparsity of their matrices compared to those of the deterministic tractography.

Figure 3.3 shows a summary of the analysis for the generalized Ising model simulations using the structural connectivity obtained by deterministic tractography without FA. Equivalent figures summarizing the results for the other five categories of tractography are plotted and presented in Appendix B.2. Figure 3.3 (a) is a representation of the magnetic susceptibility as a function of temperature together with a vertical line illustrating the critical temperature. It is followed by the distance versus temperature plot in Figure 3.3 (b) that represents the position of T_{min}. Next, Figure 3.3 (c) shows the correlation coefficient between the empirical correlation matrix and the simulated correlation matrices at each temperature with a vertical line represent-

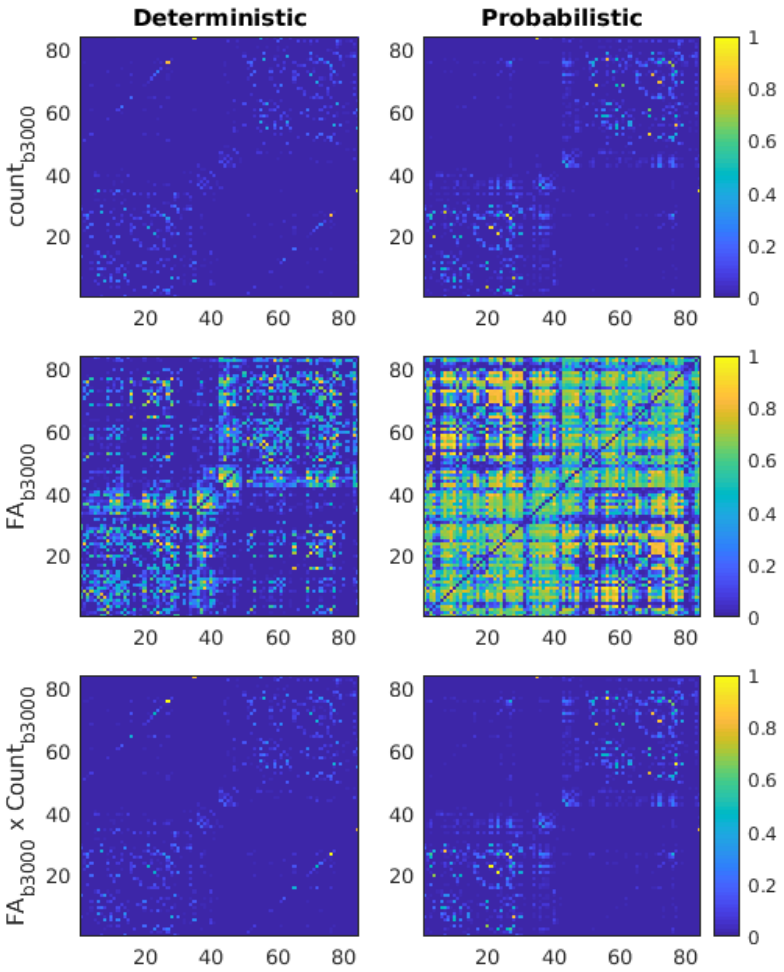

Figure 3.2: Structural connectivity matrices

ing T_{max}. Figures 3.3 (d), (e) and (f) present the simulated correlation matrices at T_c, T_{min} and T_{max} respectively while Figure 3.3 (h) presents the empirical correlation matrix. Figure 3.3 (g) illustrates the distributions of these three temperature categories for the 69 subjects.

Average temperatures, T_c, T_{min} and T_{max} for different simulations are presented in Table 3.1 while Table 3.2 represents the results from pairwise t-tests between different pairs of temperatures within the same category. Results of the t-test show that the three temperature values are not significantly different in all the categories except in probabilistic counts and FA.

Furthermore, a comparison between the correlation matrices at T_c, T_{min} and T_{max} with the empirical correlation matrix (Figure 3.3 (d), (e), (f) and Figure 3.3 (h)) was carried out by cal-

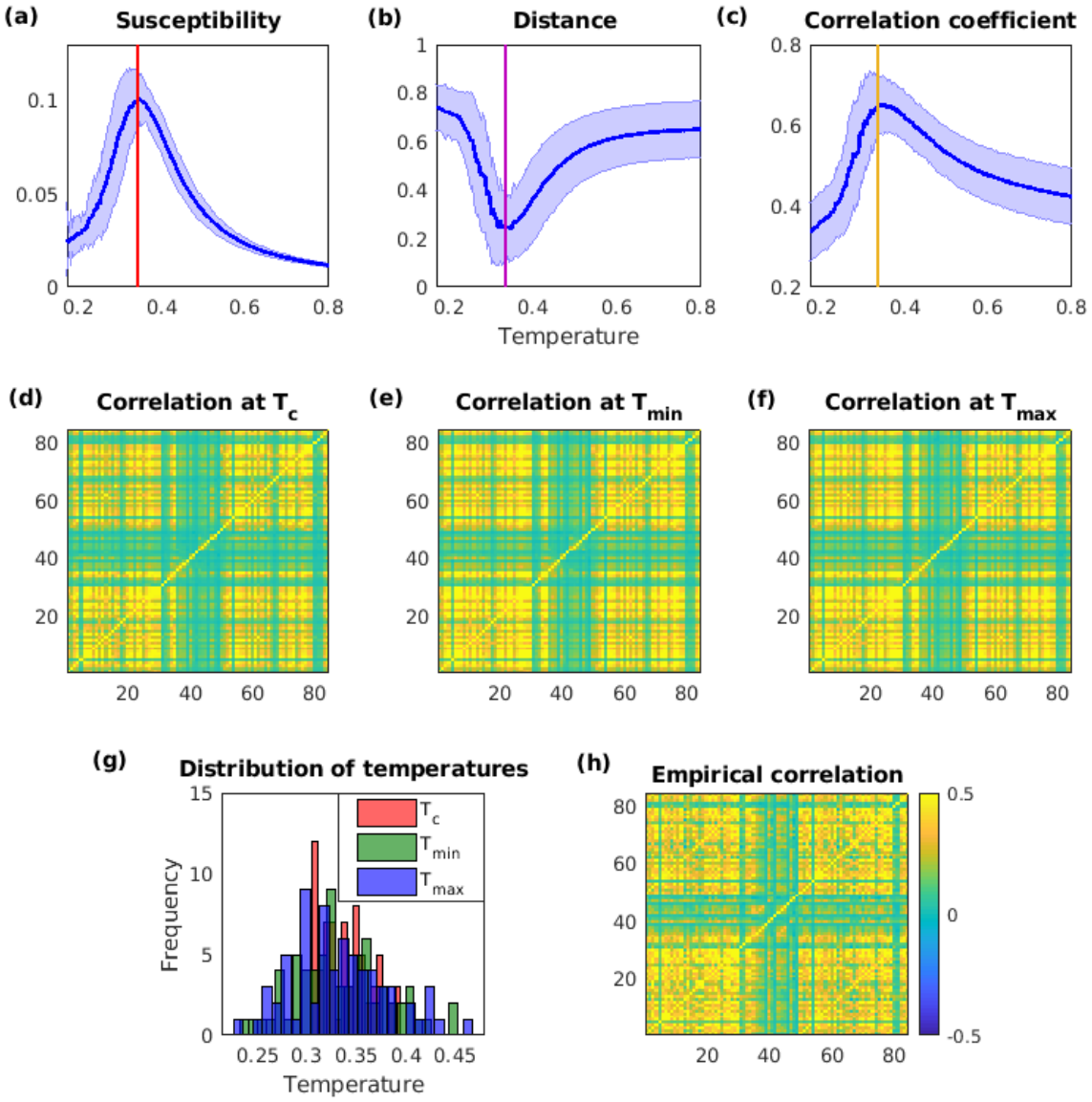

Figure 3.3: Summary of the analysis. (a) Average susceptibility as a function of temperature, (b) Distance between the simulated correlations and the empirical correlation as a function of temperature, (c) Correlation coefficient between the simulated correlations and the empirical correlations as a function of temperature, (d) (e) (f) (h) matrix representations of the correlation at T_c, T_{min} and T_{max} and empirical correlation respectively, (g) distribution of T_c, T_{min} and T_{max} within the group of 69 subjects

culating the correlation coefficient between each matrix and the empirical correlation matrix (Figure 3.4). There were no significant differences between the correlation coefficients at T_c,

Table 3.1: Average T_c, T_{min} and T_{max} for different methods

Temp.	Deterministic			Probabilistic		
	Count_{b3000}	FA_{b3000}	Count $\times FA$	Count_{b3000}	FA_{b3000}	Count $\times FA$
T_c	0.34 ± 0.02	5.89 ± 0.62	0.19 ± 0.02	0.81 ± 0.06	25.58 ± 2.29	0.91 ± 0.11
T_{min}	0.33 ± 0.05	5.55 ± 0.94	0.19 ± 0.04	0.73 ± 0.13	23.65 ± 4.16	0.86 ± 0.16
T_{max}	0.33 ± 0.05	6.20 ± 1.50	0.19 ± 0.03	0.76 ± 0.16	24.45 ± 3.42	0.87 ± 0.19

Table 3.2: p - values from the pairwise t-test to compare T_c, T_{min} and T_{max}

(a) Count_{b3000}

Det. \ Prob.	T_c	T_{min}	T_{max}
T_c	-	< 0.05	0.0239
T_{min}	0.4523	-	0.3336
T_{max}	0.3350	0.8494	-

(b) FA_{b3000}

Det. \ Prob.	T_c	T_{min}	T_{max}
T_c	-	< 0.05	0.0233
T_{min}	0.0133	-	0.2235
T_{max}	0.1169	0.0028	-

(c) Count × FA_{b3000}

Det. \ Prob.	T_c	T_{min}	T_{max}
T_c	-	0.0151	0.1264
T_{min}	0.3864	-	0.6272
T_{max}	0.5672	0.2126	-

T_{min} and T_{max} within one method. Figure 3.4 also includes the correlations between the empirical structural connectivity matrices and the empirical functional connectivity matrices. From this figure, it is evident that by introducing the generalized Ising model, predictability of the empirical correlation matrix increases on average from 0.2 to 0.6 compared to the predictability using the empirical connectivity matrix directly. Furthermore, the structural connectivity matrix that was generated using deterministic tractography without FA resulted in the highest correlation coefficient value of 0.65 between the simulated and empirical correlation matrices. A pairwise t-test indicated that there is no significant difference between the correlation coefficients obtained from probabilistic tractography counts and the weighted counts matrices by comparing the empirical and simulated functional connectomes as well as the empirical structural and functional connectomes with $p > 0.05$. All the other comparisons indicated a significant difference between the pairs with a $p < 0.05$ as presented in Figure 3.4.

To further illustrate the ability of the generalized Ising model to capture dynamics of the

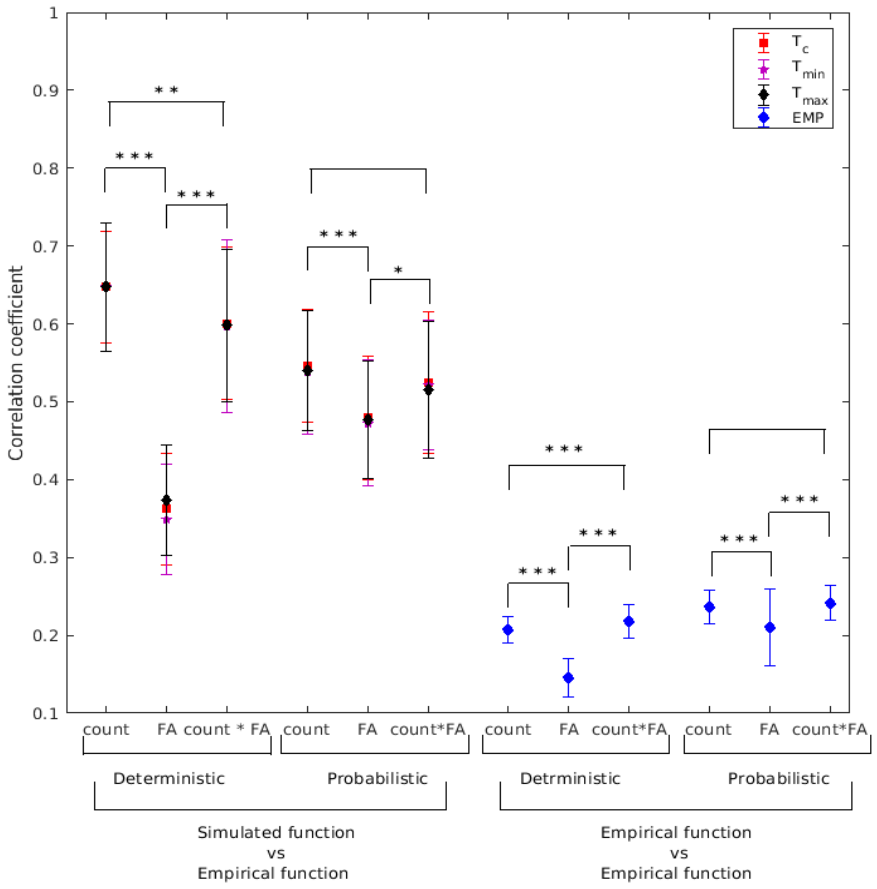

Figure 3.4: Average correlation coefficients (without using any threshold) between the simulated data (at Tc, Tmin and Tmax) and the empirical functional connectivity along with the correlation coefficient between the empirical structural connectivity and the empirical functional connectivity. * = $0.01 < p < 0.05$, ** = $0.001 < p < 0.01$ and *** = $p < 0.001$

resting brain, eight resting state networks (RSNs) are plotted in Figure 3.5 and Figure 3.6 side by side with the RSNs obtained from the empirical correlation matrix. The RSNs presented were obtained from the data that resulted through generalized Ising model simulations performed using connectomes generated by deterministic tractography. RSNs for other tractography methods are presented in Appendix B.3. From visual inspections, it can be seen that simulated correlations pick up most of the regions belonging to all the networks.

Matrix elements in the correlation matrices range from -1 to +1. Correlation coefficients between these correlation matrices (Figure 3.4) were calculated using the unthresholded corre-

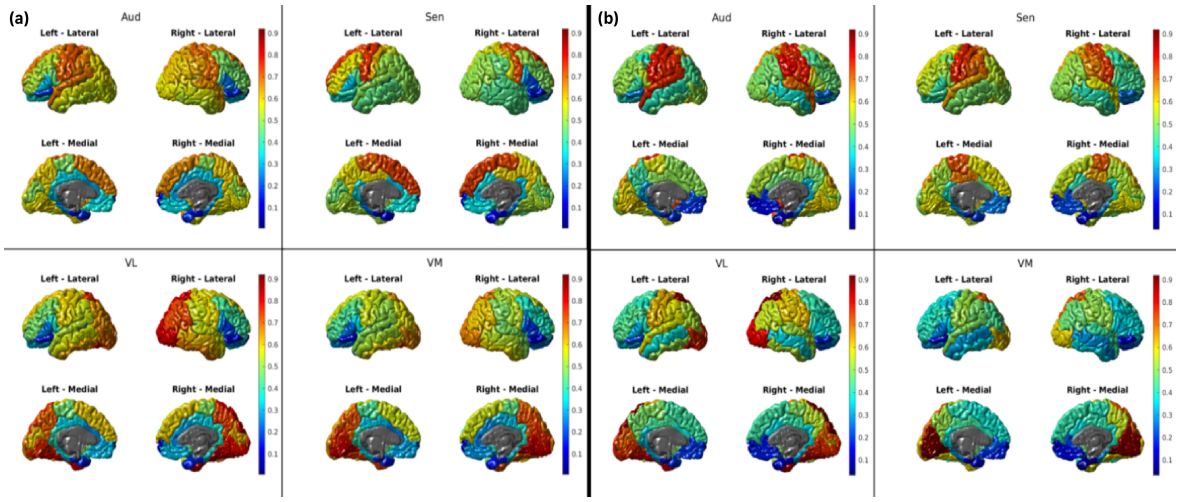

Figure 3.5: Auditory network (AUD), Sensorimotor network (Sen), Visual lateral and medial networks (VL, VM) obtained from (a) the simulated correlations (at T_c) and (b) the empirical correlations

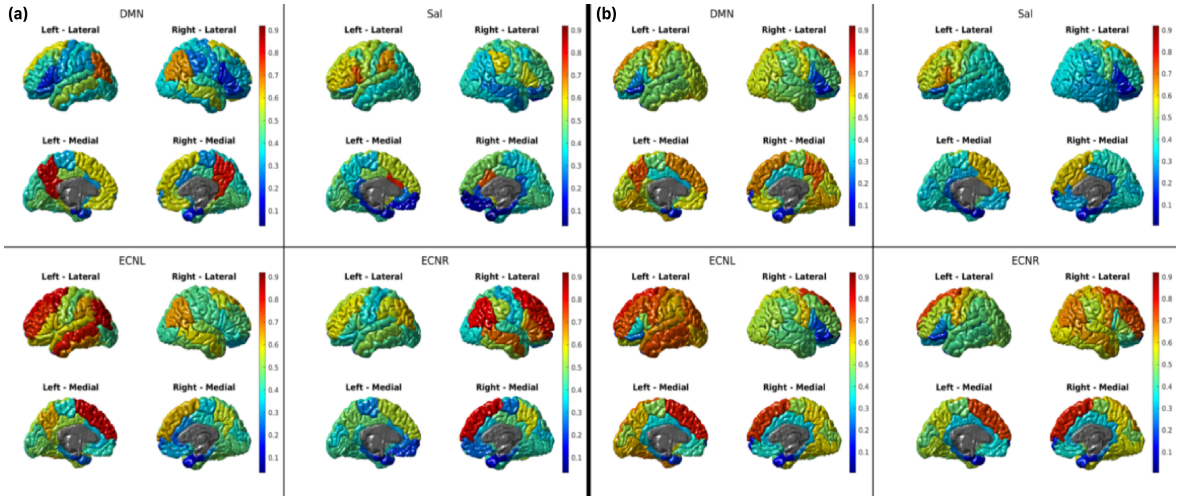

Figure 3.6: Default mode network (DMN), Salience network (Sal), External control network left and right (ECNL, ECNR) obtained from (a) the simulated correlations (at T_c) and (b) the empirical correlations

lation matrices. In order to illustrate the effect of thresholding correlation matrices, the correlation coefficient has been plotted in Figure 3.7 as a function of threshold for all the cases. When the threshold increases and reaches one, correlation coefficients of all the methods also reach approximately one due to the gradual increase of number of zeros in the correlation matrices. When threshold is equal to one, only the diagonal terms in the correlation matrices survive,

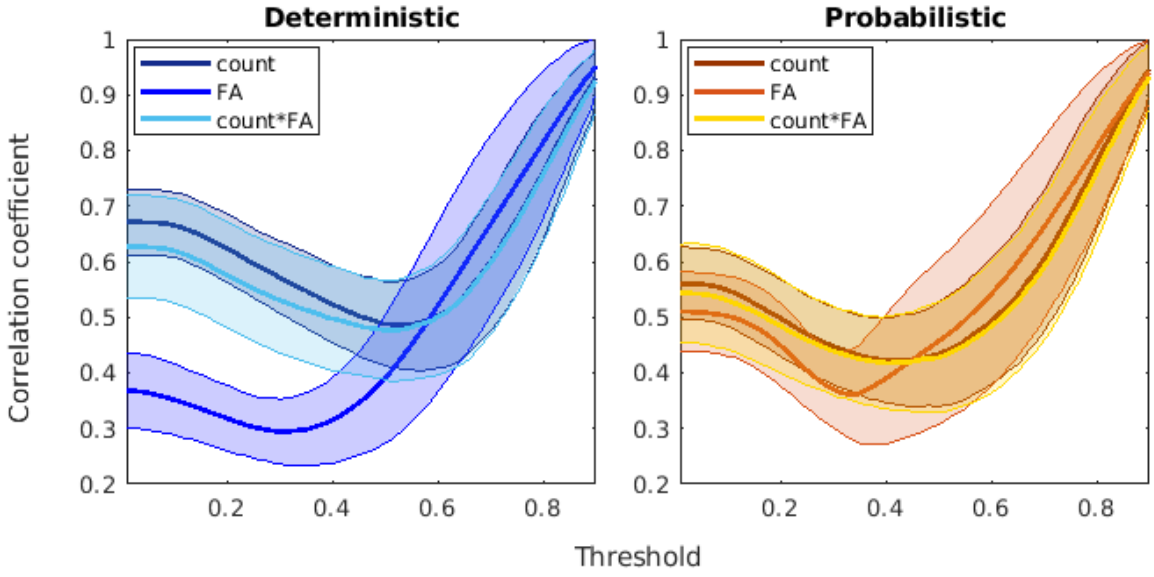

Figure 3.7: Mean correlation coefficients between the simulated data (at T_c) and the empirical functional connectivity as a function of threshold. Shaded area represents the standard deviation

while the rest of the elements are zero, resulting in a correlation coefficient of one. From this figure, it is evident that by using a threshold greater than 0.7, all the simulated correlation matrices will be able to predict the empirical correlation matrix equally well with an approximate correlation coefficient of 0.65 or greater.

Dimensionality together with sparsity can be used to investigate the nature of the structural connectivity matrix. To illustrate the effect of tractography in calculating the ”brain’s dimensionality”, dimensionality was calculated and compared among six different simulations (refer to Appendix C.1 for the calculation of dimensionality). Figure 3.8 provides a comparison of dimensionality and sparsity of the respective structural connectome with respect to the tractography method. It is evident that the dimensionality depends upon the method of tractography that has been used to extract the structural connectome. While the three structural connectomes generated using deterministic tractography had the same sparsity, the deterministic tractography method that gave the best prediction of the empirical functional correlation matrix resulted in a dimensionality ≈ 1 which was the lowest dimensionality obtained.

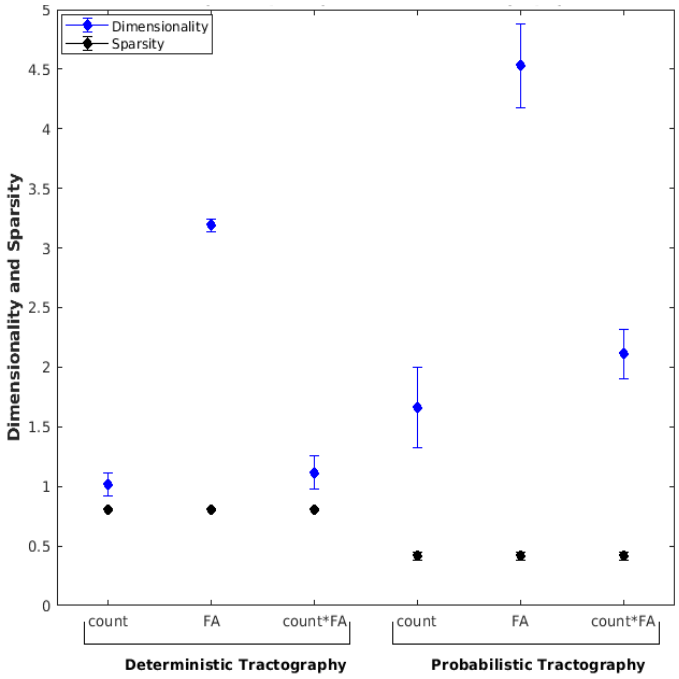

Figure 3.8: Dimensionality and sparsity for different tractography methods

From Figure 3.9 it can be observed that the correlation obtained by simulating the generalized Ising model on FA-based connectomes drops faster with the distance than do the correlations obtained by simulating the generalized Ising model on connectomes generated by either the counts or the weighted counts.

3.4 Discussion

Different types of tractography methods applied on DTI data acquired from the same subject enable to generate structural connectomes with different properties [15, 20]. These structural connectomes were then used in generalized Ising model simulations to predict the spontaneous fluctuations of the brain, resulted in varied predictabilities. Regardless of the variability in predictions among different tractography methods, a significant distinction in predictabilities that used the simulated functional connectome and the empirical structural connectome was observed. Our results of the correlation coefficient (Figure 3.4)—a quantitative measure of

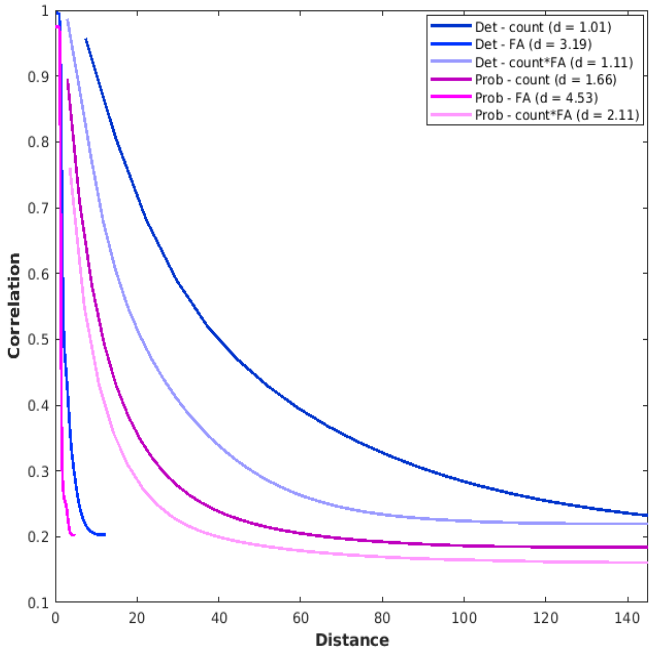

Figure 3.9: Correlation function at T_c as a function of distance for different tractography methods together with their respective dimensionality

predictability—signify a general improvement of predictions using the modelling approach rather than the direct comparisons of the empirical structural connectome with the empirical functional connectome. In addition of being able to predict the already existing functional connectivity using the structural architecture, application of modelling enables us to predict changes in the functional connectivity in place of a change in the structural connectivity. It is evident from the analysis that by changing the structural connectivity, resultant simulated functional connectivity at the critical temperature changes, and it still predicted the empirical functional correlations to a certain degree. Therefore, establishing a model to explain the observed functional correlations opens up different prospects to study the structure-function relationship of the brain such as predicting the changes of the functional correlations depending upon the alterations in the input structural connectivity.

Optimizing the generalized Ising model requires paying close attention to the only input of the model: the structural connectome of the brain. There exist different tractography methods

to obtain the structural connectome, but there is no evidence from research on the effects of increased or decreased connectivity implied by different tractography methods on the prediction. In the present work the generalized Ising model was implemented on six different connectomes, providing a study of criticality across different methods of structural connectome generation.

From the initial results of the simulations, criticality (critical temperatures Table 3.1) was identified using the magnetic susceptibility (Figure 3.3 (a)). Weights of the elements in input structural connectivity influenced the magnitude of critical temperature and hence the temperature ranges selected for simulations were different in each method. However, despite the changes in the input structural connectome, criticality exhibited the same characteristics in agreement with previous studies [35, 34]. Criticality of the Ising model has been discussed using theoretical as well as experimental evidence to illustrate that the interactions within the system tend to have a balance between integration and segregation at the critical temperature. According to previous studies, criticality can also be characterized by the maximum information transfer [51] and can be directly related to the idea of the brain functioning at criticality [52, 53], while maintaining a balance between inter- and intra-connections within and among the groups of neurons. This equivalence makes the comparison between the model at criticality and the dynamics of the brain feasible.

Robustness of the critical behavior was tested by calculating both the distance and the correlation coefficient between the simulated and the empirical functional connectivity matrices. Our results (in Table 3.1) showed that not only T_c but also T_{min} and T_{max} vary with the changes in the input structural connectome. Therefore, it will be important to consider the same tractography method when comparing healthy subjects with any other pathological condition. Paired t-test (Table 3.2) also demonstrated that T_c, T_{min} and T_{max} are not significantly different in the simulations where the structural connectomes generated by deterministic tractography was used. On the other hand, in the simulations where the probabilistic tractography was used, T_{min} and T_{max} were significantly different from T_c. Even though the three temperature parameters were significantly different in some cases, there was an overlap between the distributions of these

three different temperatures in each model (Figure 3.3 (g) and Figure B.1(g) - Figure B.5(g) in Appendix B.2). Hence, it can be inferred that the observed differences between T_c, T_{min} and T_{max} within each method were strictly due to the fluctuations of the structural connectivity within subjects. Even though the numerical values of these three temperatures differ between the methods, correlation matrices were not significantly different (Figure 3.3 (d)- (f)). In addition to that, our results showed that the simulated functional connectivity matrix and the empirical correlation matrix was alike (Figure 3.3 (h) and Figure 3.4), not only at T_c (ratifying prior work [34]) but also at T_{min} and T_{max}. Hence, T_{min} and T_{max} were also established as equivalent parameters to T_c which can be used to characterize the criticality of the generalized Ising model. This strongly indicates that the Ising model produces its best prediction of empirical data without the use of a fitting parameter—the critical temperature—a property embedded in the Ising model itself.

Deterministic tractography, when applied to obtain the structural connectome (without using FA as a weighing parameter), provided the least dense structural connectome compared to probabilistic tractography [15]. Despite being the matrix with lowest density, it provided the best prediction of the empirical functional connectivity matrix once used in generalized Ising model simulations, capturing about 65% of the empirical functional correlation matrix. On the other hand, regardless of the capability to account for the cross-fiber effects [20], probabilistic tractography provided a structural connectome which was not able to predict the empirical functional connectome to the extent a structural connectome generated using deterministic tractography could, through the generalized Ising model simulations. This could be due to the fact that bilateral connections are preserved more in deterministic tractography than in probabilistic tractography which could be the driving force of the critical behavior of the model.

This finding provides another perspective to look at the question of whether to use the deterministic tractography or the probabilistic tractography to generate the structural connectome from DTI data. Its important to stress here that our finding highly depends on the nature of adopted model as well as on the way in which the empirical correlation matrix is extracted. Of

course we should also mention that the way fMRI data were preprocessed to extract the neuronal component of the BOLD signal could also be relevant in determining the best matching. Although the deterministic tractography is said to have an increased number of false negatives [20], it is known to capture only the most relevant structural skeleton of the anatomical connections. Being able to obtain the best prediction of the empirical functional connectivity matrix by simulating the generalized Ising model using the connectome generated by deterministic tractography concludes that, for the simulations, it is sufficient to have information about only the most relevant connections or the true positives that are better identified in deterministic tractography than in probabilistic tractography. Furthermore, having a dense structural connectivity matrix (generated by probabilistic tractography), which may include a lot of false positive connections, could result in a comparatively low correlation coefficient between the simulated correlation matrices and the empirical functional correlation matrix.

Additionally, having the lowest predictability of the empirical functional correlation matrix despite the method of prediction (direct or through the generalized Ising model) and the method of tractography, it was validated that the FA matrix is not an adequate direct approximation of the structural connectome of the brain. Nevertheless, as proposed in [10], FA matrix could still be used as a weighting parameter of the structural connectivity matrix, even for the generalized Ising model simulations. Furthermore, our results showed that by applying a relevant threshold for the structural connectivity matrices generated using any of the six methods discussed in the manuscript, the predictability of the empirical functional correlation matrix can be improved. Calculated dimensionality values for different methods enabled us to further investigate the relationship between the structural connectome and the predictability. Within one tractography method (either the deterministic or the probabilistic), differences between the structural connectome and the best fit cannot be explained by sparsity of the matrix, but rather can be explained by the variations observed in dimensionality. Together with the correlation length, the dimensionality of an Ising model can describe how correlation between two spins decays with their distance. Dimensionality of the system seems to capture properties that cannot be cap-

tured by the sparsity itself. Understanding the role of dimensionality will necessarily require further investigation, but we believe it could bring important insights, especially in understanding deviation from a healthy connectome.

3.5 Conclusion

We can conclude that the generalized Ising model simulated using a structural connectome generated by either the deterministic tractography or the probabilistic tractography improves the prediction of the empirical correlation matrix with or without weighing the matrices using FA. Additionally, we could test that out of the six input matrices that have been analyzed using the generalized Ising model, deterministic tractography (without weighing by FA) provides the best prediction for the empirical functional correlation matrix. Calculation of dimensionality appears to be very informative to understanding the different performance of Ising models generated by different structural connectomes with the same sparsity. Finally, the possibilities offered by the model to predict the changes in functional connectivity matrix due to the changes in structural connectivity makes it pivotal to studying the spontaneous fluctuations of the brain in patients who suffered from severe brain injuries, or any other pathological conditions which produce fiber damage.

Acknowledgements

The authors acknowledge the Human Connectome Project (HCP) for providing the data. In particular, the data were provided by the HCP, WU-Minn Consortium (Principal Investigators: David Van Essen and Kamil Ugurbil; 1U54MH091657) funded by the 16 NIH Institutes and Centers that support the NIH Blueprint for Neuroscience Research; and by the McDonnell Center for Systems Neuroscience at Washington University. We thank the Natural Science and Engineering Research Council of Canada (NSERC) for the discovery grant and also the Canada Excellence Research Chairs (CERC).

Bibliography

[1] Derek K Jones and Alexander Leemans. Diffusion tensor imaging. In *Magnetic resonance neuroimaging*, pages 127–144. Springer, 2011.

[2] Lauren J O'Donnell and Carl-Fredrik Westin. An introduction to diffusion tensor image analysis. *Neurosurgery Clinics*, 22(2):185–196, 2011.

[3] R Douglas Fields. White matter matters. *Scientific American*, 298(3):54–61, 2008.

[4] Tonya White, Stefan Ehrlich, Beng-Choon Ho, Dara S Manoach, Arvind Caprihan, S Charles Schulz, Nancy C Andreasen, Randy L Gollub, Vince D Calhoun, and Vincent A Magnotta. Spatial characteristics of white matter abnormalities in schizophrenia. *Schizophrenia bulletin*, 39(5):1077–1086, 2012.

[5] Elisa Ambrosi, Chiara Chiapponi, Gabriele Sani, Giovanni Manfredi, Fabrizio Piras, Carlo Caltagirone, and Gianfranco Spalletta. White matter microstructural characteristics in bipolar i and bipolar ii disorder: A diffusion tensor imaging study. *Journal of affective disorders*, 189:176–183, 2016.

[6] Andrew L Alexander, Jee E Lee, Mariana Lazar, and Aaron S Field. Diffusion tensor imaging of the brain. *Neurotherapeutics*, 4(3):316–329, 2007.

[7] Denis Le Bihan, Jean-François Mangin, Cyril Poupon, Chris A Clark, Sabina Pappata, Nicolas Molko, and Hughes Chabriat. Diffusion tensor imaging: concepts and applications. *Journal of Magnetic Resonance Imaging: An Official Journal of the International Society for Magnetic Resonance in Medicine*, 13(4):534–546, 2001.

[8] Yaniv Assaf and Ofer Pasternak. Diffusion tensor imaging (dti)-based white matter mapping in brain research: a review. *Journal of molecular neuroscience*, 34(1):51–61, 2008.

[9] Gabriel A De Erausquin and Lucia Alba-Ferrara. What does anisotropy measure? insights from increased and decreased anisotropy in selective fiber tracts in schizophrenia. *Frontiers in integrative neuroscience*, 7:9, 2013.

[10] Toshinari Misaki, Takaaki Beppu, Takashi Inoue, Kuniaki Ogasawara, Akira Ogawa, and Hiroyuki Kabasawa. Use of fractional anisotropy value by diffusion tensor mri for preoperative diagnosis of astrocytic tumors: case report. *Journal of neuro-oncology*, 70(3):343–348, 2004.

[11] Anna C Alegiani, Simon MacLean, Hanna Braass, Susanne Siemonsen, Christian Gerloff, Jens Fiehler, Tae-Hee Cho, Laurent Derex, Marc Hermier, Yves Berthezene, et al. Comprehensive analysis of early fractional anisotropy changes in acute ischemic stroke. *PloS one*, 12(11):e0188318, 2017.

[12] Josep Puig, Gerard Blasco, Josep Daunis-Estadella, Götz Thomalla, Mar Castellanos, Guadalupe Soria, Alberto Prats-Galino, Javier Sánchez-González, Imma Boada, Joaquín Serena, et al. Increased corticospinal tract fractional anisotropy can discriminate stroke onset within the first 4.5 hours. *Stroke*, 44(4):1162–1165, 2013.

[13] SM Grieve, LM Williams, RH Paul, CR Clark, and E Gordon. Cognitive aging, executive function, and fractional anisotropy: a diffusion tensor mr imaging study. *American Journal of Neuroradiology*, 28(2):226–235, 2007.

[14] Thomas R Knösche, Alfred Anwander, Matthew Liptrot, and Tim B Dyrby. Validation of tractography: comparison with manganese tracing. *Human brain mapping*, 36(10):4116–4134, 2015.

[15] Maxime Descoteaux, Rachid Deriche, Thomas R Knosche, and Alfred Anwander. Deterministic and probabilistic tractography based on complex fibre orientation distributions. *IEEE transactions on medical imaging*, 28(2):269–286, 2009.

[16] Tim B Dyrby, Lise V Søgaard, Geoffrey J Parker, Daniel C Alexander, Nanna M Lind, William FC Baaré, Anders Hay-Schmidt, Nina Eriksen, Bente Pakkenberg, Olaf B Paulson, et al. Validation of in vitro probabilistic tractography. *Neuroimage*, 37(4):1267–1277, 2007.

[17] Peter J Basser, Sinisa Pajevic, Carlo Pierpaoli, Jeffrey Duda, and Akram Aldroubi. In vivo fiber tractography using dt-mri data. *Magnetic resonance in medicine*, 44(4):625–632, 2000.

[18] Olaf Sporns, Giulio Tononi, and Rolf Kötter. The human connectome: a structural description of the human brain. *PLoS computational biology*, 1(4):e42, 2005.

[19] Zhixi Li, Kyung K Peck, Nicole P Brennan, Mehrnaz Jenabi, Meier Hsu, Zhigang Zhang, Andrei I Holodny, and Robert J Young. Diffusion tensor tractography of the arcuate fasciculus in patients with brain tumors: comparison between deterministic and probabilistic models. *Journal of biomedical science and engineering*, 6(2):192, 2013.

[20] Sakh Khalsa, Stephen D Mayhew, Magdalena Chechlacz, Manny Bagary, and Andrew P Bagshaw. The structural and functional connectivity of the posterior cingulate cortex: Comparison between deterministic and probabilistic tractography for the investigation of structure-function relationships. *Neuroimage*, 102:118–127, 2014.

[21] Klaus Maier-Hein, Peter Neher, Jean-Christophe Houde, Marc-Alexandre Cote, Eleftherios Garyfallidis, Jidan Zhong, Maxime Chamberland, Fang-Cheng Yeh, Ying C Lin, Qing Ji, et al. Tractography-based connectomes are dominated by false-positive connections. *biorxiv*, page 084137, 2016.

[22] Andrew Zalesky, Alex Fornito, Luca Cocchi, Leonardo L Gollo, Martijn P van den Heuvel, and Michael Breakspear. Connectome sensitivity or specificity: which is more important? *Neuroimage*, 142:407–420, 2016.

[23] Arnaud Messé, David Rudrauf, Habib Benali, and Guillaume Marrelec. Relating structure and function in the human brain: relative contributions of anatomy, stationary dynamics, and non-stationarities. *PLoS computational biology*, 10(3):e1003530, 2014.

[24] Barry A Cipra. An introduction to the ising model. *The American Mathematical Monthly*, 94(10):937–959, 1987.

[25] Elena Antonova, Tonmoy Sharma, Robin Morris, and Veena Kumari. The relationship between brain structure and neurocognition in schizophrenia: a selective review. *Schizophrenia research*, 70(2-3):117–145, 2004.

[26] Changsong Zhou, Lucia Zemanová, Gorka Zamora-Lopez, Claus C Hilgetag, and Jürgen Kurths. Structure–function relationship in complex brain networks expressed by hierarchical synchronization. *New Journal of Physics*, 9(6):178, 2007.

[27] Makoto Fukushima, Richard F Betzel, Ye He, Martijn P van den Heuvel, Xi-Nian Zuo, and Olaf Sporns. Structure–function relationships during segregated and integrated network states of human brain functional connectivity. *Brain Structure and Function*, 223(3):1091–1106, 2018.

[28] Etay Hay, Petra Ritter, Nancy J Lobaugh, and Anthony R McIntosh. Multiregional integration in the brain during resting-state fmri activity. *PLoS computational biology*, 13(3):e1005410, 2017.

[29] Gustavo Deco, Mario Senden, and Viktor Jirsa. How anatomy shapes dynamics: a semi-analytical study of the brain at rest by a simple spin model. *Frontiers in computational neuroscience*, 6:68, 2012.

[30] Ruben Schmidt, Karl JR LaFleur, Marcel A de Reus, Leonard H van den Berg, and Martijn P van den Heuvel. Kuramoto model simulation of neural hubs and dynamic synchrony in the human cerebral connectome. *BMC neuroscience*, 16(1):54, 2015.

[31] Michael Breakspear. Dynamic models of large-scale brain activity. *Nature neuroscience*, 20(3):340, 2017.

[32] Daniele Marinazzo, Mario Pellicoro, Guo-Rong Wu, Leonardo Angelini, Jesus M Cortes, and Sebastiano Stramaglia. Information transfer of an ising model on a brain network. *BMC neuroscience*, 14(1):P376, 2013.

[33] S Stramaglia, M Pellicoro, L Angelini, E Amico, Hannelore Aerts, JM Cortés, S Laureys, and Daniele Marinazzo. Ising model with conserved magnetization on the human connectome: Implications on the relation structure-function in wakefulness and anesthesia. *Chaos: An Interdisciplinary Journal of Nonlinear Science*, 27(4):047407, 2017.

[34] Pubuditha M Abeyasinghe, Demetrius R de Paula, Sina Khajehabdollahi, Sree R Valluri, Adrian M Owen, and Andrea Soddu. Role of dimensionality in predicting the spontaneous behavior of the brain using the classical ising model and the ising model implemented on a structural connectome. *Brain connectivity*, 8(7):444–455, 2018.

[35] Daniel Fraiman, Pablo Balenzuela, Jennifer Foss, and Dante R Chialvo. Ising-like dynamics in large-scale functional brain networks. *Physical Review E*, 79(6):061922, 2009.

[36] Patric Hagmann, Leila Cammoun, Xavier Gigandet, Reto Meuli, Christopher J Honey, Van J Wedeen, and Olaf Sporns. Mapping the structural core of human cerebral cortex. *PLoS biology*, 6(7):e159, 2008.

[37] Matthew F Glasser, Stamatios N Sotiropoulos, J Anthony Wilson, Timothy S Coalson, Bruce Fischl, Jesper L Andersson, Junqian Xu, Saad Jbabdi, Matthew Webster, Jonathan R Polimeni, et al. The minimal preprocessing pipelines for the human connectome project. *Neuroimage*, 80:105–124, 2013.

[38] Mark Jenkinson, Christian F Beckmann, Timothy EJ Behrens, Mark W Woolrich, and Stephen M Smith. Fsl. *Neuroimage*, 62(2):782–790, 2012.

[39] Bruce Fischl. Freesurfer. *Neuroimage*, 62(2):774–781, 2012.

[40] Mark Jenkinson, Peter Bannister, Michael Brady, and Stephen Smith. Improved optimization for the robust and accurate linear registration and motion correction of brain images. *Neuroimage*, 17(2):825–841, 2002.

[41] Matthew F Glasser and David C Van Essen. Mapping human cortical areas in vivo based on myelin content as revealed by t1-and t2-weighted mri. *Journal of Neuroscience*, 31(32):11597–11616, 2011.

[42] David C Van Essen, Kamil Ugurbil, E Auerbach, D Barch, TEJ Behrens, R Bucholz, Acer Chang, Liyong Chen, Maurizio Corbetta, Sandra W Curtiss, et al. The human connectome project: a data acquisition perspective. *Neuroimage*, 62(4):2222–2231, 2012.

[43] Zoltan Nagy, Helena Westerberg, Stefan Skare, Jesper L Andersson, Anders Lilja, Olof Flodmark, Elisabeth Fernell, Kirsten Holmberg, Birgitta Böhm, Hans Forssberg, et al. Preterm children have disturbances of white matter at 11 years of age as shown by diffusion tensor imaging. *Pediatric Research*, 54(5):672, 2003.

[44] Stephen M Smith, Christian F Beckmann, Jesper Andersson, Edward J Auerbach, Janine Bijsterbosch, Gwenaëlle Douaud, Eugene Duff, David A Feinberg, Ludovica Griffanti, Michael P Harms, et al. Resting-state fmri in the human connectome project. *Neuroimage*, 80:144–168, 2013.

[45] Robert E Smith, Jacques-Donald Tournier, Fernando Calamante, and Alan Connelly. Anatomically-constrained tractography: improved diffusion mri streamlines tractography through effective use of anatomical information. *Neuroimage*, 62(3):1924–1938, 2012.

[46] J-Donald Tournier, Fernando Calamante, and Alan Connelly. Mrtrix: diffusion tractography in crossing fiber regions. *International Journal of Imaging Systems and Technology*, 22(1):53–66, 2012.

[47] Ben Jeurissen, Jacques-Donald Tournier, Thijs Dhollander, Alan Connelly, and Jan Sijbers. Multi-tissue constrained spherical deconvolution for improved analysis of multi-shell diffusion mri data. *NeuroImage*, 103:411–426, 2014.

[48] J-Donald Tournier, Chun-Hung Yeh, Fernando Calamante, Kuan-Hung Cho, Alan Connelly, and Ching-Po Lin. Resolving crossing fibres using constrained spherical deconvolution: validation using diffusion-weighted imaging phantom data. *Neuroimage*, 42(2):617–625, 2008.

[49] JS Damoiseaux, SARB Rombouts, F Barkhof, P Scheltens, CJ Stam, Stephen M Smith, and Cristian F Beckmann. Consistent resting-state networks across healthy subjects. *Proceedings of the national academy of sciences*, 103(37):13848–13853, 2006.

[50] MBCFDS De Luca, Christian F Beckmann, N De Stefano, PM Matthews, and Stephen M Smith. fmri resting state networks define distinct modes of long-distance interactions in the human brain. *Neuroimage*, 29(4):1359–1367, 2006.

[51] Daniele Marinazzo, Mario Pellicoro, Guorong Wu, Leonardo Angelini, Jesús M Cortés, and Sebastiano Stramaglia. Information transfer and criticality in the ising model on the human connectome. *PloS one*, 9(4):e93616, 2014.

[52] L De Arcangelis, F Lombardi, and HJ Herrmann. Criticality in the brain. *Journal of Statistical Mechanics: Theory and Experiment*, 2014(3):P03026, 2014.

[53] Paolo Moretti and Miguel A Muñoz. Griffiths phases and the stretching of criticality in brain networks. *Nature communications*, 4:2521, 2013.

Chapter 4

Will a Potts Model with q > 2 States Simulated on a Structural Connectome be Able to Better Predict the Spontaneous Fluctuations of the Brain?

4.1 Introduction

Over the past few decades, neuroscientists have been seeking an ideal methodology, informed by anatomy, for explaining the dynamical functions of the brain. According to prior research, the functions of the brain should highly depend upon its anatomical structure [1, 2]. However it is a fact that the structure and function of the brain do not share a complete one-to-one correlation throughout. The applications of mathematical modelling were proposed to explain the dynamics of the brain that could not be explained directly using the characteristics of underlying anatomy [3]. Modelling is useful not only in explaining the relationship between the structure and function of the brain, but also, more significantly, it is critical in predicting changes in the functional connectome due to changes in the brain structure [2].

In prior studies, the possibility of simulating functional connectivity of the brain using its structural connectivity was explored in different approaches. Among the models that have been driven by the structural connectome of the brain, a 2-dimensional Ising model simulated on a structural connectome is a well discussed approach [4, 5, 6, 7]. Initially introduced to explain the characteristics of ferromagnets [8], 2-dimensional Ising model was later used to infer global properties of the functional connectome of the brain [9], and then generalized and simulated on a structural connectome to predict the functional connectome. It is a very simple model, consisting of a collection of spins representing brain regions whose interaction strengths are defined by the characteristics of the structural connectivity. While the system is kept in a thermal bath, generalized Ising model simulations are able to well predict the functional correlation matrix of the brain when the temperature of the heat bath reaches a critical value [7].

On the other hand, Potts model is a generalization of the Ising model that was introduced in 1951 by Renfrey Potts to gain insight into the behavior of ferromagnets [10, 11] with the possibility of exploring different number of spin sites (q). The extra degrees of freedom added by the possible number of spin states increases the possibility of using the Potts model to explain different physical systems. Spin states are defined such that they are uniformly distributed about a circle. The Potts model has been studied extensively, using different numbers of possible spin states on different lattice configurations, and demonstrating the differences in characteristics [12, 13]. Mostly, Potts models with q = 3 and 4 have been studied to demonstrate how criticality changes from one model to another using different lattice configurations [14, 15]. While all these studies contribute to the understanding of properties of materials using the spin systems, we propose to further generalize the Potts model using structural connectome of the brain as an advancement to the generalized Ising model, and to thereby find the relationship between brain structure and function.

Dynamics are being introduced for the spin sites using Metropolis Monte Carlo algorithm to be able to predict the functional connectome using the generalized Ising model simulations.

Further a time series is generated for each spin site [7]. From the basic definition of the Ising model (which is a special case of the Potts model with q = 2), each spin is given the choice to be in one of the two available spin states, up or down [8]. Hence, when the dynamics are being introduced to the model, spin states can fluctuate with respect to time between only these two discrete states. This generates a time series as shown in Figure 4.1 (a) with only two possible states to fluctuate between. In contrast, empirical time series have no such restrictions on the number of states; rather, the fluctuations of the time series depend only upon the percentage activity of brain regions (Figure 4.1 (h)) which is believed to be a combination of neural activity, activity of astrocytes and the metabolic activity.

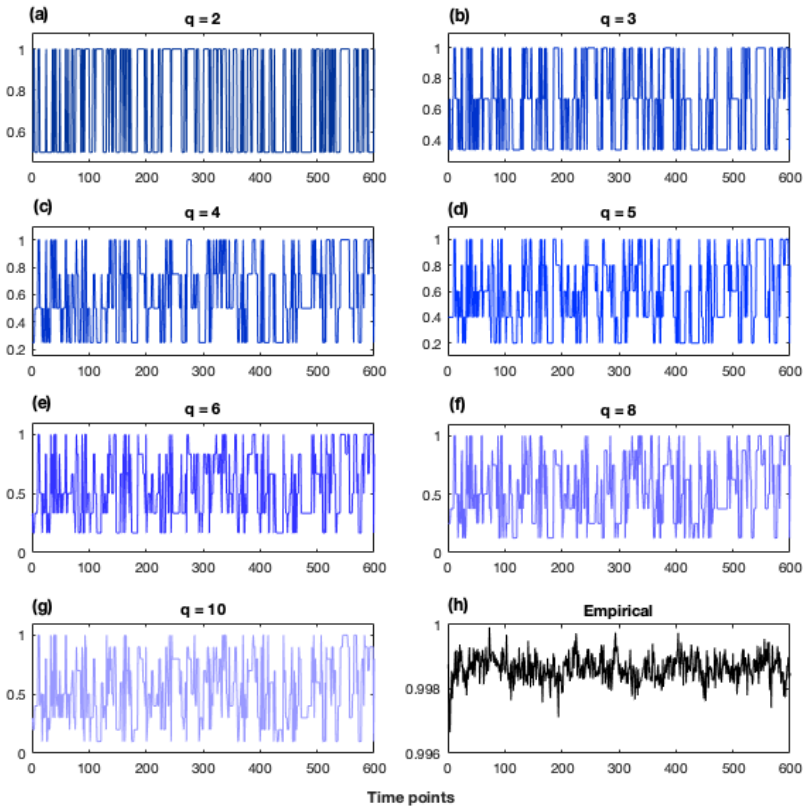

Figure 4.1: Simulated time series for different number of spin states together with the empirical time series. Plots represent the time series of a randomly selected region (40^{th} region for all cases). Number of time points shown (600) are half of the actual number of time points available

Therefore, one could hypothesize the generalization of the Potts model using more than 2 state spins to generate a time series more likely to have an analogue behavior similar to the empirical time series (Figure 4.1 (b - g)) that represents the activity of neurons, astrocytes and metabolism. Thus, our objective in this manuscript is to simulate the Potts model on a structural connectome with different number of spin states. En-route to generating an optimized model that is driven by the structural connectome of the brain to understand spontaneous fluctuations, it is important to examine all possible variations that could be incorporated in the model to improve the predictability. While we examine the impact of characteristics of the structural connectome in a parallel paper, in this manuscript we aim to address the question of what will be the impact of having a higher number of spin states on predicting the spontaneous fluctuations of the human brain through the correlations between time series.

4.2 Methodology

4.2.1 Data acquisition and preprocessing

Subjects

A set of sixty-nine healthy subjects, aged between 22 - 35 (with 41 women), were studied during wakefulness. Informed consent was obtained from all participants in the study.

Ethics statement

The Ethics Committee of Washington University and the University of Minnesota approved the study.

Acquisition and preprocessing

Resting state fMRI images and diffusion weighted images were acquired using high resolution 3T MR scans at the Washington University - University of Minnesota Consortium of the

Human Connectome Project (WU-Minn HCP) [16, 17, 18, 19, 20, 21]. Further details about preprocessing the structural and functional data can be found in [7]. Preprocessed data were parcellated into 84 individually labelled regions using AAL2 atlas in FSL [22].

Blood Oxygen Level Dependent (BOLD) time series were extracted for each region (using the preprocessed fMRI data). Pearson product-moment coefficient between each pair of time series was calculated to obtain the empirical correlation matrices. The average correlation matrix (averaged over 69 subjects) was used for the analysis (later in the paper we will refer to this as the empirical functional correlation matrix). The parcellation procedure was performed using FSL and Freesurfer, while the correlation calculation was performed using MATLAB (https://www.mathworks.com/).

Probabilistic streamlines reconstruction approach [23] have been performed on a Multi-Shell, Multi-Tissue Constrained Spherical Deconvolution fiber orientation distribution model [24, 25] to obtain the structural connectome from the preprocessed DTI data. All streamlines have been mapped to the parcellated image to produce a structural connectome, considering the number of streamlines as structural connectivity weight. The average structural connectome (averaged over 69 subjects) was used for simulations and the analysis.

4.2.2 Model simulations

We consider the simulations of the Potts model with q = 2, 3, 4, 5, 6, 8 and 10 on a structural connectome. Initially a vector of the size 1×84 was generated, and each spin site was assigned a random spin S_i. The value of S_i depended upon the number of states, q such that when q = 2, S_i = 1, 2 and when q = 3, S_i = 1, 2, 3 (and so on). The spin configuration was kept in a heat bath with a temperature T which controlled the properties of the system. The energy of such a configuration at state x in the absence of an external magnetic field can be calculated using the Equation 4.1.

$$E(x) = -\sum_{i,j=1}^{N} J_{ij}\delta_{S_i S_j} \tag{4.1}$$

where

$$\delta_{S_i S_j} = \begin{cases} 1, & \text{if } S_i = S_j \\ 0, & \text{otherwise} \end{cases} \tag{4.2}$$

and J_{ij} is coupling between the i^{th} and j^{th} region and s_i and s_j represent the spins of the i^{th} and j^{th} regions respectively.

Starting from a random spin configuration, the system was brought to a state with an equilibrium energy using the Metropolis Monte Carlo algorithm (MMC) [26, 27]. We ran 84×84×10 number of MMC steps at each temperature to ensure the spin configuration reached an equilibrium state. From the simulations, thermodynamic quantities such as energy (Equation 4.1), magnetization (Equation 4.3), specific heat (4.4) and susceptibility (Equation 4.5) were calculated using the respective equations. In equation 4.4, e is the energy per spin (E/N).

$$m(T) = <|\sum_{i=1}^{N} S_i|> \tag{4.3}$$

$$C(T) = \frac{N}{T^2}(< e^2 > - < e >^2) \tag{4.4}$$

$$\chi(T) = \frac{N}{T}(< m^2 > - < m >^2) \tag{4.5}$$

Subsequently, 84×1200 MMC steps were applied on the equilibrium spin configuration to introduce dynamics to the spins, assuming that the time it takes to run 84 MMC steps is equivalent to one TR. Hence, 1200 time points—which is equivalent to the number of time points obtained in the empirical time series—were generated for each spin site following the above step. Correlations between these time series calculated using Pearson product-moment

coefficient were used for further analysis. This procedure was repeated for 250 temperatures starting from 0.005 with an increment of 0.006. Moreover, the complete procedure described above was repeated ten times, each time starting with a different random spin configuration to explore the effects of different initial spin configurations. A total of 70 simulations (7×10 trials) of the generalized Potts model were carried out for seven different models with different number of spin states (q = 2, 3, 4, 5, 6, 8 and 10). All the simulations were carried out using Fortran code written by Dr. F. W. S. Lima, while the analysis was carried out using MATLAB 2018b.

4.2.3 Analysis

Analysis of the data were performed per model for each simulation separately and the results have been plotted for the average over the ten simulations per model. Initially the thermodynamic properties have been plotted and the critical temperatures (T_c) were located using the susceptibility versus temperature plots. For each model, the distance and the correlation coefficient between the simulated correlation matrices and the empirical correlation matrix was calculated as a function of temperature to locate the temperature that minimizes the distance (T_{min}) and the temperature that maximizes the correlation coefficient (T_{max}). Pairwise t-tests were performed to compare the significance of T_c, T_{min} and T_{max}. Next, the simulated correlation matrices and the correlation distribution at T_c were compared with the empirical correlation matrix and the correlation distribution. Moreover, spatial maps of RSNs are plotted and being compared with the empirical RSN maps for each model. Finally, a quantitative comparison was performed via the correlation coefficients between the simulated and the empirical results.

4.3 Results

All the results are presented as the average over the 10 independent simulations per model. First, by applying the MMC algorithm, the temperature dependence of energy, the magnetization, the specific heat and the susceptibility were calculated for each simulation and are presented in Figure 4.2. As observed from the susceptibility plots, the temperature at which the maximum change in magnetizations (or the maximum susceptibility) occur decreases as the number of spin states increases.

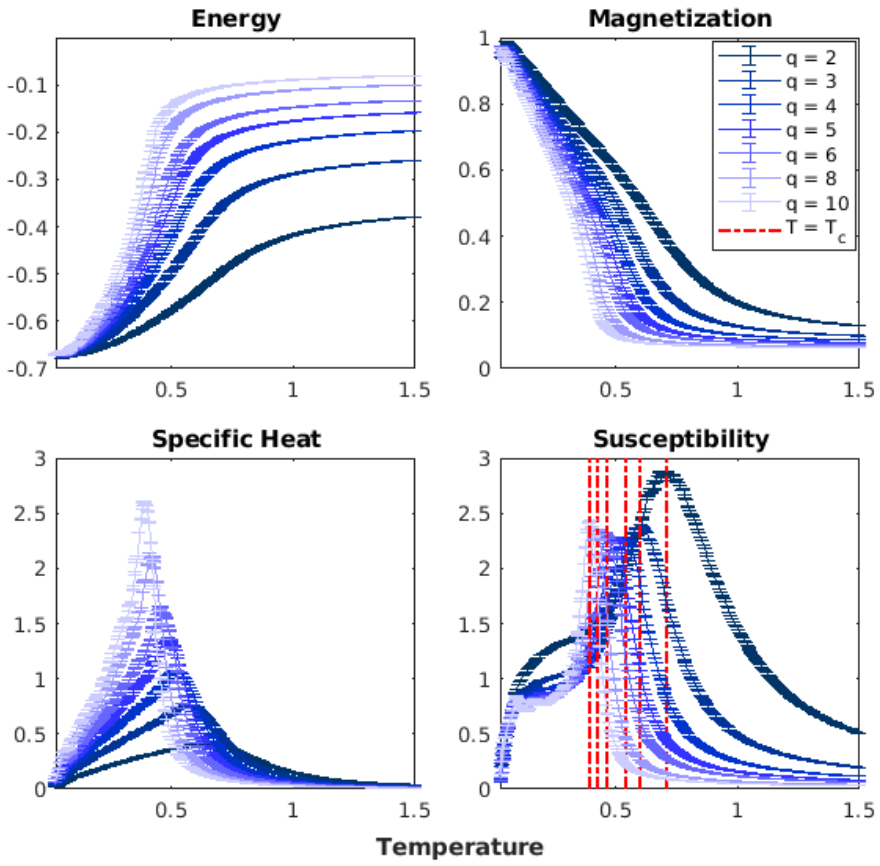

Figure 4.2: Thermodynamic properties for Potts models with different spin states. Red lined in the susceptibility plot indicates the temperature that gives the maximum susceptibility for different simulations

Next, Figure 4.3 illustrates how distance and the correlation coefficient between the empirical and simulated data varies with respect to the temperature of the heat bath. Distance and the correlation values represented in the figure are the average values (averaged over the ten independent simulations) and T_{min} and T_{max} (plotted in a vertical line) were obtained using the minimum and maximum values of the averaged plots, respectively. By calculating the distance and the correlation coefficient per temperature for each trial, T_{min} and T_{max}, the respective temperatures which minimized the distance and maximized the correlation were obtained. The average of the three temperature parameters T_c, T_{min} T_{max} that were obtained for ten independent simulations per model are recorded in Table 4.1.

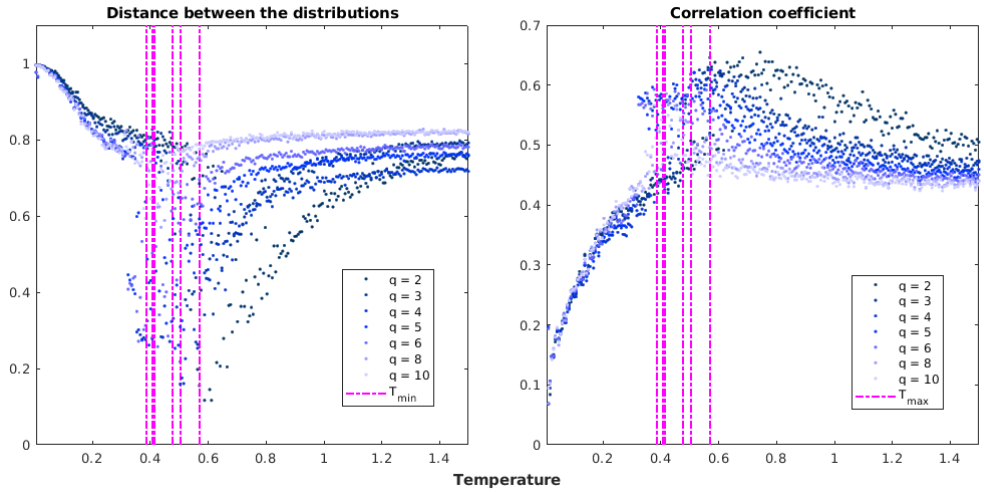

Figure 4.3: (a) Distance between the simulated and the empirical correlation matrices as a function of temperature (b) correlation between the simulated and the empirical correlation matrices at a function of temperature. Vertical dashed lines represent T_{min} and T_{max} respectively

Paired t-tests were performed to compare the significance between T_c, T_{min} and T_{max} in each situation, which resulted in mix outcomes. T_c, T_{min} and T_{max} were all significantly different in q = 2, 3, 4, 8 with $p < 0.05$. However, T_{min} and T_{max} were not significantly different in q = 5, 6, 10 with p =0.11, 0.20, 1 respectively. Furthermore, T_{max} and T_c were not significantly different in q =5 and 10 with p = 0.24 and 0.33, respectively.

Figure 4.4 illustrates the correlation matrices at the critical temperature T_c for each system

Table 4.1: Average T_c, T_{min} and T_{max} for different simulations

Number of states	T_c	T_{min}	T_{max}
2	0.708 ± 0.002	0.702 ± 0.004	0.739 ± 0.013
3	0.599 ± 0.001	0.503 ± 0.000	0.561 ± 0.007
4	0.540 ± 0.002	0.478 ± 0.049	0.584 ± 0.019
5	0.497 ± 0.001	0.408 ± 0.033	0.460 ± 0.094
6	0.461 ± 0.001	0.410 ± 0.034	0.390 ± 0.035
8	0.425 ± 0.001	0.413 ± 0.000	0.419 ± 0.001
10	0.395 ± 0.001	0.386 ± 0.009	0.386 ± 0.028

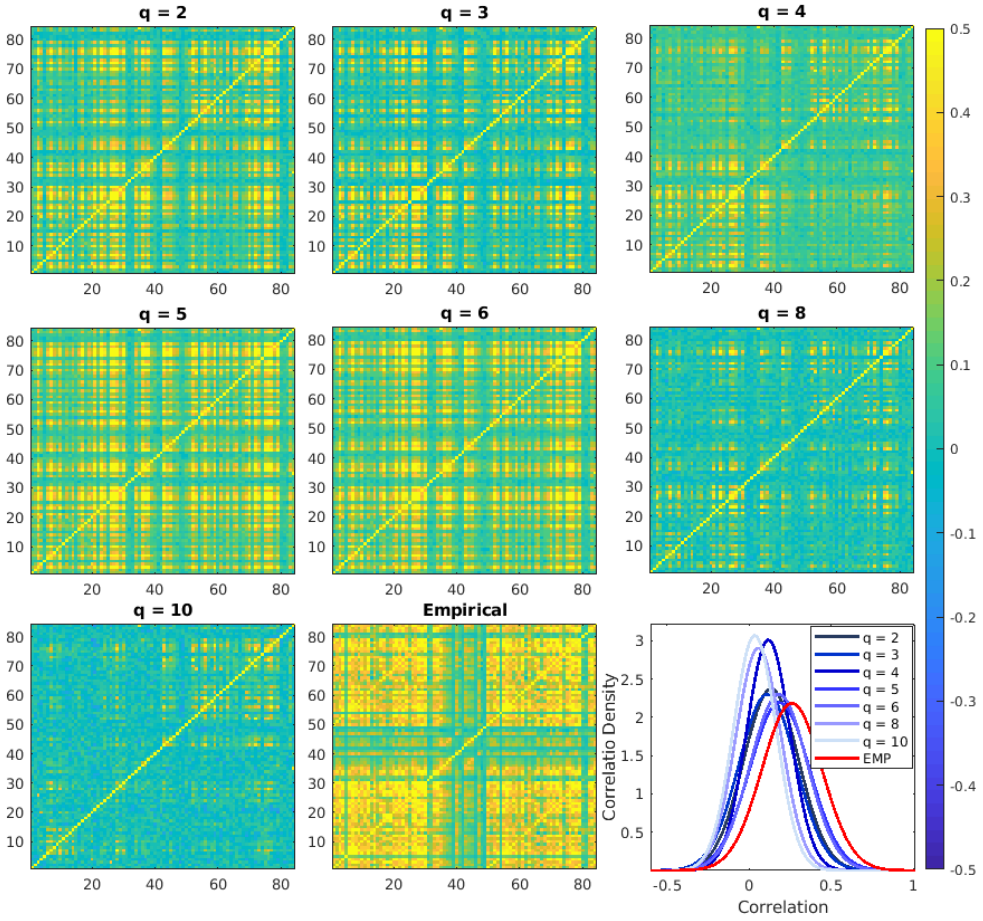

Figure 4.4: Correlation matrices at T_c for q = 2, 3, 4, 5, 6, 8 and 10 together with the empirical correlation matrix and the distribution of the correlations of each system with different number of spin states

with different numbers of spin states, along with the empirical correlation matrix. Additionally, it shows the distribution of correlations at T_c for each model together with the distribution of empirical correlation. It is evident from the distribution of correlations that systems with higher number of spin states tend to deviate further from the empirical correlation distribution, which supports the observed differences in correlation matrices.

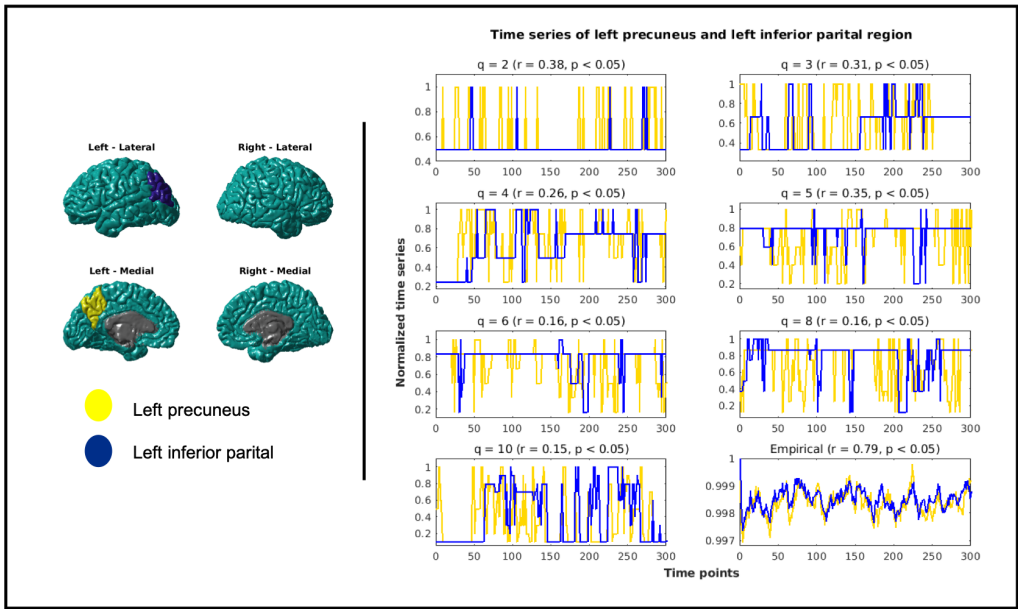

Figure 4.5: Simulated time series for left precuneus (yellow) and the left inferior parietal region (blue) (spatial positions are indicated on the brain in left) for seven different simulations along with that of the empirical data. Presented correlations are the correlations between the two time series

To study the correlations between the time series in more detail, time series belonging to two regions of the brain, the left precuneus and the left inferior parietal region—which are known to be highly correlated [28]—are presented in Figure 4.5 together with their respective correlations for each model and with that of the empirical data. We have plotted the time series up to 300 time points out of the 1200 time points only for better illustration purposes. Even though increasing the number of spin states creates a time series more relatable to the BOLD time series, it can be observed that the correlation between these two timeseries decreases as the number of spin states increases.

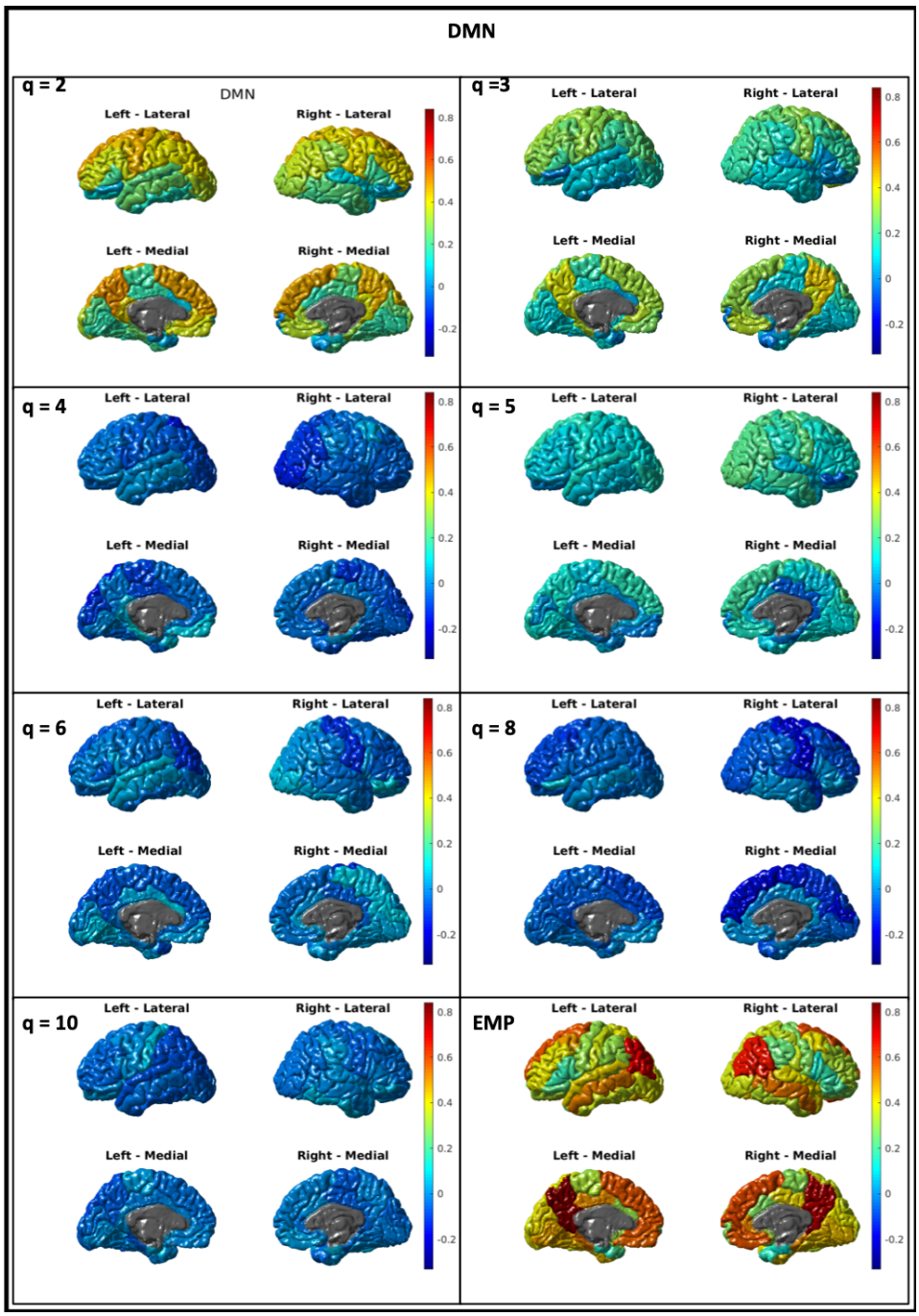

Figure 4.6: Brain maps of the default mode network for the simulated data at T_c for seven different systems together with the brain map of the empirical data

To further observe the degree to which the Potts models with different spin states can capture the dynamics of the brain, correlations obtained for one of the Resting State Networks (RSNs)—the default mode network (DMN)—were mapped on a brain for different model sim-

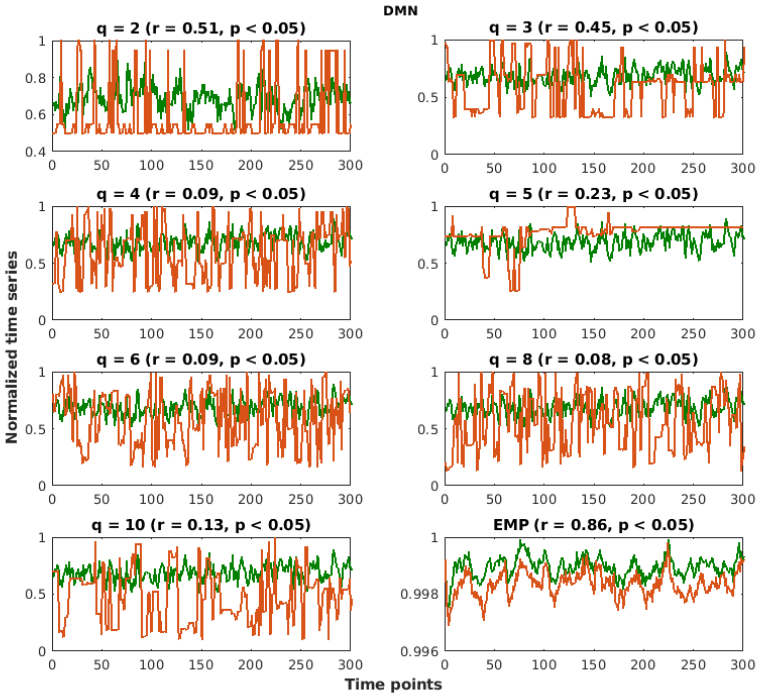

Figure 4.7: Average time series for the DMN is presented in green while the time series of the region that has the highest correlation with the average time series is presented in orange for all the models and the empirical data

ulations together with that of the empirical data in Figure 4.6. DMN comprises with the regions of the brain that activates when the brain is at "*rest*". It is a popular network to study as it had been observed in various studies across different platforms and, hence captured the attention of neuroscientists. In order to generate these brain maps, an average time course per network was initially created by averaging the time series of all the regions belonging to each RSN. Afterwards, correlation between each time series in the system and the averaged time series were calculated and plotted on a brain map. Brain maps for other RSNs are presented in Appendix C. Not surprisingly, the ability to capture RSNs decreases as the number of spin states increases, supporting the correlation matrices presented in Figure 4.4. Figure 4.7 demonstrates the calculation of the highest correlation plotted on brain maps for each model by presenting the average time series for the DMN, the time series of the best correlated region, and the correlation between the two. Time series plots for the rest of the networks are presented in

Appendix C. In these plots, more states than the actual number of states are visible since the time series plotted is the averaged time series over the ten trials.

Finally, the correlation coefficients between the empirical correlation and the simulated correlation were calculated (at T_c, T_{min} and T_{max}) and plotted in Figure 4.8. It is observed that the correlation coefficient between the simulated data at T_s and the empirical data decreases as the number of possible spin sites increases.

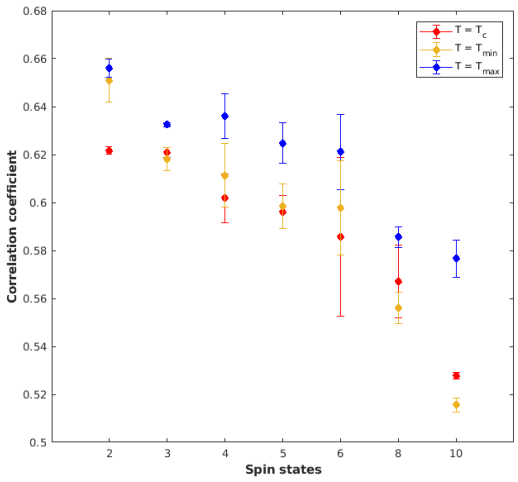

Figure 4.8: Correlation coefficient between the empirical correlation and the simulated correlations (at T_c, T_{min} and T_{max}) for the Potts models with different number of spin states

4.4 Discussion

Potts model simulations performed on a structural connectome with q = 2, 3, 4, 5, 6, 8 and 10 enabled us to compare the simulated data (at T_c) with the empirical data through Pearson product-moment coefficient calculated among the time series in each case. Our results clearly illustrated that increasing the number of spin states in the model does not increase the predictability of the spontaneous fluctuations in the brain using the simulations; rather, it decreases the predictability as the number of spin states increases. All the results supported the fact that the best model to predict the spontaneous fluctuations of the brain is a 2-state Potts

model (Ising model) simulated on a structural connectome, which further establishes the recent findings in [7].

All the results presented for the 2 state Potts model were consistent with the results presented in [7] for an Ising model simulated on a structural connectome. Furthermore, the trend observed in T_c obtained from the susceptibility curves presented in Figure 4.2 were consistent with the trend in [15] for q = 3 and 4, which shows a decrease in T_c when going from q = 3 to 4.

Figure 4.4 shows that the Potts model simulated on a structural connectome captures the pattern of the empirical correlation. However, the correlation decreases as the number of states increases. The distribution of correlation at T_c also shows a shift towards the left when the number of spin states increases. Correlations that are plotted in this figure in forms of matrices represent the correlation among time series of different brain regions. The effect of coupling on these different systems remains the same, as they were simulated on the same structural connectivity that has the characteristics of the structural architecture in the brain. However, for a particular temperature, when there are only two possible spin states in the system, the number of all possible equilibrium spin configurations is less than the number of all possible equilibrium spin configurations when the system has 10 spin states. This reduces the probability of having time series that are correlated with each other, which could be the reason for the decreasing correlations when the number of spin states increases. Figure 4.5 further supports this finding by illustrating a diminishing correlation between the time series of the left precuneus and the left inferior parietal region, which are known to be highly correlated [28].

Furthermore, Figure 4.8 clearly shows the decay in correlation coefficient between the empirical functional connectivity and the simulated functional connectivity at T_c. The highest correlation coefficient observed for data from 2-state Potts model simulations can be discussed further in terms of the connection between the BOLD time series and the actual neural activity.

BOLD time series does not directly measure the neural activity in the brain [29]. As explained in [30] it is believed that the neural activity convoluted with a hemodynamic response

function (HRF) results in the BOLD time series. On the other hand, at a fundamental level, the function of a neuron can also be characterized by action potentials, which have a digital nature and give rise to the local field potentials (LFP) that can be measured using neuroimaging techniques [31]. Hence, the functionality of a neuron can be thought to have a binary nature: as if it either passes a signal or stays inactive. Therefore, if the activity of a neuron can be directly monitored with respect to time, it would look like a binary time series with only two states—either active or inactive—and can be directly related to a time series generated by a 2-states Potts model or an Ising model.

The hypothesis that was tested in this manuscript was led by our understanding that the generalized Potts model generates a time series that predicts the BOLD time series. However, our results suggest that the 2-states Potts model (or an Ising model) controlled by the structural architecture could be predicting the neural activity directly, rather than indirectly, as is achieved by the BOLD time series. To investigate it further, it would be beneficial as a next step to convolve the simulated time series with an HRF and compare the resultant with the empirical BOLD time series.

4.5 Conclusion

Model that generates the highest correlation coefficient for the comparison between the simulated data and the empirical data is the generalized Ising model which has only to state spins. Increasing the number of spin states decreases the predictability of the empirical functional correlation matrix. Generalized Ising model could be capturing the digital nature of the neuronal activity rather than the analogue behavior of the BOLD signal which not only reflects the neural activity but a combination of the neural activity, activity of astrocytes and the metabolic functions.

Acknowledgements

The authors acknowledge the Human Connectome Project (HCP) for providing the data. In particular, the data were provided by the HCP, WU-Minn Consortium (Principal Investigators: David Van Essen and Kamil Ugurbil; 1U54MH091657) funded by the 16 NIH Institutes and Centers that support the NIH Blueprint for Neuroscience Research; and by the McDonnell Center for Systems Neuroscience at Washington University. We thank the Natural Science and Engineering Research Council of Canada (NSERC) for the discovery grant and also the Canada Excellence Research Chairs (CERC). Additionally we would like to thank Dr. F. W. S. Lima from Universidade Federal do Piau, Brazil for providing the Fortran code for the Potts model simulations.

Bibliography

[1] Hae-Jeong Park and Karl Friston. Structural and functional brain networks: from connections to cognition. *Science*, 342(6158):1238411, 2013.

[2] Kanika Bansal, Johan Nakuci, and Sarah F Muldoon. Personalized brain network models for assessing structure–function relationships. *Current opinion in neurobiology*, 52:42–47, 2018.

[3] Daniel J Amit. *Modeling brain function: The world of attractor neural networks*. Cambridge university press, 1992.

[4] Gustavo Deco, Mario Senden, and Viktor Jirsa. How anatomy shapes dynamics: a semi-analytical study of the brain at rest by a simple spin model. *Frontiers in computational neuroscience*, 6:68, 2012.

[5] Daniele Marinazzo, Mario Pellicoro, Guorong Wu, Leonardo Angelini, Jesús M Cortés, and Sebastiano Stramaglia. Information transfer and criticality in the ising model on the human connectome. *PloS one*, 9(4):e93616, 2014.

[6] Sebastiano Stramaglia, Mario Pellicoro, Leonardo Angelini, Enrico Amico, Hannelore Aerts, JM Cortés, Steven Laureys, and Daniele Marinazzo. Ising model with conserved magnetization on the human connectome: Implications on the relation structure-function in wakefulness and anesthesia. *Chaos: An Interdisciplinary Journal of Nonlinear Science*, 27(4):047407, 2017.

[7] Pubuditha M Abeyasinghe, Demetrius R de Paula, Sina Khajehabdollahi, Sree R Valluri, Adrian M Owen, and Andrea Soddu. Role of dimensionality in predicting the spontaneous behaviour of the brain using the classical ising model and the ising model implemented on the structural connectome. *Brain connectivity*, (ja), 2018.

[8] Barry A Cipra. An introduction to the ising model. *The American Mathematical Monthly*, 94(10):937–959, 1987.

[9] Daniel Fraiman, Pablo Balenzuela, Jennifer Foss, and Dante R Chialvo. Ising-like dynamics in large-scale functional brain networks. *Physical Review E*, 79(6):061922, 2009.

[10] Fa-Yueh Wu. The potts model. *Reviews of modern physics*, 54(1):235, 1982.

[11] FY Wu. Potts model of magnetism. *Journal of Applied Physics*, 55(6):2421–2425, 1984.

[12] Clive F Baillie and Paul D Coddington. Comparison of cluster algorithms for two-dimensional potts models. *Physical Review B*, 43(13):10617, 1991.

[13] Nuno AM Araújo, Roberto FS Andrade, and Hans J Herrmann. q-state potts model on the apollonian network. *Physical Review E*, 82(4):046109, 2010.

[14] PRO Da Silva, FWS Lima, and RN Costa Filho. Potts model with q= 3 and 4 states on directed small-world network. *Computer Physics Communications*, 184(12):2746–2750, 2013.

[15] RM Marques, FWS Lima, and Raimundo N Costa Filho. Potts model on directed small-world voronoi–delaunay lattices. *Physica A: Statistical Mechanics and its Applications*, 451:295–304, 2016.

[16] Matthew F Glasser, Stamatios N Sotiropoulos, J Anthony Wilson, Timothy S Coalson, Bruce Fischl, Jesper L Andersson, Junqian Xu, Saad Jbabdi, Matthew Webster, Jonathan R Polimeni, et al. The minimal preprocessing pipelines for the human connectome project. *Neuroimage*, 80:105–124, 2013.

[17] Mark Jenkinson, Christian F Beckmann, Timothy EJ Behrens, Mark W Woolrich, and Stephen M Smith. Fsl. *Neuroimage*, 62(2):782–790, 2012.

[18] Bruce Fischl. Freesurfer. *Neuroimage*, 62(2):774–781, 2012.

[19] Mark Jenkinson, Peter Bannister, Michael Brady, and Stephen Smith. Improved optimization for the robust and accurate linear registration and motion correction of brain images. *Neuroimage*, 17(2):825–841, 2002.

[20] Matthew F Glasser and David C Van Essen. Mapping human cortical areas in vivo based on myelin content as revealed by t1-and t2-weighted mri. *Journal of Neuroscience*, 31(32):11597–11616, 2011.

[21] David C Van Essen, Kamil Ugurbil, E Auerbach, D Barch, TEJ Behrens, R Bucholz, Acer Chang, Liyong Chen, Maurizio Corbetta, Sandra W Curtiss, et al. The human connectome project: a data acquisition perspective. *Neuroimage*, 62(4):2222–2231, 2012.

[22] R Cameron Craddock, G Andrew James, Paul E Holtzheimer III, Xiaoping P Hu, and Helen S Mayberg. A whole brain fmri atlas generated via spatially constrained spectral clustering. *Human brain mapping*, 33(8):1914–1928, 2012.

[23] J-Donald Tournier, Fernando Calamante, and Alan Connelly. Mrtrix: diffusion tractography in crossing fiber regions. *International Journal of Imaging Systems and Technology*, 22(1):53–66, 2012.

[24] Ben Jeurissen, Jacques-Donald Tournier, Thijs Dhollander, Alan Connelly, and Jan Sijbers. Multi-tissue constrained spherical deconvolution for improved analysis of multi-shell diffusion mri data. *NeuroImage*, 103:411–426, 2014.

[25] J-Donald Tournier, Chun-Hung Yeh, Fernando Calamante, Kuan-Hung Cho, Alan Connelly, and Ching-Po Lin. Resolving crossing fibres using constrained spherical deconvolution: validation using diffusion-weighted imaging phantom data. *Neuroimage*, 42(2):617–625, 2008.

[26] Nicholas Metropolis, Arianna W Rosenbluth, Marshall N Rosenbluth, Augusta H Teller, and Edward Teller. Equation of state calculations by fast computing machines. *The journal of chemical physics*, 21(6):1087–1092, 1953.

[27] Harvey Gould, Jan Tobochnik, Dawn C Meredith, Steven E Koonin, Susan R McKay, and Wolfgang Christian. An introduction to computer simulation methods: applications to physical systems. *Computers in Physics*, 10(4):349–349, 1996.

[28] Leila Glass, Ashley L Ware, and Sarah N Mattson. Neurobehavioral, neurologic, and neuroimaging characteristics of fetal alcohol spectrum disorders. In *Handbook of clinical neurology*, volume 125, pages 435–462. Elsevier, 2014.

[29] Nikos K Logothetis, Jon Pauls, Mark Augath, Torsten Trinath, and Axel Oeltermann. Neurophysiological investigation of the basis of the fmri signal. *Nature*, 412(6843):150, 2001.

[30] Johanna M Zumer, Matthew J Brookes, Claire M Stevenson, Susan T Francis, and Peter G Morris. Relating bold fmri and neural oscillations through convolution and optimal linear weighting. *Neuroimage*, 49(2):1479–1489, 2010.

[31] Nikos K Logothetis and Josef Pfeuffer. On the nature of the bold fmri contrast mechanism. *Magnetic resonance imaging*, 22(10):1517–1531, 2004.

Chapter 5

Discussion and Future Work

5.1 Discussion

Analogous to prior studies, critical behavior of the model was verified through the observation of basic properties in the system such as magnetic susceptibility [1], specific heat [2], and transfer entropy [3, 4], which provided the critical temperature T_c. In addition to these basic properties of a static Ising model, the critical behavior was shown to be conserved even after introducing the dynamics to the model: after generating time series per spin site, assessed T_{min} and T_{max} values were not significantly different from T_c [5]. T_{min} was the temperature that minimized the distance between the simulated correlation matrix and the empirical correlation matrix, while T_{max} was the temperature that maximized the correlation coefficient between the simulated correlation matrix and the empirical correlation matrix. Hence, an optimized generalized Ising model allowed us to predict the functional correlation matrix of the brain—which represents the brain's spontaneous fluctuations—using a structural connectivity matrix not only at T_{min} and T_{max} which are fitting parameters, but also at the critical temperature (T_c) which is a property embedded in the Ising model.

In agreement with previous research [3, 4, 2], our results indicated a phase transition (from an ordered phase to a disordered phase) in the simulated data at T_c using the order parameter

(the magnetization), where other thermodynamic quantities such as specific heat and susceptibility were peaked. At sub-critical temperatures, since the system was in a very low energy state, the spins do not interact with each other even if they were highly structurally connected. At super-critical temperatures, the system was at a very high energy state and hence influenced only minimally by the underlying structural connectivity. Between these two extremes, at the critical temperature, underlying structural connectivity influenced the interactions among spins such that there was a balance between integration and segregation among the spin populations evolving to optimize the functions of the system. On the other hand, the brain is believed to function at the criticality with maximum information transfer and a balance between integration and segregation among the neuronal populations [6, 7, 8, 9]. This understanding made it possible to predict the functional correlation matrix of the brain using the simulated functional correlation at T_c (or T_{min} and T_{max}).

In addition to using susceptibility of the generalized Ising model to obtain T_c or the state of the model that best predicts the functional connectivity of brain, the method of using the global degree to find the criticality was introduced. Susceptibility and specific heat measures the changes in the fundamental quantities of the model, magnetization and energy respectively [1, 10]. In studies that involved the static Ising model simulations, the critical temperature was obtained most commonly using the susceptibility or specific heat [10, 2, 5] as discussed previously. After introducing the dynamics to the model, our results concluded that the global degree shows a similar variation as the specific heat, not only by maximizing the degree at the critical temperature, but also by producing a cumulative integral that follows a similar pattern as the energy. This presented the possibility of finding a relationship between the thermodynamic quantities and a fundamental graph theoretical property through the Ising model.

Dimensionality of a healthy brain was calculated to be *two* using a novel method that depends upon a new definition of distance between each pair of regions of the brain, and is defined from their structural connectivity. The method of calculation was developed by ob-

serving the critical behavior of the generalized Ising model and studying the variations of the system around criticality [5]. The dimensionality of a system plays a key role in controlling the functions of any system [11], while the definition of dimensionality can depend upon the system itself. One method of defining the dimensionality of neural data is by observing the reactivity of neurons to stimuli [12]. For example, neurons that are highly specialized and only react to specific stimuli are known to have low dimensions, while neurons that respond to stimuli with mixed selectivity are said to be high-dimensional [13]. Another common method for studying dimensionality is to use Principle Component Analysis (PCA) [14]. In PCA, dimensionality is introduced as the number of random variables that explain the neural activity. PCA is used to reduce this number of random variable (dimensionality reduction) by isolating only a set of principle variables [15, 16]. In any of these definitions, dimensionality does not directly depend upon the anatomy of the brain, but rather depends upon the number of random variables or the features that can be inferred from the functional brain imaging data.

In contrast, our dimensionality calculation algorithm directly depends upon the structural connectivity of the brain because, at criticality, the behavior of the system is controlled by the structural connectivity. In evidence of this claim, the effects of different structural connectivity matrices on the calculation of dimensionality was studied by comparing the generalized Ising model simulations using six different structural connectivity matrices (Chapter 3). Our results demonstrated that different types of tractography methods implemented on the same DTI data can yield different dimensionality—which could vary from 1 to 2.5—while concluding also that there is no direct relationship between the predictability of the model and the dimensionality. Therefore, for future studies that implement the calculation of dimensionality, it could be informative to explore and compare the generalized Ising model simulations using structural connectivity obtained by different tractography methods. Dimensionality could be advantageous when simulating the Ising model on an altered structural connectivity caused by a pathological situation or an accidental brain injury: dimensionality could identify the level of impact to the spontaneous brain fluctuations from the alteration in the structural connectome.

Characterizing the functional connectivity matrix using the structural connectivity of the brain through the Ising model simulations enabled us to increase the predictability of the functional connectivity matrix in contrast to direct comparisons of the empirical structural and functional connectivity matrices. Even though the generalized Ising model was proven to predict the empirical functional connectivity matrix at the critical temperature in previous studies [1, 3, 4, 2], the improvement in predictability was not quantitatively assessed in parallel to the direct comparisons. In addition to corroborating the previous findings, our analysis provided a quantitative measure to illustrate how modelling can improve the predictability of the empirical functional connectivity using the structural connectivity of the brain.

Furthermore, it was concluded that a generalized Ising model simulated with a structural connectome generated using deterministic tractography provides a superior prediction of the empirical functional connectivity matrix versus other tractography methods. Being the only input of the generalized Ising model, characteristics of the structural connectivity controls the state of the model. Therefore, finding the foremost method of tractography is important in modeling the dynamics using the structural connectivity. While previous researchers [3, 4, 2, 17, 18], established the capabilities of these different models in predicting the functional connectome of the brain (some of whom studied its dependence on the size of the structural connectome), they did not investigate how different methods of acquisition of the structural connectomes would affect their predictions. In contrast, our results decreased the ambiguity in using different tractography methods and proved that the deterministic tractography stands out by providing the best fit of the empirical correlation matrix over other methods in generalized Ising model simulations.

There are debates over choosing deterministic tractography versus probabilistic tractography to obtain the structural connectome of the brain [19, 20, 21] for different purposes. Recently, in [22], Kahlsa et al. demonstrated that probabilistic tractography is better able of identify cross-fiber connections than is deterministic tractography; while deterministic tractography is better able to identify long range anatomical connectivity. Despite the advantages

of probabilistic tractography in explaining cross-fiber connectivity, generalized Ising model performs best with the structural connectome containing only the most necessary information about the anatomical connectivity.

Generalized Potts model simulations further justified our choice of the generalized Ising model to predict the empirical functional connectome over a Potts model with a higher number of spin states. Even though an increase in the number of spin states produced a time series more similar to the BOLD time series, instead of a time series generated in a system with just two spin states, it did not significantly modify the correlations among the time series. Despite the generalization of the model using the structural connectome of the brain, similar to [23, 24], it was observed that when the number of spin states increased, the value of the critical temperature decreased. As discussed in Chapter 4, a significant correlation between direct neural activity of the brain regions and the time series generated for each region using the 2 state Potts model (Ising model) was hypothesized from the results. To test this further, it will be useful to convolute the simulated time series with a hemodynamic response function, and generate a signal, which can be compared with the empirical BOLD signals.

5.2 Future work

Two novel methodologies applied to significant areas of research in neuroscience were presented in this thesis that deserve further investigations as described below. The importance of these research areas, of the approach we have taken, and of this work's impact to the field of neuroscience are discussed. In addition to that, key limitations of proposed work is discussed. In future work, we focus to address some of the shortcomings that are common to presented work, one being modifying the computer simulations such that the model can be simulated on structural connectomes generated using different parcellation schemes (with more than 84 ROIs) without being time consuming. Currently, we are simulating the generalized Ising model using different sizes of structural connectomes for the same set of subjects to study the effect of

the size on the prediction. Another point that we would like to focus on is to find an appropriate scheme to modify the generalized Ising model implementation to account for the activity of astrocytes and neuronal populations separately via the structural connectivity, rather than using a common structural connectivity matrix which provides only the anatomical connections between neuronal populations. Additionally, mental test and comparisons between the frequency content of the simulated and empirical time series will be performed to compare the simulated correlation matrices with the empirical correlation matrix instead of the correlation coefficient which only consider the linear relationships between the matrices that are being compared.

5.2.1 Application of the generalized Ising model to patients with brain injuries

Following the three papers presented in this thesis, we have established the potential of a two-spin generalized Ising model, simulated on a structural connectome generated using deterministic tractography, to predict the empirical functional correlation matrix at the critical temperature. Subsequently, it is our intention to simulate the optimized generalized Ising model on a structural connectome belonging to patients with Disorders Of Consciousness (DOC). This will allow us to thoroughly investigate how the altered structural connectomes affect the functional connectomes of these patients. Further investigations will hopefully lead our research to predict changes in functional correlations upon hypothesizing further changes (such as introducing or removing more connections in the structural connectivity matrix) in the structural connectome, and assisting us in finding those necessary connections whose re-introduction could restore the functions of the patient's brain.

The challenges we face in conducting this work lie in the extraction of the structural connectome from DOC patients. Complex brain anatomy is further complicated by brain injury and, unlike the case of healthy patients, both the implementation of brain imaging for DOC patients and the tractography procedure necessary to obtain underlying structural architecture demand careful attention to detail. Furthermore, it would be more meaningful to apply a par-

cellation scheme different from AAL2, with a higher number of ROIs. As discussed in [25], the optimal number of ROIs a parcellation scheme may have—such that the separation of functionally specialized regions in the brain are as meaningful as possible—is 208.

5.2.2 Dimensionality calculation of any complex network

Another line of research which follows from Chapter 2 is the calculation of dimensionality of a system, given the characteristics of its underlying structural connectivity. Calculating the dimensionality of a system is important, as it is a key factor that drives the behavior of smaller units in a system leading to its overall performance [26, 11]. Understanding the dimensionality of a given system can provide new pathways to study complex networks.

Interestingly, there is an ample amount of not only man-made networks (such as the world wide web, social networks, or airline connection maps), but also natural networks, such as the neuronal networks. Even though the dimensionality of a network is most commonly defined by its physical dimensions, some networks do not admit a definition of dimensionality a priori, as they exist in a virtual space (rather than a physical one). Even if the system occupies a physical space, dimensionality of the system in physical space may not be the relevant quantity which controls the network behavior. Hence, our goal is to introduce the application of an approach of defining dimensionality accompanying the structural connectivity architecture, as well as the functions of sub units in the network, using the generalized Ising model such that the dimensionality can always be calculated: regardless of whether a system occupies a physical space or a virtual space. In networks where no viable concept of dimensionality previously exists, defining the dimensionality via the generalized Ising model will improve the understanding of the functionality of a particular network while also providing the ability to predict the functions resulting from changes in the structural architecture.

Bibliography

[1] Daniel Fraiman, Pablo Balenzuela, Jennifer Foss, and Dante R Chialvo. Ising-like dynamics in large-scale functional brain networks. *Physical Review E*, 79(6):061922, 2009.

[2] Sebastiano Stramaglia, Mario Pellicoro, Leonardo Angelini, Enrico Amico, Hannelore Aerts, JM Cortés, Steven Laureys, and Daniele Marinazzo. Ising model with conserved magnetization on the human connectome: Implications on the relation structure-function in wakefulness and anesthesia. *Chaos: An Interdisciplinary Journal of Nonlinear Science*, 27(4):047407, 2017.

[3] Gustavo Deco, Mario Senden, and Viktor Jirsa. How anatomy shapes dynamics: a semi-analytical study of the brain at rest by a simple spin model. *Frontiers in computational neuroscience*, 6:68, 2012.

[4] Daniele Marinazzo, Mario Pellicoro, Guo-Rong Wu, Leonardo Angelini, Jesus M Cortes, and Sebastiano Stramaglia. Information transfer of an ising model on a brain network. *BMC neuroscience*, 14(1):P376, 2013.

[5] Pubuditha M Abeyasinghe, Demetrius Ribeiro de Paula, Sina Khajehabdollahi, Sree Ram Valluri, Adrian M Owen, and Andrea Soddu. Role of dimensionality in predicting the spontaneous behavior of the brain using the classical ising model and the ising model implemented on a structural connectome. *Brain connectivity*, 8(7):444–455, 2018.

[6] Dante R Chialvo. Critical brain networks. *Physica A: Statistical Mechanics and its Applications*, 340(4):756–765, 2004.

[7] Mikail Rubinov, Olaf Sporns, Jean-Philippe Thivierge, and Michael Breakspear. Neurobiologically realistic determinants of self-organized criticality in networks of spiking neurons. *PLoS computational biology*, 7(6):e1002038, 2011.

[8] Enzo Tagliazucchi and Dante R Chialvo. The collective brain is critical. *arXiv preprint arXiv:1103.2070*, 2011.

[9] Luca Cocchi, Leonardo L Gollo, Andrew Zalesky, and Michael Breakspear. Criticality in the brain: A synthesis of neurobiology, models and cognition. *Progress in neurobiology*, 158:132–152, 2017.

[10] David P Landau and Kurt Binder. *A guide to Monte Carlo simulations in statistical physics*. Cambridge university press, 2014.

[11] Francesco Paolo Ulloa Severino, Jelena Ban, Qin Song, Mingliang Tang, Ginestra Bianconi, Guosheng Cheng, and Vincent Torre. The role of dimensionality in neuronal network dynamics. *Scientific reports*, 6:29640, 2016.

[12] Kechen Zhang and Terrence J Sejnowski. Neuronal tuning: To sharpen or broaden? *Neural computation*, 11(1):75–84, 1999.

[13] Stefano Fusi, Earl K Miller, and Mattia Rigotti. Why neurons mix: high dimensionality for higher cognition. *Current opinion in neurobiology*, 37:66–74, 2016.

[14] Lindsay I Smith. A tutorial on principal components analysis. Technical report, 2002.

[15] Konstantinos I Diamantaras and Sun Yuan Kung. *Principal component neural networks: theory and applications*, volume 5. Wiley New York, 1996.

[16] Rich Pang, Benjamin J Lansdell, and Adrienne L Fairhall. Dimensionality reduction in neuroscience. *Current Biology*, 26(14):R656–R660, 2016.

[17] Ruben Schmidt, Karl JR LaFleur, Marcel A de Reus, Leonard H van den Berg, and Martijn P van den Heuvel. Kuramoto model simulation of neural hubs and dynamic synchrony in the human cerebral connectome. *BMC neuroscience*, 16(1):54, 2015.

[18] CJ Honey, O Sporns, Leila Cammoun, Xavier Gigandet, Jean-Philippe Thiran, Reto Meuli, and Patric Hagmann. Predicting human resting-state functional connectivity from structural connectivity. *Proceedings of the National Academy of Sciences*, 106(6):2035–2040, 2009.

[19] Kei Yamada, Koji Sakai, Kentaro Akazawa, Sachiko Yuen, and Tsunehiko Nishimura. Mr tractography: a review of its clinical applications. *Magnetic resonance in medical sciences*, 8(4):165–174, 2009.

[20] Maxime Descoteaux, Rachid Deriche, Thomas R Knosche, and Alfred Anwander. Deterministic and probabilistic tractography based on complex fibre orientation distributions. *IEEE transactions on medical imaging*, 28(2):269–286, 2009.

[21] Zhixi Li, Kyung K Peck, Nicole P Brennan, Mehrnaz Jenabi, Meier Hsu, Zhigang Zhang, Andrei I Holodny, and Robert J Young. Diffusion tensor tractography of the arcuate fasciculus in patients with brain tumors: comparison between deterministic and probabilistic models. *Journal of biomedical science and engineering*, 6(2):192, 2013.

[22] Sakh Khalsa, Stephen D Mayhew, Magdalena Chechlacz, Manny Bagary, and Andrew P Bagshaw. The structural and functional connectivity of the posterior cingulate cortex: Comparison between deterministic and probabilistic tractography for the investigation of structure–function relationships. *Neuroimage*, 102:118–127, 2014.

[23] PRO Da Silva, FWS Lima, and RN Costa Filho. Potts model with q= 3 and 4 states on directed small-world network. *Computer Physics Communications*, 184(12):2746–2750, 2013.

[24] RM Marques, FWS Lima, and Raimundo N Costa Filho. Potts model on directed small-world voronoi–delaunay lattices. *Physica A: Statistical Mechanics and its Applications*, 451:295–304, 2016.

[25] Erik SB van Oort, Maarten Mennes, Tobias Navarro Schröder, Vinod J Kumar, Nestor I Zaragoza Jimenez, Wolfgang Grodd, Christian F Doeller, and Christian F Beckmann. Functional parcellation using time courses of instantaneous connectivity. *NeuroImage*, 170:31–40, 2018.

[26] H Eugene Stanley. Dependence of critical properties on dimensionality of spins. *Physical Review Letters*, 20(12):589, 1968.

Appendix A

Appendices: Chapter 2

A.1 2D Classical Ising model

The classical Ising model was introduced by Wilhelm Lenz in 1920. The 2D Ising model (in the absence of an external magnetic field) was solved by Onsager in 1944 [1]. It was introduced to explain the interactions of magnetic spins mathematically. The physical system (a magnet) is represented by a lattice configuration in the Ising model. Each lattice site has a spin s which could take only two possible values, either up (+1) or down (−1) (Figure A.1). Thus, it is a collection of +1 and −1s representing the spins. This configuration is kept in a thermal bath of temperature T. Interactions between the spins are always influenced by this temperature and allow the system to reach an equilibrium energy state while resulting in different equilibrium spin configurations with different properties at different temperatures.

The energy of this spin system at any state x in the absence of an external magnetic field can be calculated using Equation A.1:

$$E(x) = -J \sum_{i,j=nn(i)}^{N} s_i s_j \tag{A.1}$$

where J is the coupling constant, s_i and s_j represent the spins of the i^{th} and j^{th} site respectively, and N is the size of the lattice. For the calculation of energy in the 2D Ising model, only

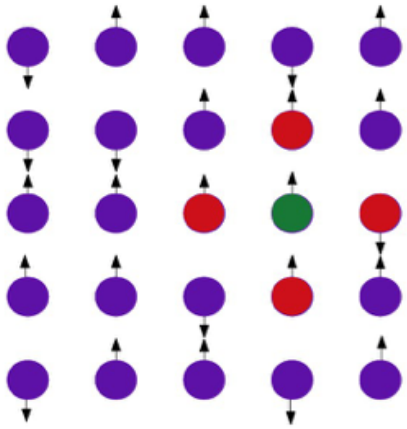

Figure A.1: Representation of a 2D lattice arrangement. Each lattice site has a spin, either up or down. The nearest neighbours of the green lattice site are represented in red

the nearest neighbour interactions are considered together with equal coupling (J = 1). The probability of finding the system in the state x with energy $E(x)$ is given by Equation A.2:

$$P(x) = \frac{1}{Z}\ e^{-\frac{E(x)}{k_B T}} \tag{A.2}$$

where k_B is the Boltzmann constant, T is the temperature of the heat bath and Z is the partition function. Equation A.3 illustrates the partition function of the system which describes the statistical properties of the spin system in thermodynamic equilibrium. The summation is over all possible 2^N spin configurations.

$$Z = \sum_{\{x\}} e^{-\frac{E(x)}{k_B T}} \tag{A.3}$$

At equilibrium, thermodynamic properties such as magnetization, magnetic susceptibility and the specific heat of the system can be calculated using Equations A.4, A.5 and A.6 respectively where s_i is the spin of the i^th spin site. Magnetization simply is an order parameter which explains the state of the spin system, either an ordered state or a disordered state. Magnetic susceptibility is the derivative of magnetization which captures the changes of magnetization.

This is used to identify the critical temperature of the spin system by noting the temperature which maximizes the susceptibility (or the temperature which gives the highest variation of magnetization). Specific heat tells us how much does the energy of the spin system changes with changing temperature.

$$M = \frac{1}{N} \mid \sum_{i=1}^{N} s_i \mid \tag{A.4}$$

$$\chi = \frac{1}{T}[\langle M^2 \rangle - \langle M \rangle^2] \tag{A.5}$$

$$C_v = \frac{1}{T^2}[\langle E^2 \rangle - \langle E \rangle^2] \tag{A.6}$$

When a 2D lattice configuration is considered, there are two extreme equilibrium configurations of spins it can hold, one for lower temperatures (sub-critical) and the other one for higher temperatures (super-critical). When the temperature is very low, all the spins prefer to be aligned along the same direction, with very large clusters of the same spin, either up or down (ordered) resulting in high magnetization even in the absence of an external magnetic field (Figure A.2 (a)). In the other end, when the temperature is very high, the spins are a mixture of up spins as well as down spins (disordered) without any order which will result in zero magnetization (Figure A.2 (c)). In between these two extremes, there exists a critical temperature (T_c) [3] where the system exhibits transition from ordered phase to the disordered phase (Figure A.2 (b)). As the figure illustrates, at this temperature there is a mixture of ordered spins as well as disordered spins. Additionally, the system acquires its maximum susceptibility or the maximum change in magnetization at T_c. Even a single spin flip can change the entire system [2], and the perturbation introduced by a single spin flip can spread over the entire system rapidly. Therefore, with different temperatures of the heat bath, the system could exhibit completely different properties [1] which depend only on the temperature of the system.

To impose the dynamics to the classical Ising model, the Metropolis Monte Carlo algorithm

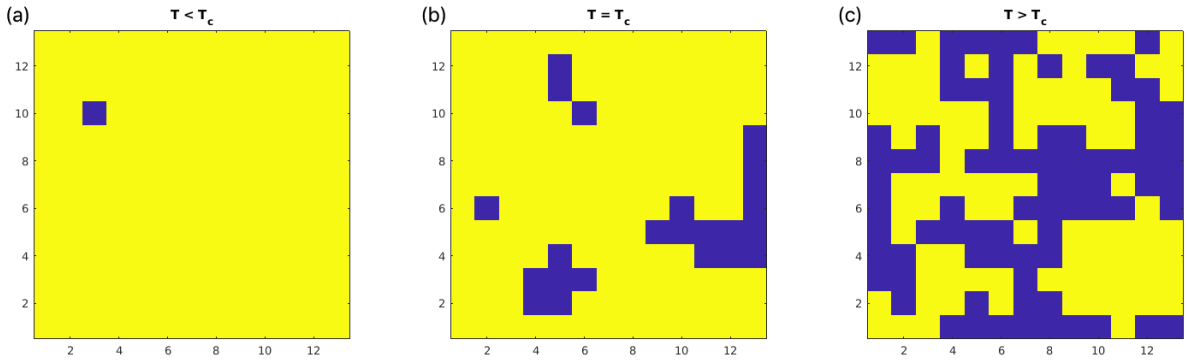

Figure A.2: Representation of the equilibrium spin configuration for (a) $T < T_c$, (b) $T = T_c$ and (c) $T > T_c$ for a two-dimensional lattice arrangement. Red color is for the up spins (+1) and blue color is for the down spins (−1) [3]

is used. The Metropolis algorithm involves the construction of a new state based on the current state of the system with a transition probability. It is used in the Ising model to find the equilibrium energy state starting from a random spin configuration for a constant temperature [4]. This algorithm is used in the classical Ising model with the periodic boundary conditions. Periodic boundary conditions were introduced to the system to restrain the finite size effects.

In the simplest way, spins of the Ising model can be considered as equivalent to the BOLD activity in the brain with +1 for the activity higher than the baseline activity and −1 for the activity lower than the baseline activity. The classical Ising model exhibits long range correlations at the critical temperature, which explains the observed interactions of the spins that are spatially distant from each other. This fact can be compared with the functional integration observed in the brain. The brain maintains a balance between the functional integration and segregation in order to perform efficiently [5]. As observed in the behaviour of the brain, there are separate regions which are specialized to perform certain functions. While functioning separately, these regions need to exchange information with each other in order to function as a complete system. This process is explained as the functional integration and can be compared with the long range correlations observed in the Ising model. Thus the classical Ising model was chosen to model the oscillations observed in BOLD signal for comparison.

A.2 Critical exponents and scaling relations

Critical exponents

Critical exponents of Magnetization, Susceptibility and Specific Heat was calculated by fitting Equation A.7 to A.11 for the respective plots. For Susceptibility and the Specific Heat, since there are two separate equations for fitting the right hand side and the left hand side of the plot, we obtained two critical exponents using both equations. Then the exponent that has the minimum error was chosen.

Magnetization

$$M(T) = P_1[\frac{T_c - T}{T_c}]^{\beta} \tag{A.7}$$

Susceptibility

$$\chi_{left}(T) = P_1[\frac{T_c - T}{T_c}]^{-\gamma} \tag{A.8}$$

$$\chi_{right}(T) = P_1[\frac{T - T_c}{T_c}]^{-\gamma} \tag{A.9}$$

Specific Heat

$$c_{v-left}(T) = P_1[-\ln(\frac{T_c - T}{T_c})]^{\alpha} \tag{A.10}$$

$$c_{v-right}(T) = P_1[-\ln(\frac{T - T_c}{T_c})]^{\alpha} \tag{A.11}$$

Correlation function

In order to calculate the correlation length (η) for different temperatures, Equation A.12 was fitted for the correlation function versus distance plot at each temperature. At the critical temperature, the correlation length goes to infinity and Equation A.12 simplifies to Equation A.13. Furthermore, the correlation function at the critical temperature is said to behave according to Equation A.14 at the critical temperature [6]. Therefore the critical exponent for the correlation function (ν) was obtained by fitting Equation A.14 for the correlation function versus temperature plot at the critical temperature. By plugging in this value in the denominator of Equation A.13, we were able to calculate the dimensionality.

$$G(r) = \frac{exp(\frac{-r}{\xi})}{r^{d-2+\eta}} \tag{A.12}$$

$$G(r)[atT_c] = \frac{1}{r^{d-2+\eta}} \tag{A.13}$$

$$G(r)[atT_c] = P_1(r)^{-\eta} \tag{A.14}$$

Correlation length

Correlation lengths which have been calculated by fitting Equation A.12 was plotted as a function of temperature. Equation A.15 and A.16 was used to fit the above mentioned plot from left hand side and the right hand side and ν, the critical exponent of the correlation length was obtained.

$$\xi_{left}(T) = P_1[\frac{T_c - T}{T_c}]^{-\nu} \tag{A.15}$$

$$\xi_{right}(T) = P_1[\frac{T - T_c}{T_c}]^{-\nu} \tag{A.16}$$

Scaling relations

Critical exponents calculated from the above mentioned methods obey the scaling relations presented in Equations A.17, A.18 and A.19.

$$(2 - \eta)\nu = \gamma \tag{A.17}$$

$$\frac{\nu}{2}(\eta + d - 2) = \beta \tag{A.18}$$

$$2 - \nu d = \alpha \tag{A.19}$$

Variables and constants in the equations:

P_1 - Constant

T - Temperature

T_c - Critical Temperature

η - Correlation Length

r - Distance

d - Dimensionality

Critical exponents

β - Magnetization

γ - Susceptibility

α - Specific Heat

η - Correlation Function

ν - Correlation Length

A.3 Labels of 84 parcellations of the brain

Right hemishpere

1. Thalamus-Proper
2. Caudate
3. Putamen
4. Pallidum
5. Hippocampus
6. Amygdala
7. Accumbens-area
8. bankssts
9. caudalanteriorcingulate
10. caudalmiddlefrontal
11. cuneus
12. entorhinal
13. fusiform
14. inferiorparietal
15. inferiortemporal
16. isthmuscingulate
17. lateraloccipital
18. lateralorbitofrontal
19. lingual
20. medialorbitofrontal
21. middletemporal
22. parahippocampal
23. paracentral
24. parsopercularis
25. parsorbitalis
26. parstriangularis
27. pericalcarine
28. postcentral
29. posteriorcingulate
30. precentral
31. precuneus
32. rostralanteriorcingulate
33. rostralmiddlefrontal
34. superiorfrontal
35. superiorparietal
36. superiortemporal
37. supramarginal
38. frontalpole
39. temporalpole
40. transversetemporal
41. insula
42. Cerebellum-Cortex

Left hemishpere

43. bankssts
44. caudalanteriorcingulate
45. caudalmiddlefrontal
46. cuneus
47. entorhinal
48. fusiform
49. inferiorparietal
50. inferiortemporal
51. isthmuscingulate
52. lateraloccipital
53. lateralorbitofrontal
54. lingual
55. medialorbitofrontal
56. middletemporal
57. parahippocampal
58. paracentral
59. parsopercularis
60. parsorbitalis
61. parstriangularis
62. pericalcarine
63. postcentral
64. posteriorcingulate
65. precentral
66. precuneus
67. rostralanteriorcingulate
68. rostralmiddlefrontal
69. superiorfrontal
70. superiorparietal
71. superiortemporal
72. supramarginal
73. frontalpole
74. temporalpole
75. transversetemporal
76. insula
77. Cerebellum-Cortex
78. Thalamus-Proper
79. Caudate
80. Putamen
81. Pallidum
82. Hippocampus
83. Amygdala
84. Accumbens-area

A.4 Supplementary figures

A.4.1 Distance between the correlation dictributions

To compare the correlation distributions, the distance between the correlation distributions were calculated using the Kolmogrov Smirnov test [7]. The temperature (T_{min}) which minimizes this distance was obtained for the ten realizations separately and compared with T_c using a two sample t-test.

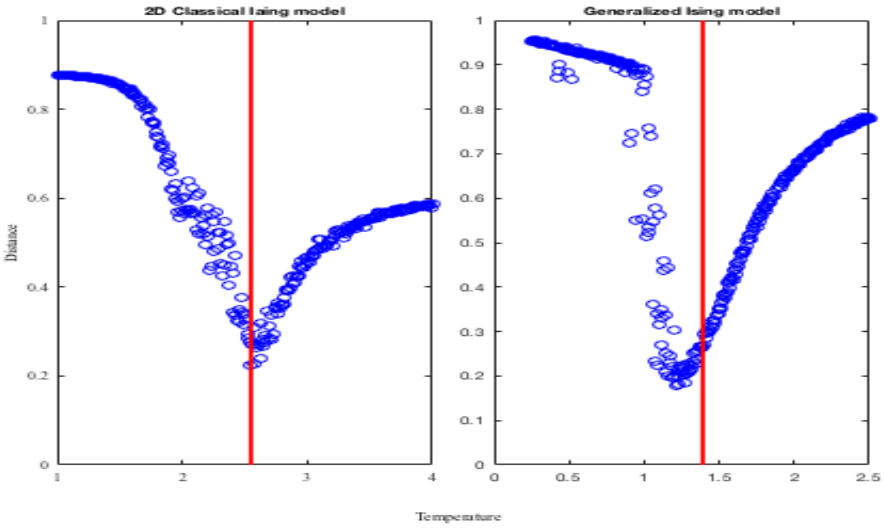

Figure A.3: Distance between the correlation distributions as a function of temperature for the 2D classical Ising model and the generalized Ising mode. Red vertical line corresponds to the critical temperature T_c

A.4.2 Inter-subject variance of T_c and T_{min}

The work presented in the paper was performed using the average connectivity over 69 subjects. Variation of the critical temperature and T_{min} was due to simulating the 2D classical Iasing model and the generalized Ising model ten times using the same average connectivity. However, we simulated the generalized Ising model using 69 different structural connectivity matrices and the figure below illustraites how T_c and T_{min} are distributed among the subjects.

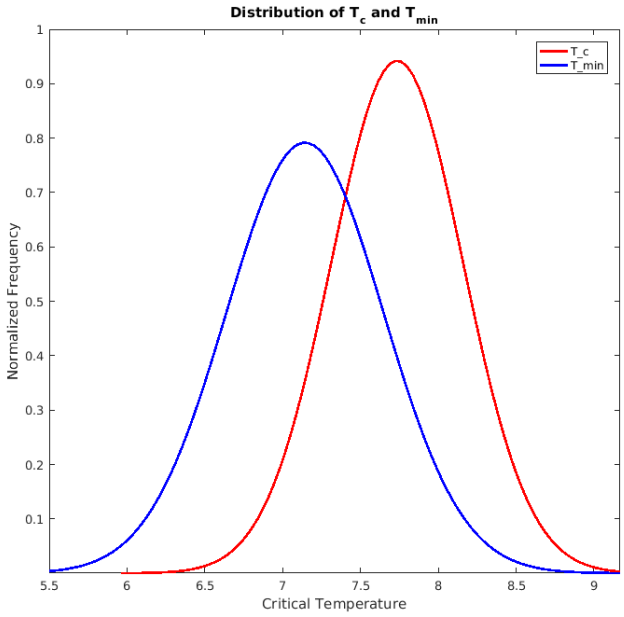

Figure A.4: Distribution of T_c and T_{min} for 69 subjects

A.4.3 Further study of the difference in T_c

In order to investigate the observed difference of T_c for the generalized Ising model and the 2D classical Ising model we generated different connectivity matrices by gradually changing the sparsity of the matrices. Figure A.5 represents the initial structrual connectivity which is been used for the generalized Ising model simulations and then how an intermediate structural connectivity as well as the structural connectivity of the 2D classical Ising model.

Starting with the structural connectivity used in the generalized Ising model simulations and by changing/removing connections randomly preserving the randomness, the structural connectivity was gradually transformed to that of the 2D Ising model.The connectivity matrices build during this transformation were used in the generalized Ising model simulations and the critical temperature was obtained from each simulation. In Figure A.6, critical temperature is plotted as a function of the sparsity of the connectivity matrix. Transition is from the generalized Ising model with a sparsity of 0.06 to the 2D classical Ising model with a sparsity of 0.95. From this figure it can be seen that the sparsity of the connectivity matrix could explain

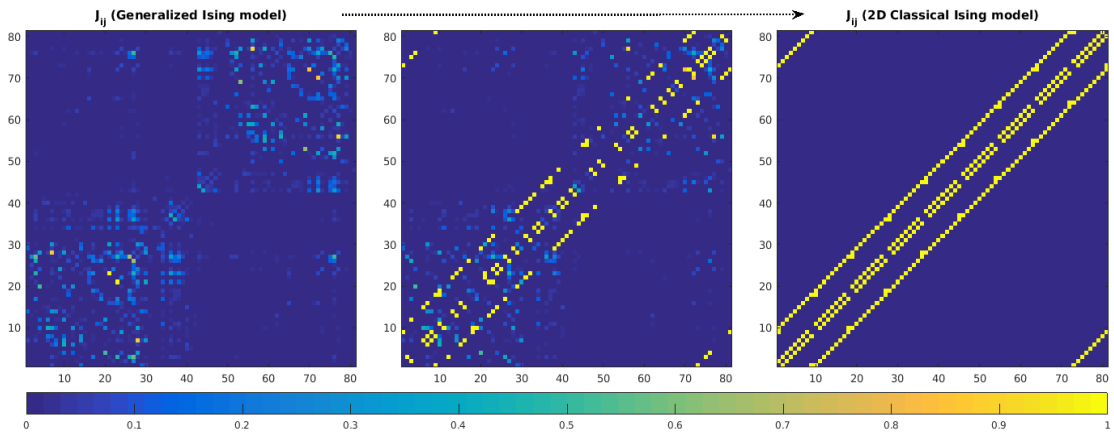

Figure A.5: Structural connectivity matrix of the generalized Ising model, an intermediate structural connectivity and the structural connectivity used for the 2D classical Ising model

the difference observed in the critical temperatures from the generalized Ising model and the 2D classical Ising model. However, the variations observed in the critical temperature in this figure could be due to the random procedure followed in order to get different connectivity matrices during the transition.

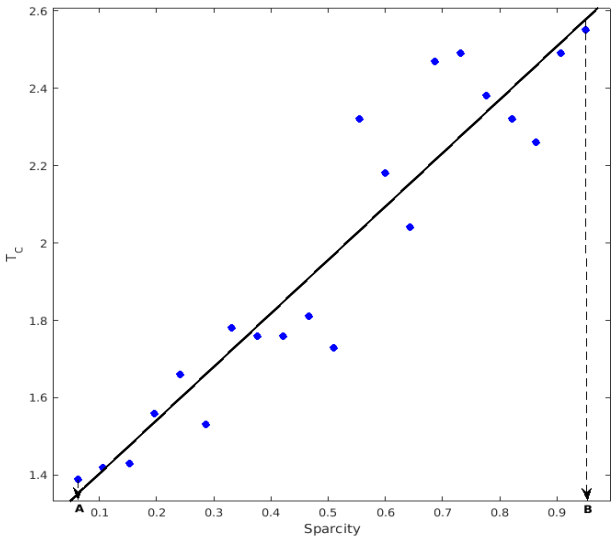

Figure A.6: Critical temperature versus sparsity of the connectivity matrices. Point A represents the sparsity of the generalized Ising model and point B the 2D classical Ising model

A.4.4 Global degree as a function of temperature

In graph theory, degree of a node is said to be the number of connection that node has. For a graph, the global degree gives the average degree of the whole network by taking the average over the number of nodes the network has. We have calculated the global degree for using the results of the simulations of 2D classical Ising model and the generalized Ising model as a function of temperature. From this plot, it is evident that the degree of the generalized Ising model maximizes at a temperature different from the critical temperature but not significantly different from T_{min}.

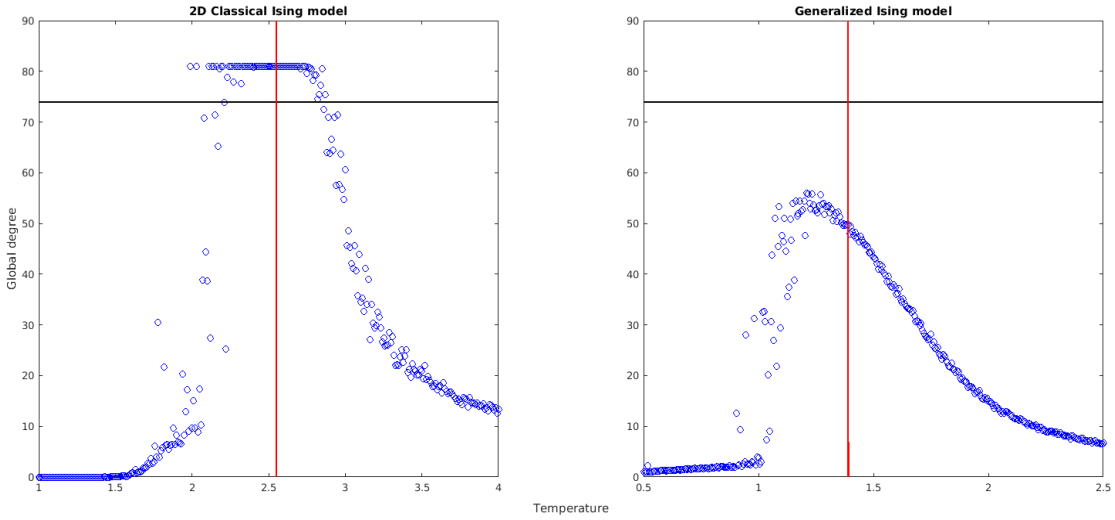

Figure A.7: Global degree as a function of temperature for the 2D classical Ising model and the Generalized Ising model. Black horizontal line represents the global degree for the empirical functional connectivity. Red vertical line represents the critical temperature for each case

Bibliography

[1] Stephen G Brush. History of the Lenz-Ising model. *Reviews of modern physics*, 39(4):883, 1967.

[2] Dante R Chialvo. Emergent complex neural dynamics. *Nature physics*, 6(10):744–750, 2010.

[3] TK Das, PM Abeyasinghe, JS Crone, A Sosnowski, S Laureys, AM Owen, and A Soddu. Highlighting the structure-function relationship of the brain with the Ising model and graph theory. *BioMed research international*, 2014.

[4] David P Landau and Kurt Binder. *A guide to Monte Carlo simulations in statistical physics*. Cambridge University Press, 2014.

[5] Giulio Tononi, Gerald M Edelman, and Olaf Sporns. Complexity and coherency: integrating information in the brain. *Trends in cognitive sciences*, 2(12):474–484, 1998.

[6] Lilian Witthauer and Manuel Dieterle. The phase transition of the 2d-ising model. *Summer Term*, 7(1):1–5, 2007.

[7] Ian T Young. Proof without prejudice: use of the kolmogorov-smirnov test for the analysis of histograms from flow systems and other sources. *Journal of Histochemistry & Cytochemistry*, 25(7):935–941, 1977.

Appendix B

Appendices: Chapter 3

B.1 Calculating the Dimensionality of a System Using the Results of Generalized Ising Model Simulations

Normalized structural connectivity (J_{ij}) of the system is used in the generalized Ising model simulations which results in the time series for each node of the network for a given number of time points. Pearsons' correlation between these time series was calculated which results in a N$\times$ N symmetric correlation matrix (where N is the number of nodes in the network or the number of sites). This process was carried out for a range of temperatures.

Calculting the correlation function $G(r)$

Correlation function per temperature illustrates the changes of correlation with respect to the distance between the nodes. In order to calculate the correlation function, firstly, the distance between nodes were defined using the structural connectivity matrix as $\frac{1}{J_{ij}}$. Secondly, the correlation was grouped such that the correlation at a particular distance is the average of all correlations at that distance. It resulted a correlation as a function of distance for each temperature.

Correlation function can be explained using Equation B.1 for any temperature [2, 1] except the critical temperature. Equation B.1 simplifies to Equation B.2 at the critical temperature since the correlation length (ξ) becomes infinite at T_c.

$$G(r) \simeq \frac{exp(\frac{-r}{\xi})}{r^{d-2+\eta}} = \frac{exp(\frac{-r}{\xi})}{r^{P_0}} \tag{B.1}$$

$$G(r) \simeq \frac{1}{r^{P_0}} \tag{B.2}$$

Calculating the dimensionality

From Ornstein-Zernike theory, another equation was developed to explain the correlation function at temperatures greater than the critical temperature, It is presented in Equation B.3 [1, 2].

$$G(r) \simeq \frac{exp(\frac{-r}{\xi})}{r^{\frac{d-1}{2}}} \tag{B.3}$$

By equating the power of r in the denominator of Equation refgrall and **??**,

$$P_0(T > T_c) = \frac{d-1}{2} \tag{B.4}$$

$$\therefore d = 2P_0 + 1 \tag{B.5}$$

Procedure: After calculating $G(r)$ for all the temperatures, Equation B.1 was fitted and P_0 and ξ per temperature were obtained from the fitting. Then P_0 values for $T > T_c$ were separated and averaged to obtain one P_0 value. Finally, using the calculated P_0 value and Equation B.5, dimensionality of the system was calculated.

B.2 Additional Results of the Initial Analysis of Tractography

In all the figures below, panel (a) represents the networks obtained using simulated functional data while panel (b) represents the networks obtained from empirical functional data.

1. Deterministic tractography - FA

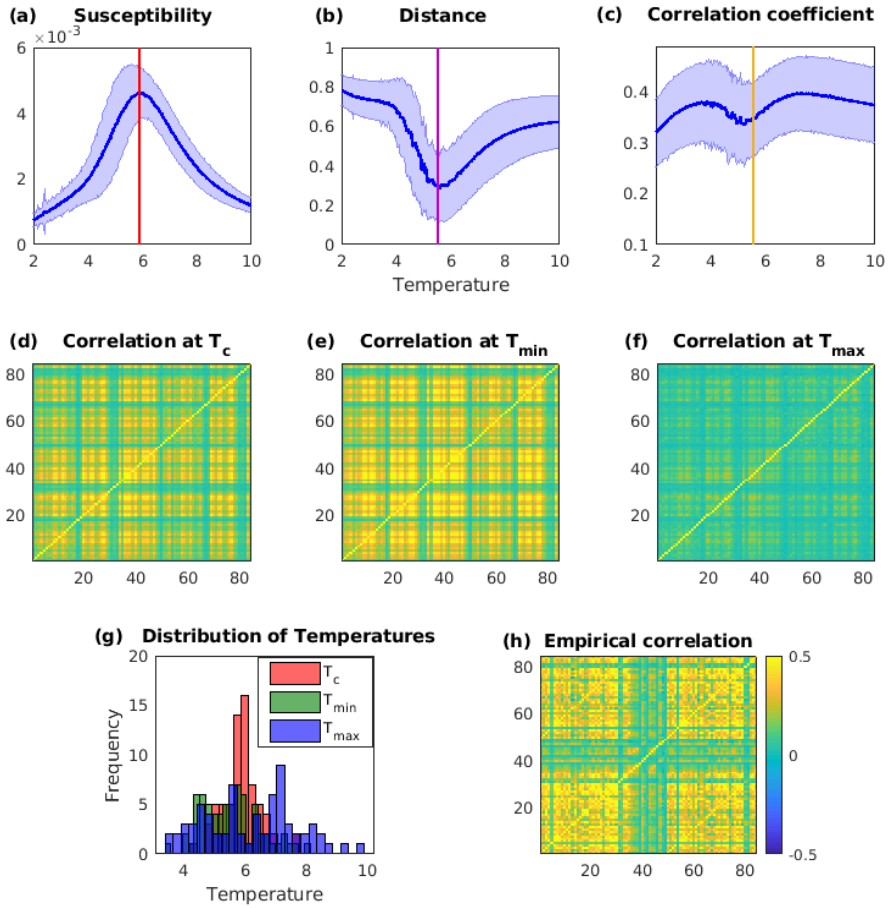

Figure B.1: (a) Average susceptibility as a function of temperature, (b) Distance between the simulated correlations and the empirical correlation as a function of temperature, (c) Correlation coefficient between the simulated correlations and the empirical correlations as a function of temperature, (d) (e) (f) (h) matrix representations of the correlation at T_c, T_{min} and T_{max} and empirical correlation respectively, (g) distribution of T_c, T_{min} and T_{max} within the group of 69 subjects

2. Deterministic tractography - counts weighted by FA

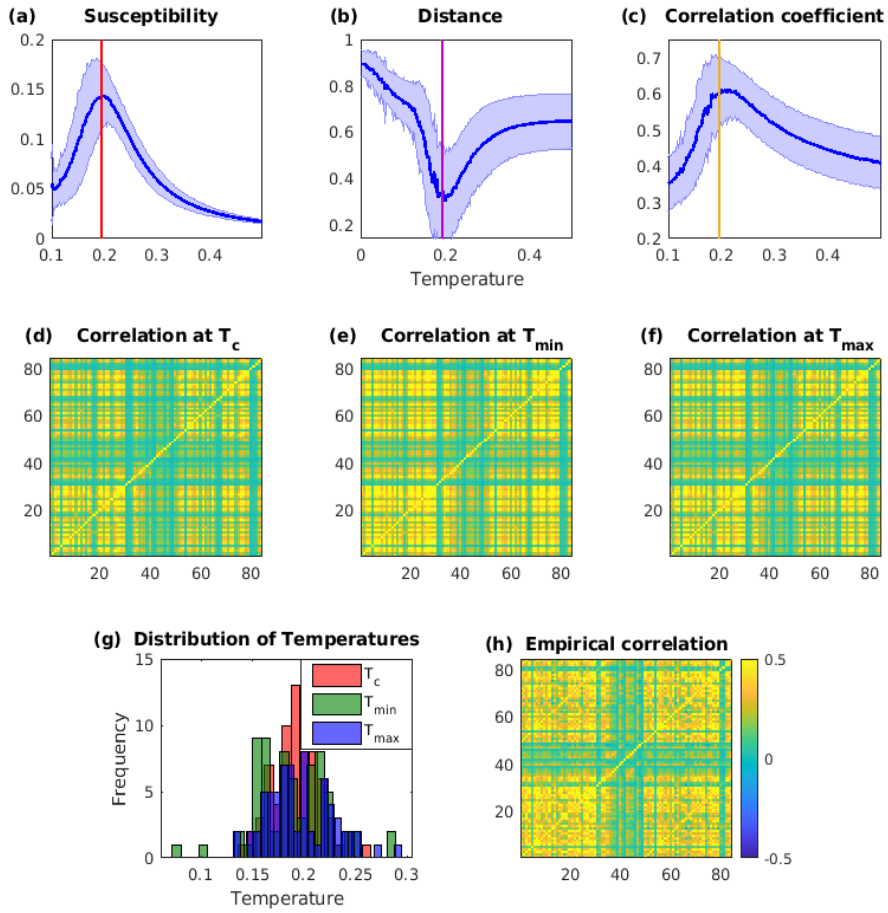

Figure B.2: (a) Average susceptibility as a function of temperature, (b) Distance between the simulated correlations and the empirical correlation as a function of temperature, (c) Correlation coefficient between the simulated correlations and the empirical correlations as a function of temperature, (d) (e) (f) (h) matrix representations of the correlation at T_c, T_{min} and T_{max} and empirical correlation respectively, (g) distribution of T_c, T_{min} and T_{max} within the group of 69 subjects

3. Probabilistic tractography - counts

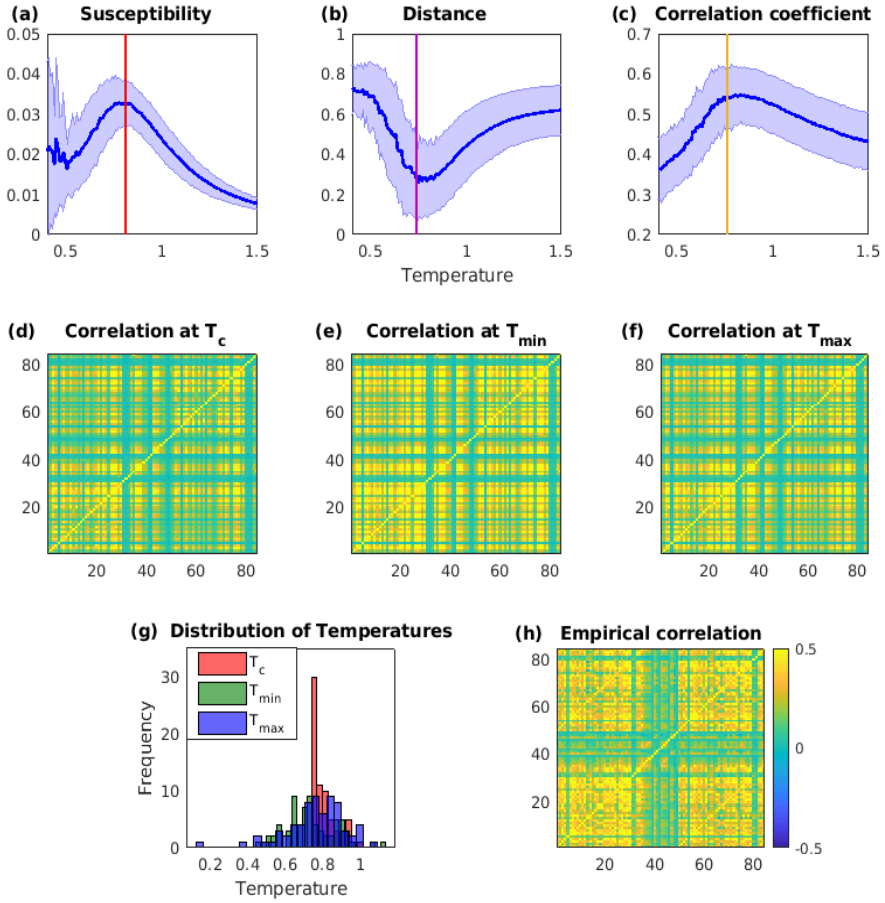

Figure B.3: (a) Average susceptibility as a function of temperature, (b) Distance between the simulated correlations and the empirical correlation as a function of temperature, (c) Correlation coefficient between the simulated correlations and the empirical correlations as a function of temperature, (d) (e) (f) (h) matrix representations of the correlation at T_c, T_{min} and T_{max} and empirical correlation respectively, (g) distribution of T_c, T_{min} and T_{max} within the group of 69 subjects

4. Probabilistic tractography - FA

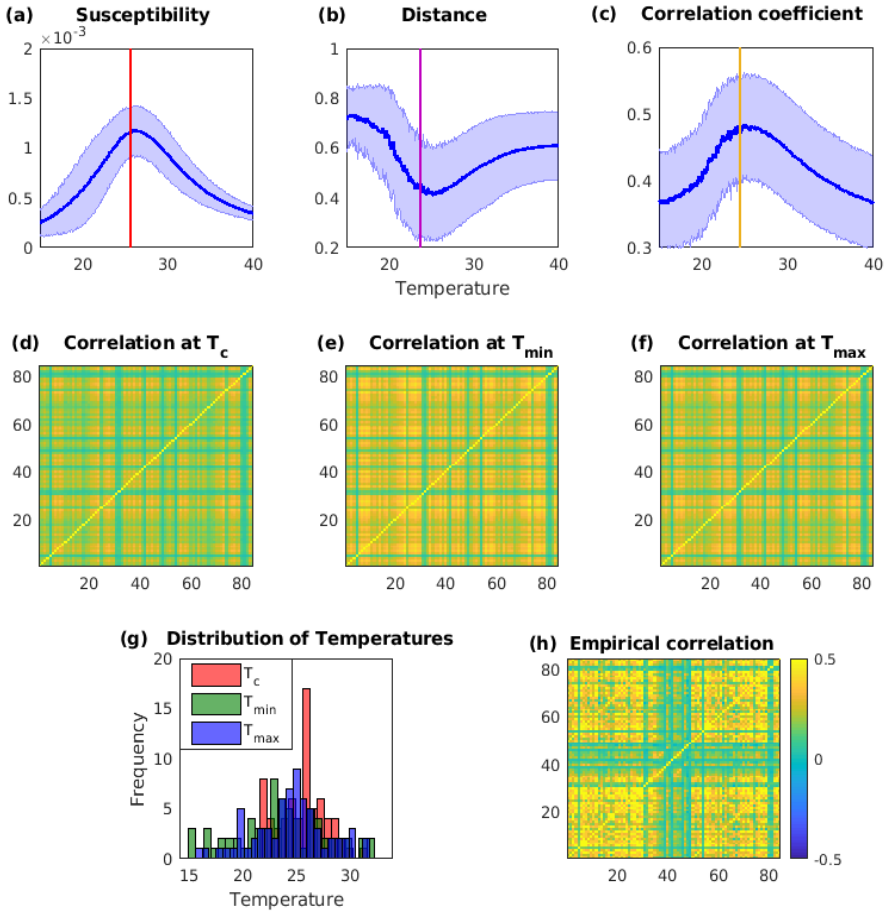

Figure B.4: (a) Average susceptibility as a function of temperature, (b) Distance between the simulated correlations and the empirical correlation as a function of temperature, (c) Correlation coefficient between the simulated correlations and the empirical correlations as a function of temperature, (d) (e) (f) (h) matrix representations of the correlation at T_c, T_{min} and T_{max} and empirical correlation respectively, (g) distribution of T_c, T_{min} and T_{max} within the group of 69 subjects

5. Probabilistic tractography - counts weighted by FA

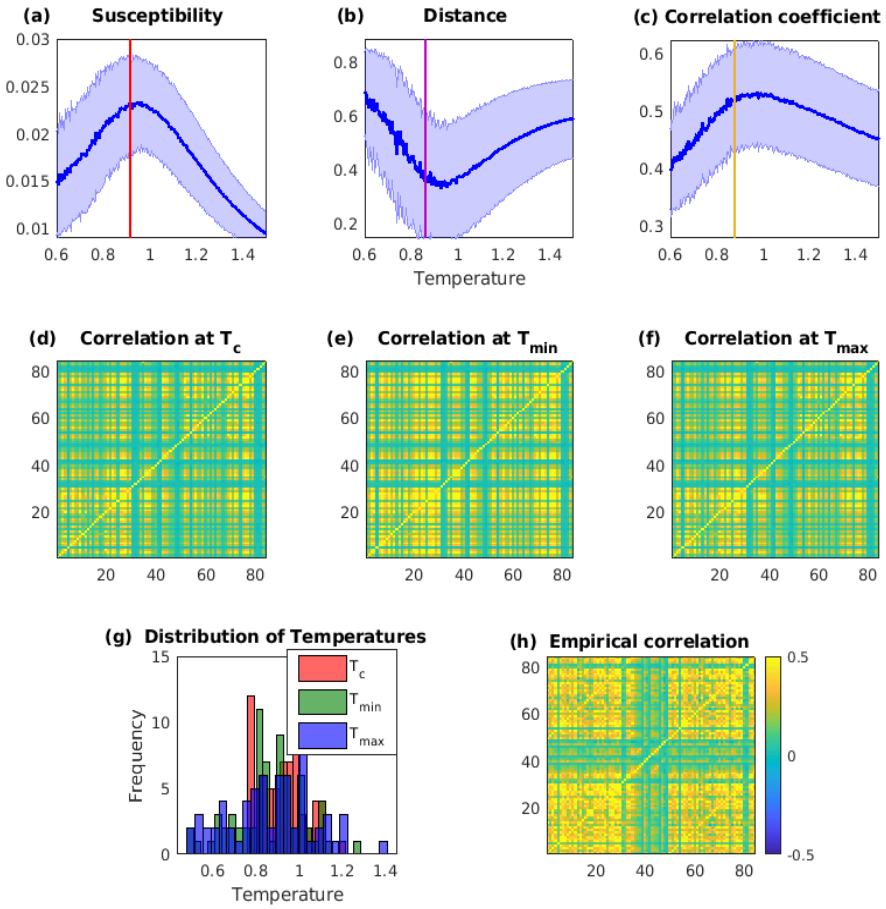

Figure B.5: (a) Average susceptibility as a function of temperature, (b) Distance between the simulated correlations and the empirical correlation as a function of temperature, (c) Correlation coefficient between the simulated correlations and the empirical correlations as a function of temperature, (d) (e) (f) (h) matrix representations of the correlation at T_c, T_{min} and T_{max} and empirical correlation respectively, (g) distribution of T_c, T_{min} and T_{max} within the group of 69 subjects

B.3 Additional Results of the RSN analysis

In all the figures below, panel (a) represents the networks obtained using simulated functional data while panel (b) represents the networks obtained from empirical functional data.

1. Deterministic tractography - FA

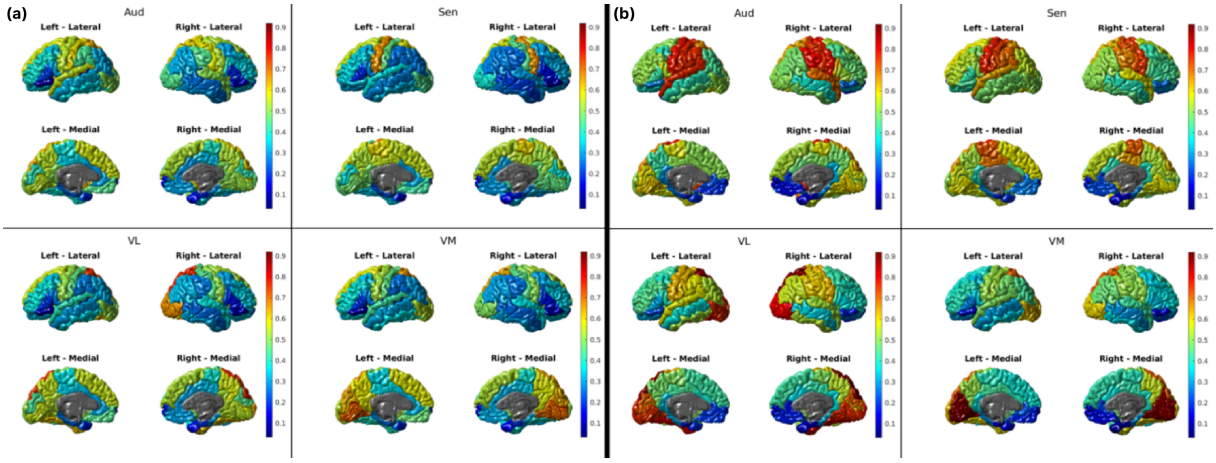

Figure B.6: Auditory network (Aud), Sensorimotor network (Sen), Visual lateral, medial networks (VL, VM) obtained from the simulated (at T_c) and the empirical correlations. RSNs for other tractography methods are presented in Appendix C

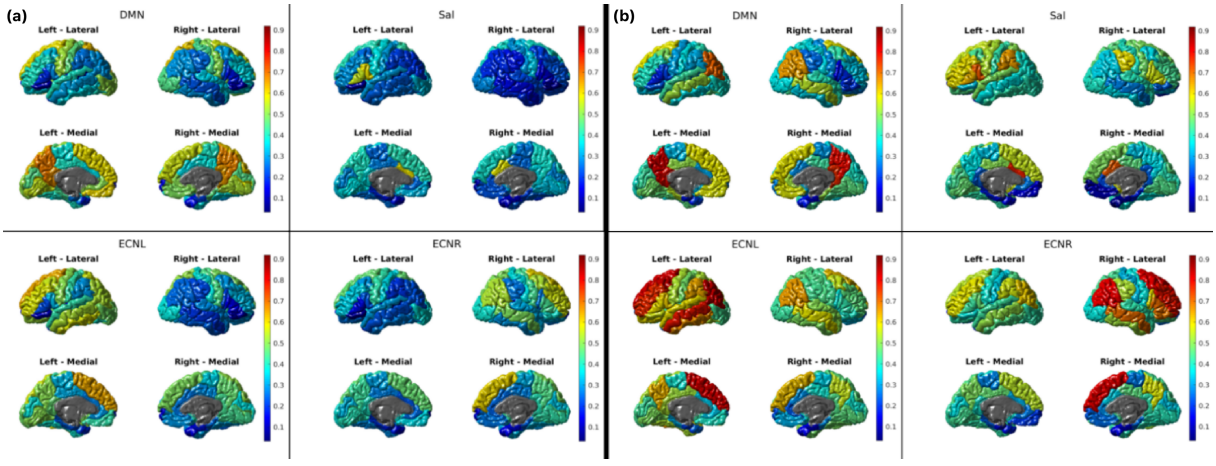

Figure B.7: Default mode network (DMN), Salience network (Sal), External control network left and right (ECNL, ECNR)

2. Deterministic tractography - counts weighted by FA

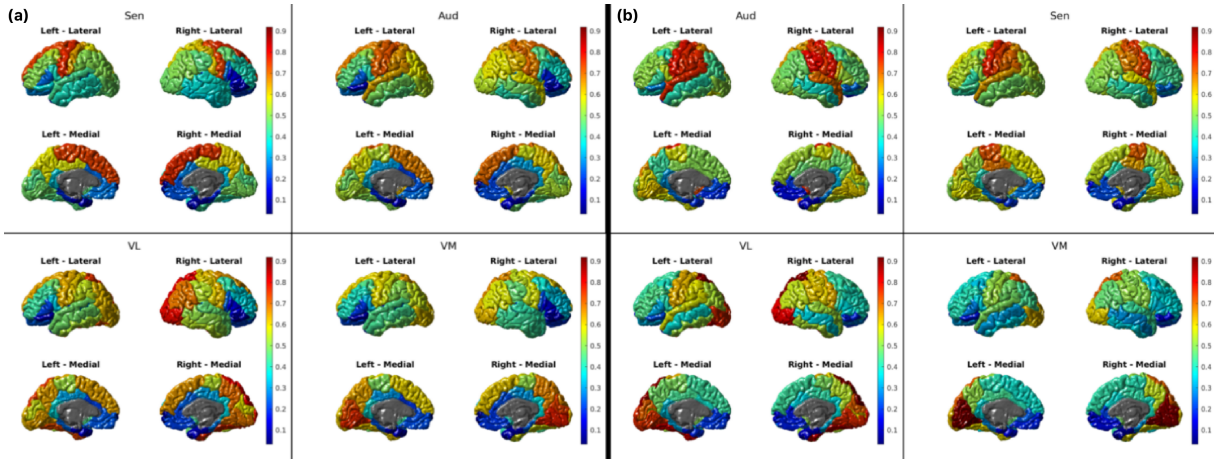

Figure B.8: Auditory network (Aud), Sensorimotor network (Sen), Visual lateral, medial networks (VL, VM) obtained from the simulated (at T_c) and the empirical correlations. RSNs for other tractography methods are presented in Appendix C

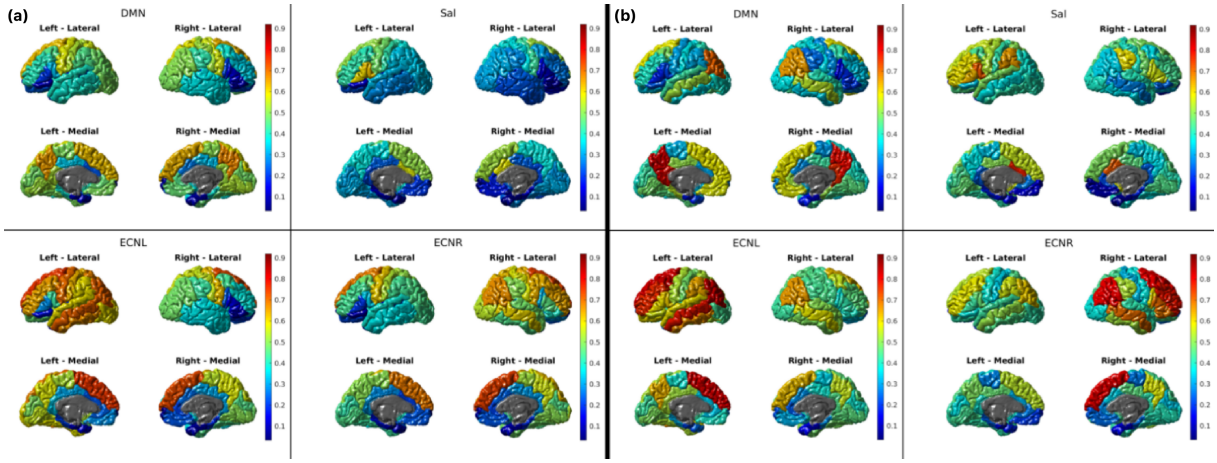

Figure B.9: Default mode network (DMN), Salience network (Sal), External control network left and right (ECNL, ECNR)

3. Probabilistic tractography - counts

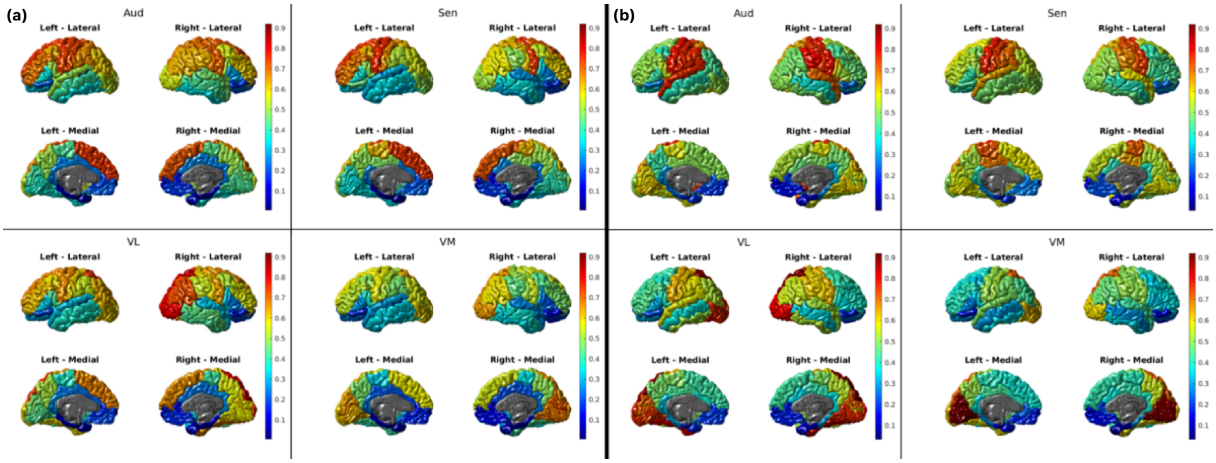

Figure B.10: Auditory network (Aud), Sensorimotor network (Sen), Visual lateral, medial networks (VL, VM) obtained from the simulated (at T_c) and the empirical correlations. RSNs for other tractography methods are presented in Appendix C

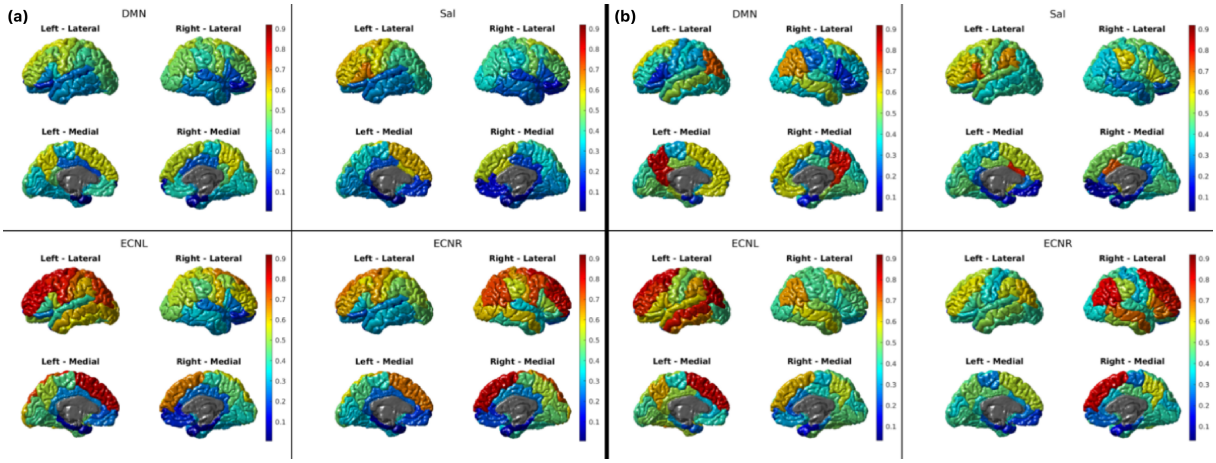

Figure B.11: Default mode network (DMN), Salience network (Sal), External control network left and right (ECNL, ECNR)

4. Probabilistic tractography - FA

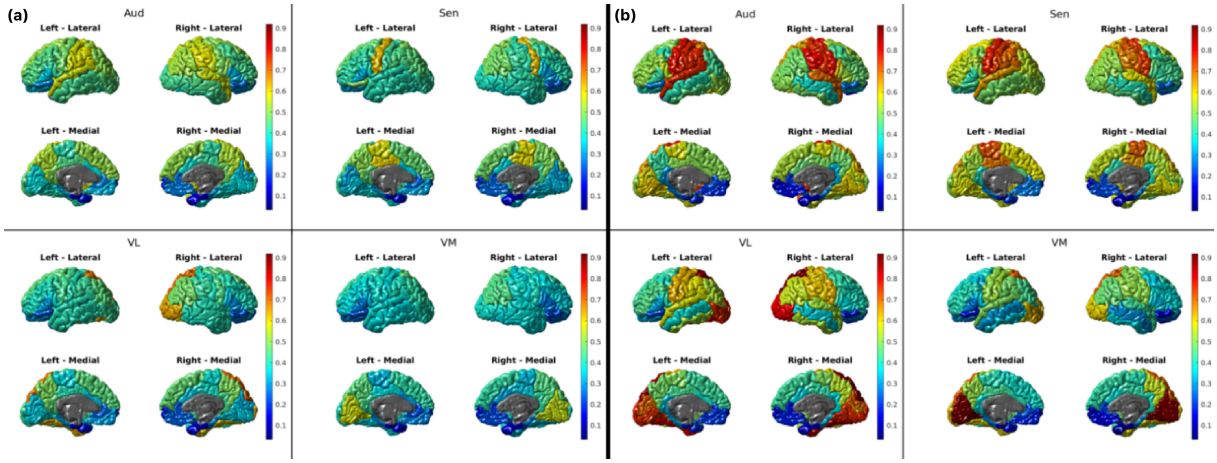

Figure B.12: Auditory network (Aud), Sensorimotor network (Sen), Visual lateral, medial networks (VL, VM) obtained from the simulated (at T_c) and the empirical correlations. RSNs for other tractography methods are presented in Appendix C

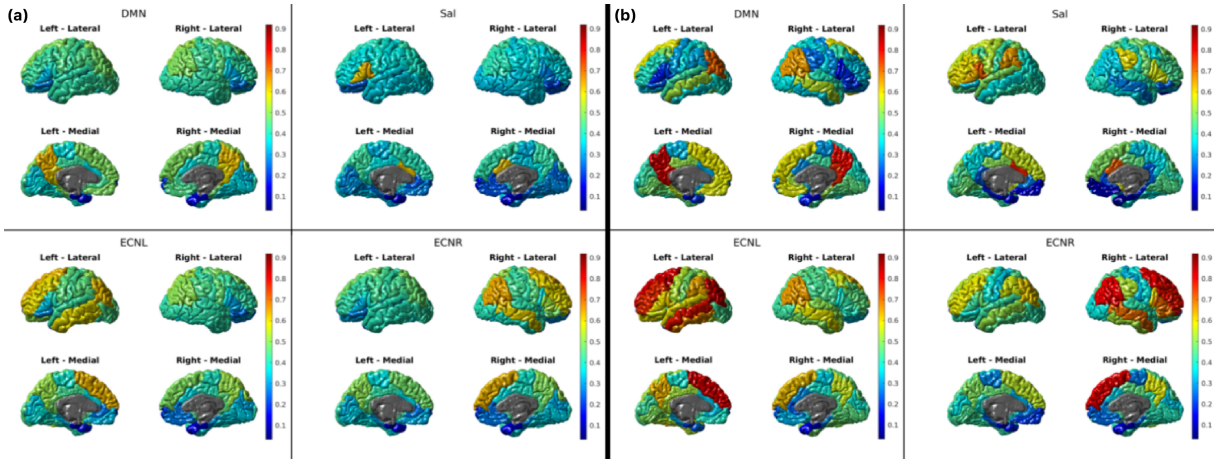

Figure B.13: Default mode network (DMN), Salience network (Sal), External control network left and right (ECNL, ECNR)

5. Probabilistic tractography - counts weighted by FA

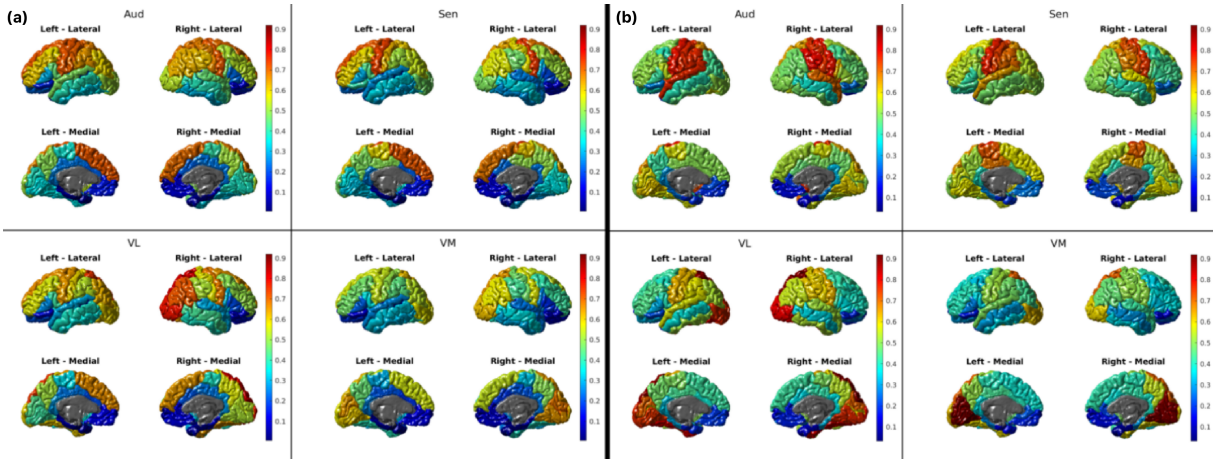

Figure B.14: Auditory network (Aud), Sensorimotor network (Sen), Visual lateral, medial networks (VL, VM) obtained from the simulated (at T_c) and the empirical correlations. RSNs for other tractography methods are presented in Appendix C

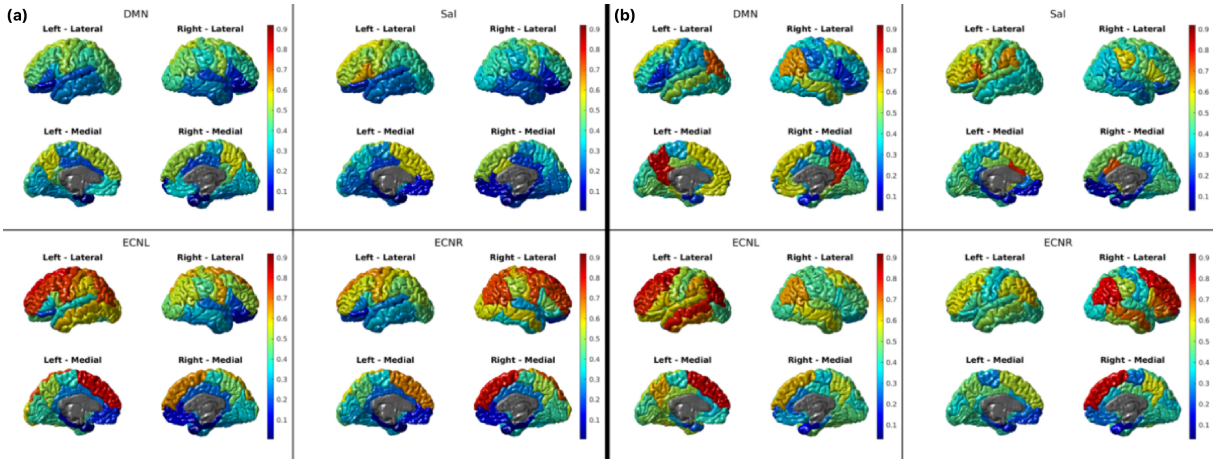

Figure B.15: Default mode network (DMN), Salience network (Sal), External control network left and right (ECNL, ECNR)

Bibliography

[1] David P Landau and Kurt Binder. *A guide to Monte Carlo simulations in statistical physics*. Cambridge University Press, 2014.

[2] H Eugene Stanley. *Phase transitions and critical phenomena*. Clarendon Press, Oxford, 1971.

Appendix C

Appendices: Chapter 4

C.1 Supplementary figures

1.Auditory network

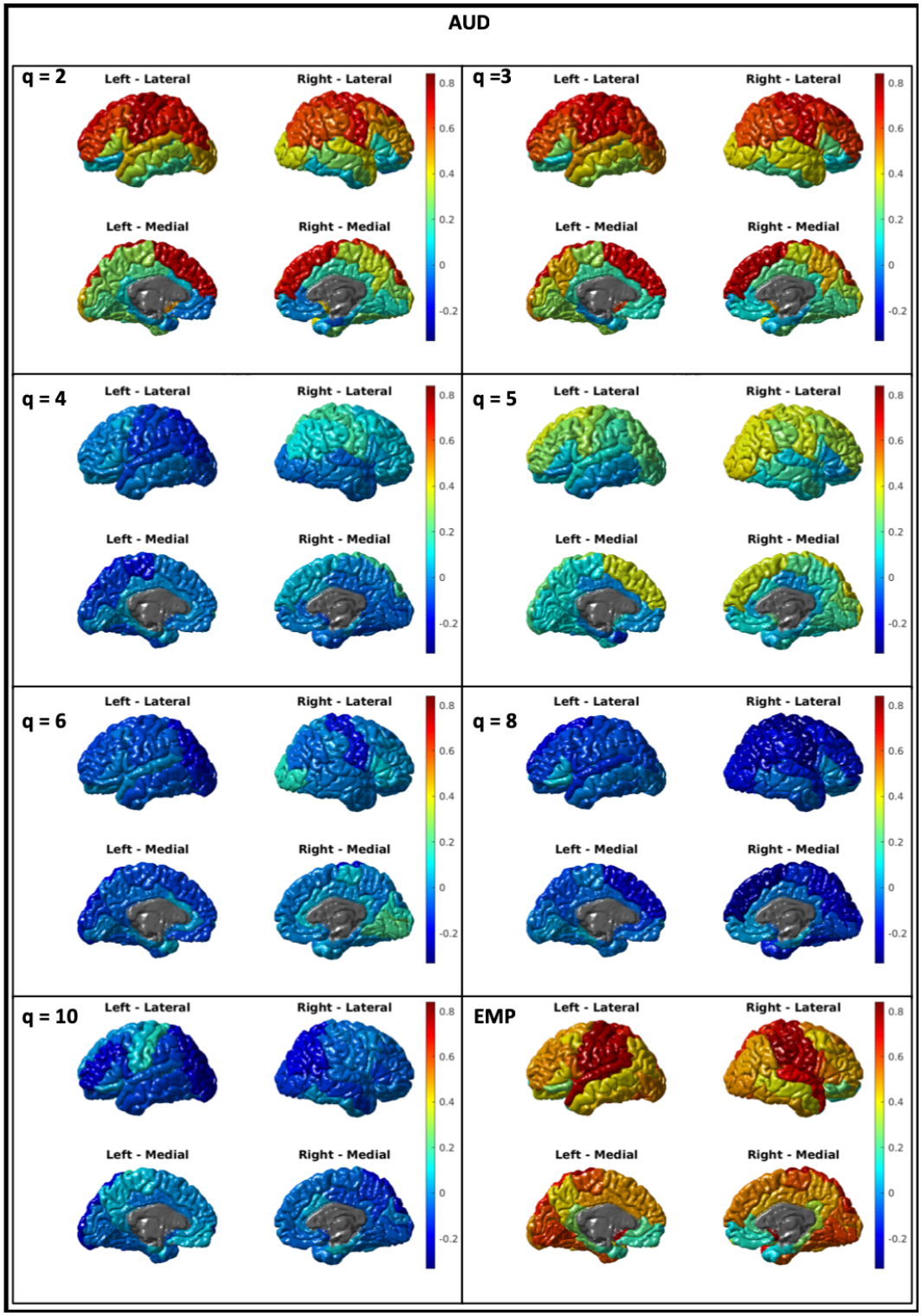

Figure C.1: Brain maps for the auditory network from simulated data at T_c for seven models together with the brain map for the empirical data

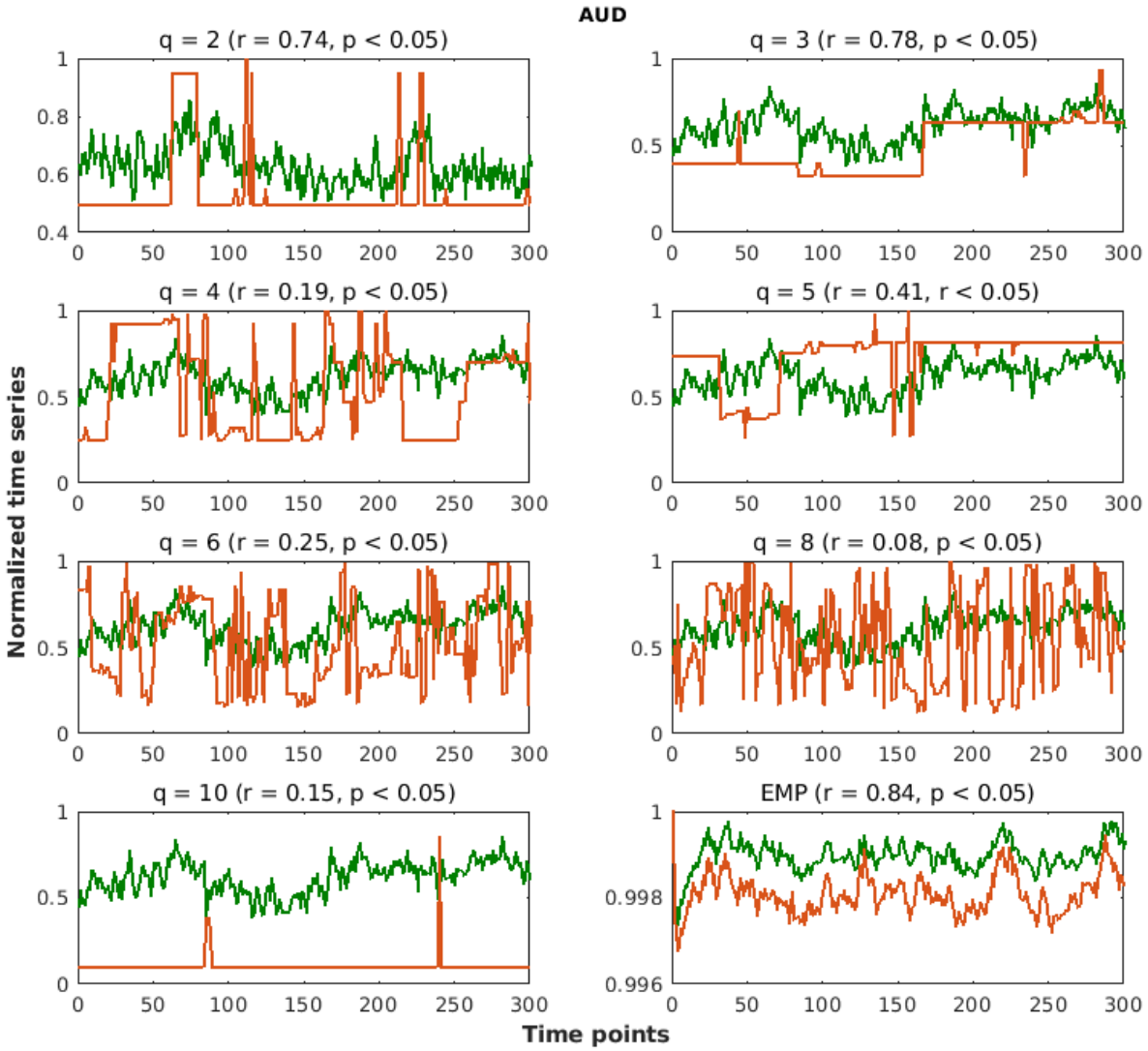

Figure C.2: Average time series for the DMN is presented in green while the time series of the region that has the highest correlation with the average time series is presented in orange for all the models and the empirical data

2. Executive control network left

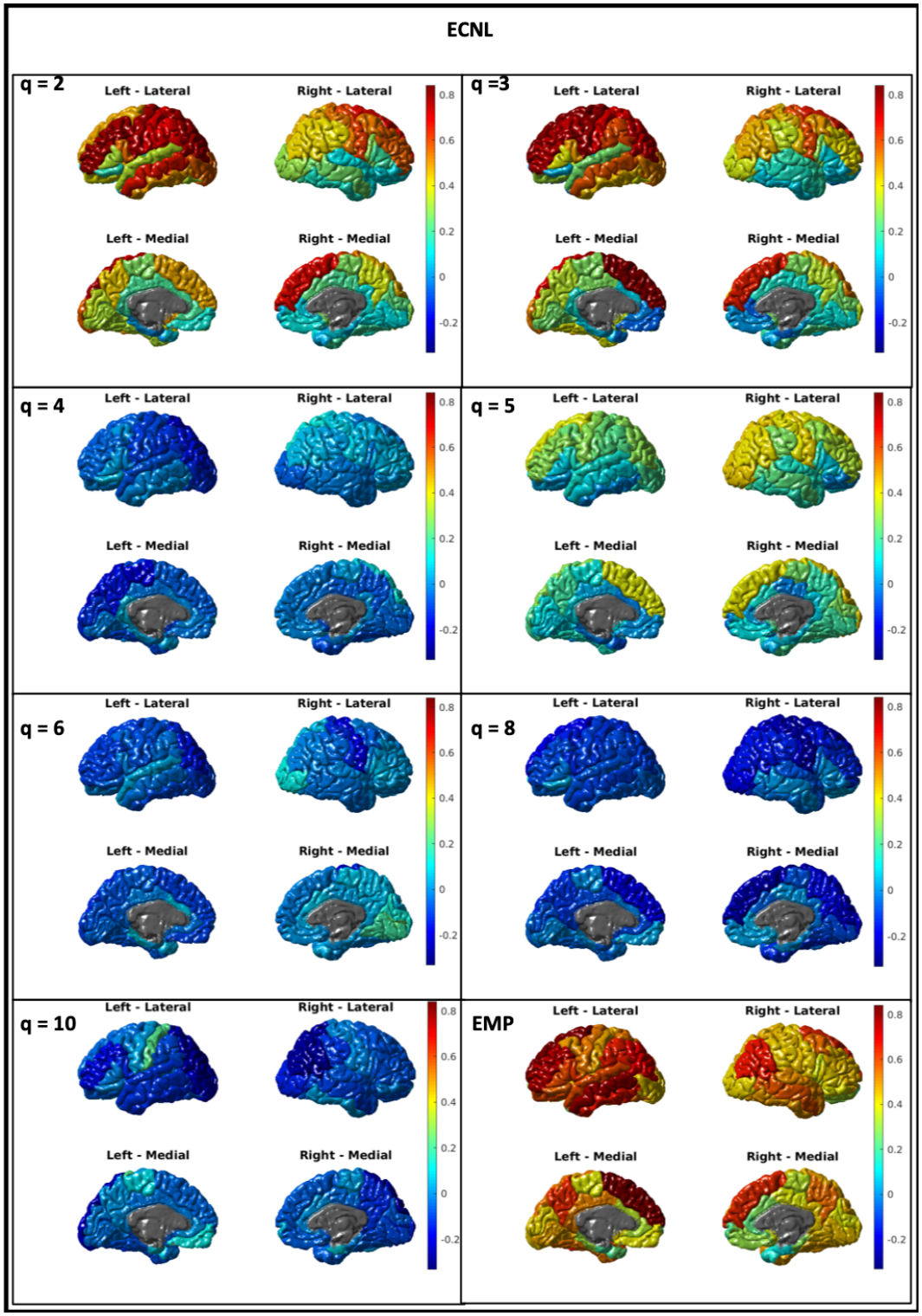

Figure C.3: Brain maps for the executive control network left from simulated data at T_c for seven models together with the brain map for the empirical data

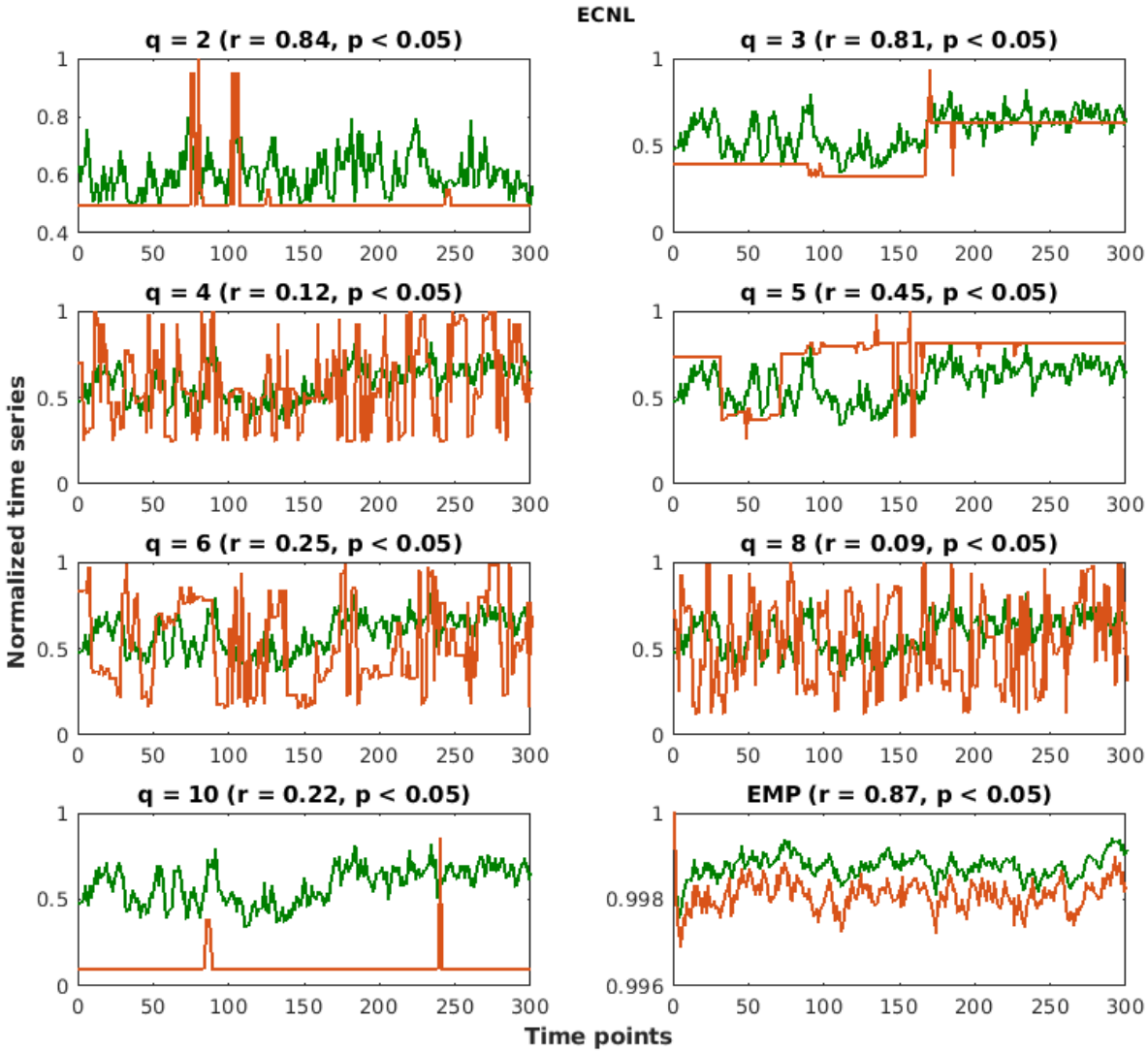

Figure C.4: Average time series for the DMN is presented in green while the time series of the region that has the highest correlation with the average time series is presented in orange for all the models and the empirical data

3. Executive control network right

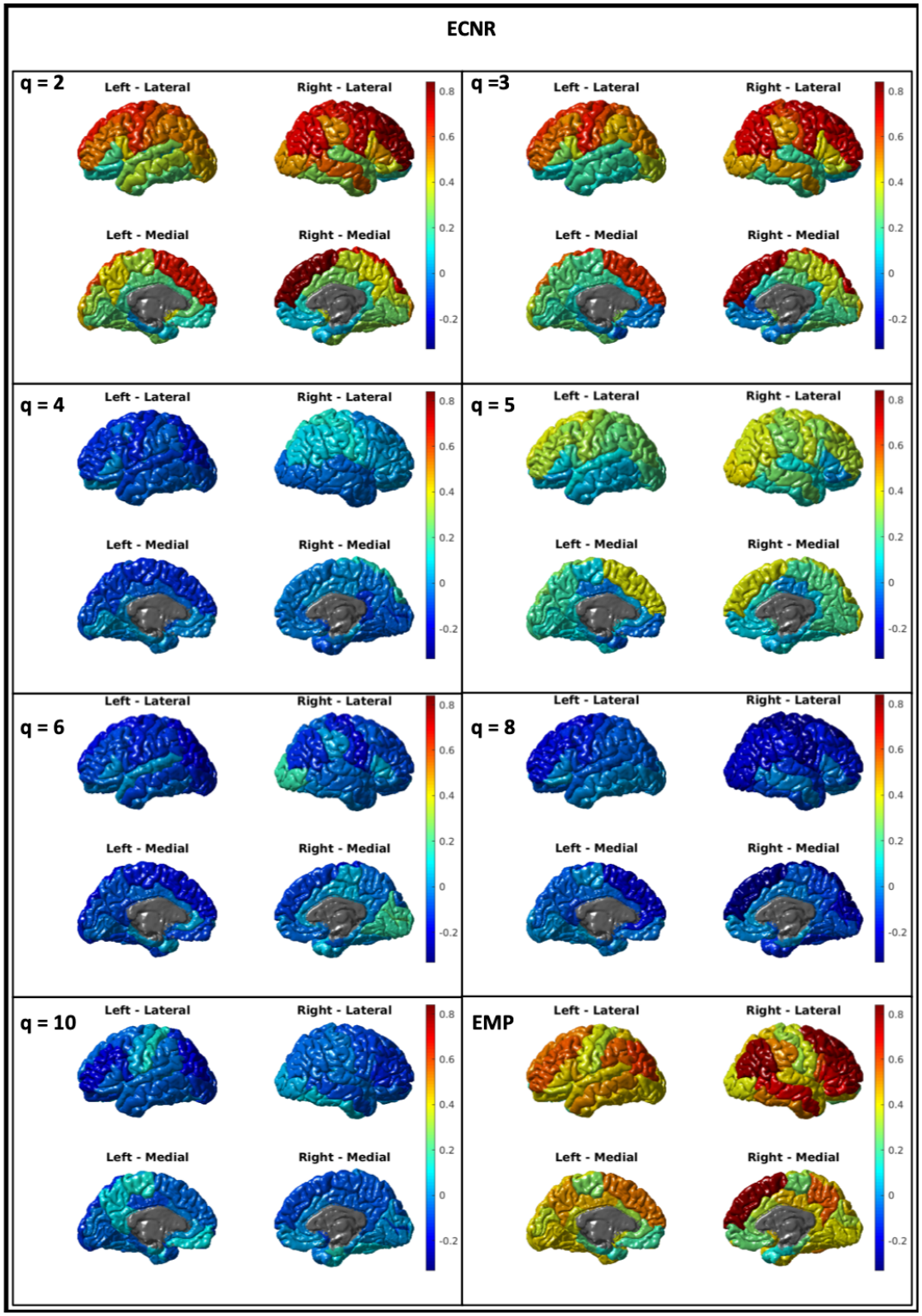

Figure C.5: Brain maps for the executive control network right from simulated data at T_c for seven models together with the brain map for the empirical data

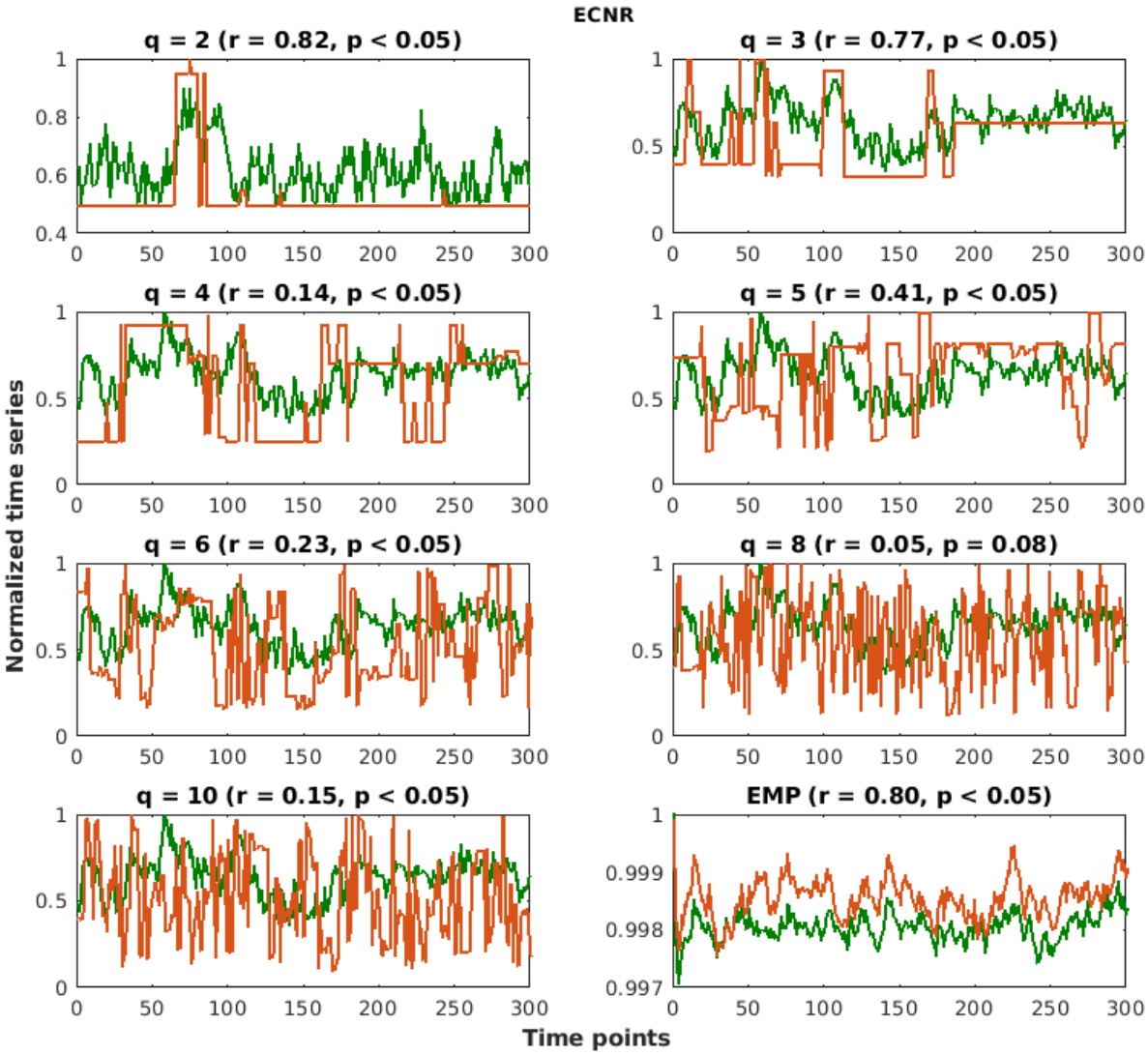

Figure C.6: Average time series for the DMN is presented in green while the time series of the region that has the highest correlation with the average time series is presented in orange for all the models and the empirical data

4. Salience network

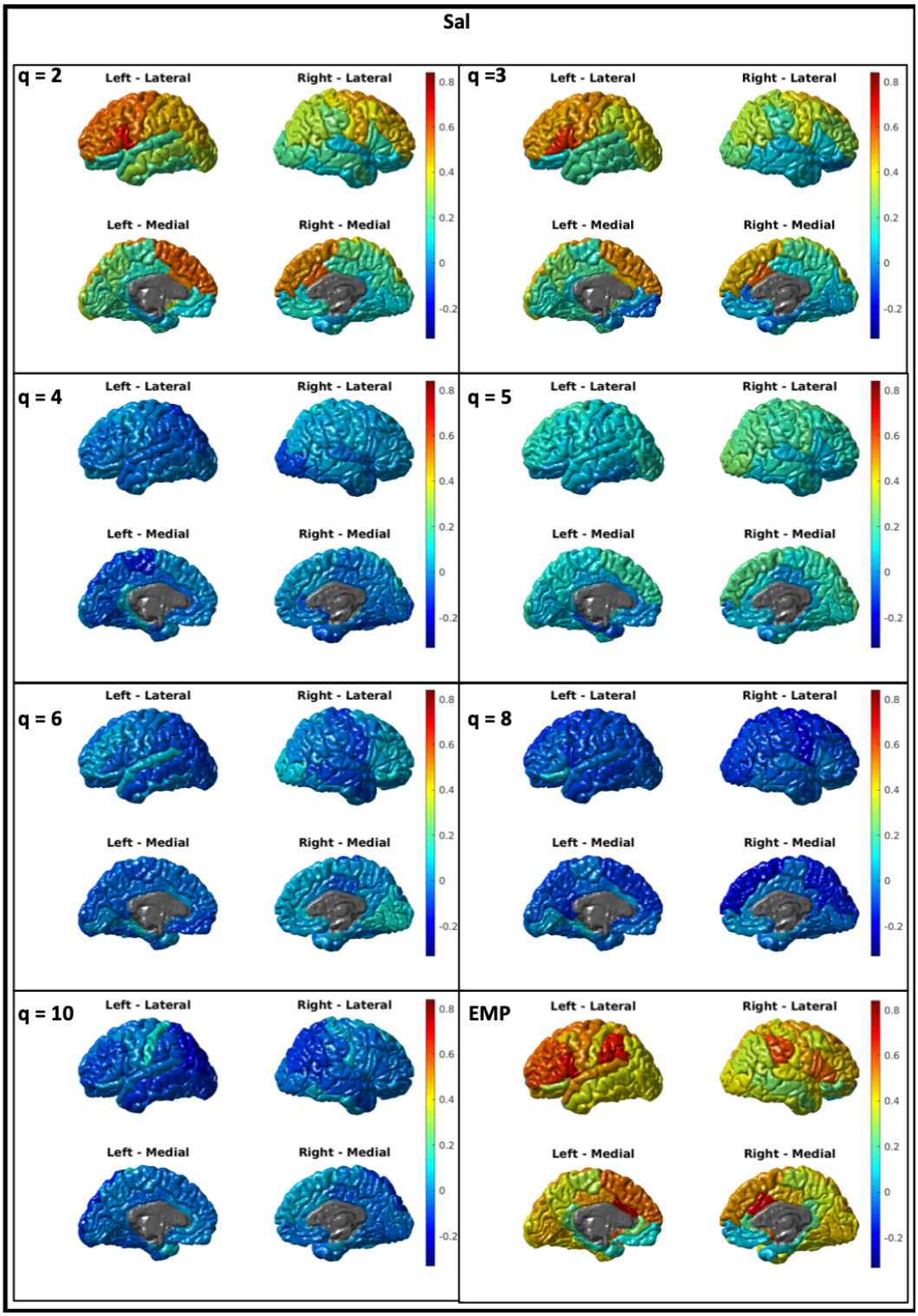

Figure C.7: Brain maps for the salience network from simulated data at T_c for seven models together with the brain map for the empirical data

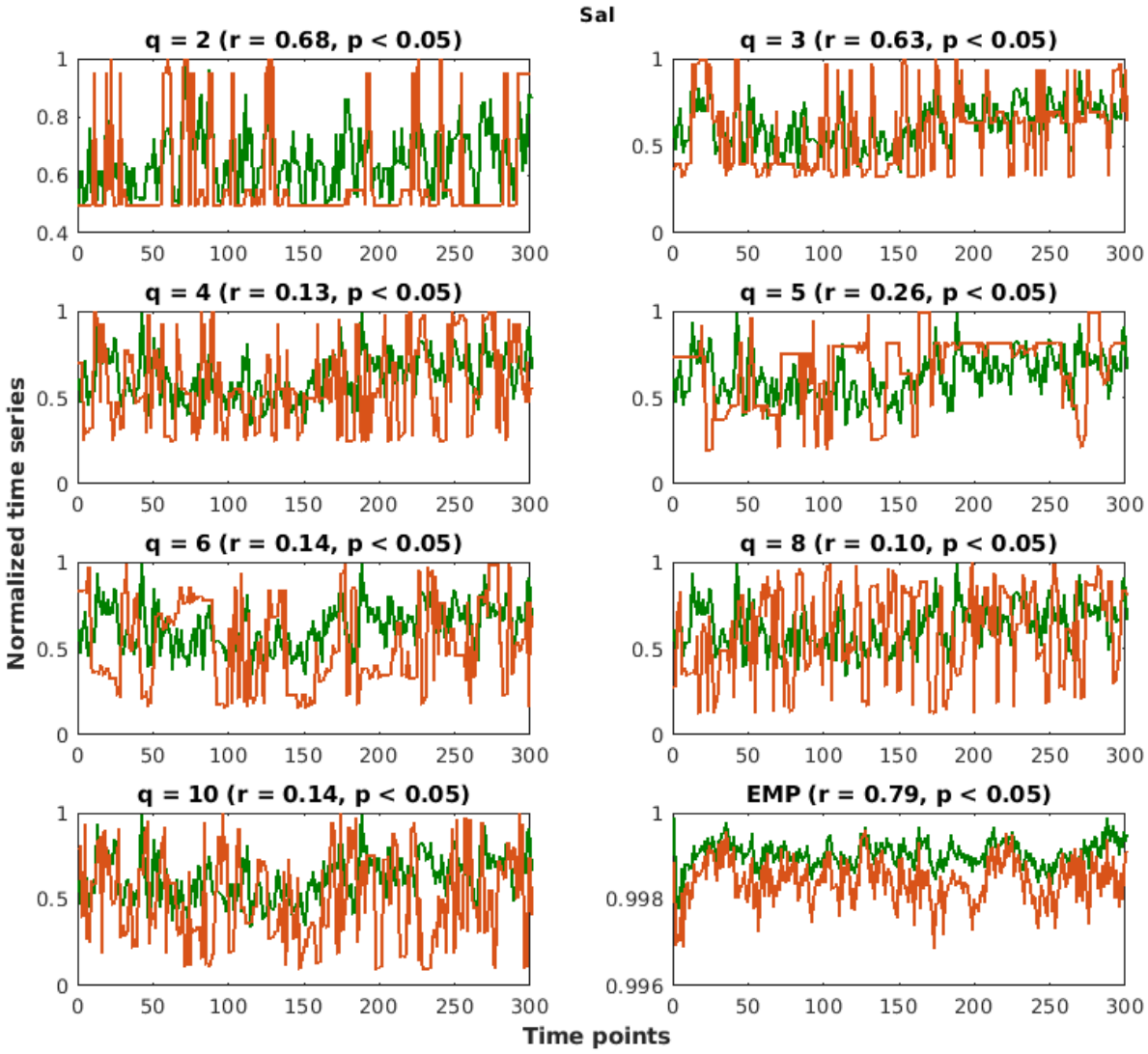

Figure C.8: Average time series for the DMN is presented in green while the time series of the region that has the highest correlation with the average time series is presented in orange for all the models and the empirical data

5. Sensorimotor network

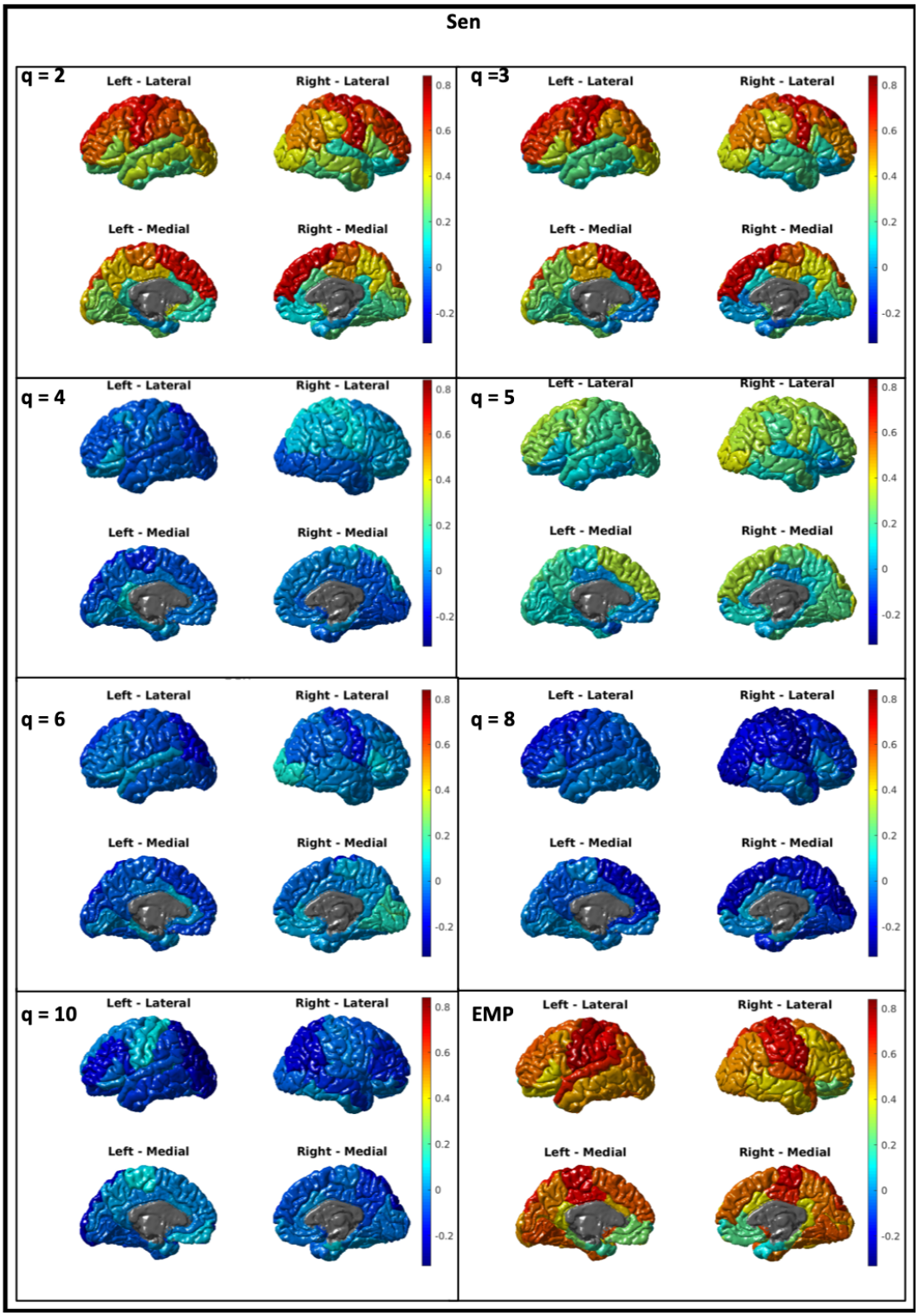

Figure C.9: Brain maps for the sensorimotor network from simulated data at T_c for seven models together with the brain map for the empirical data

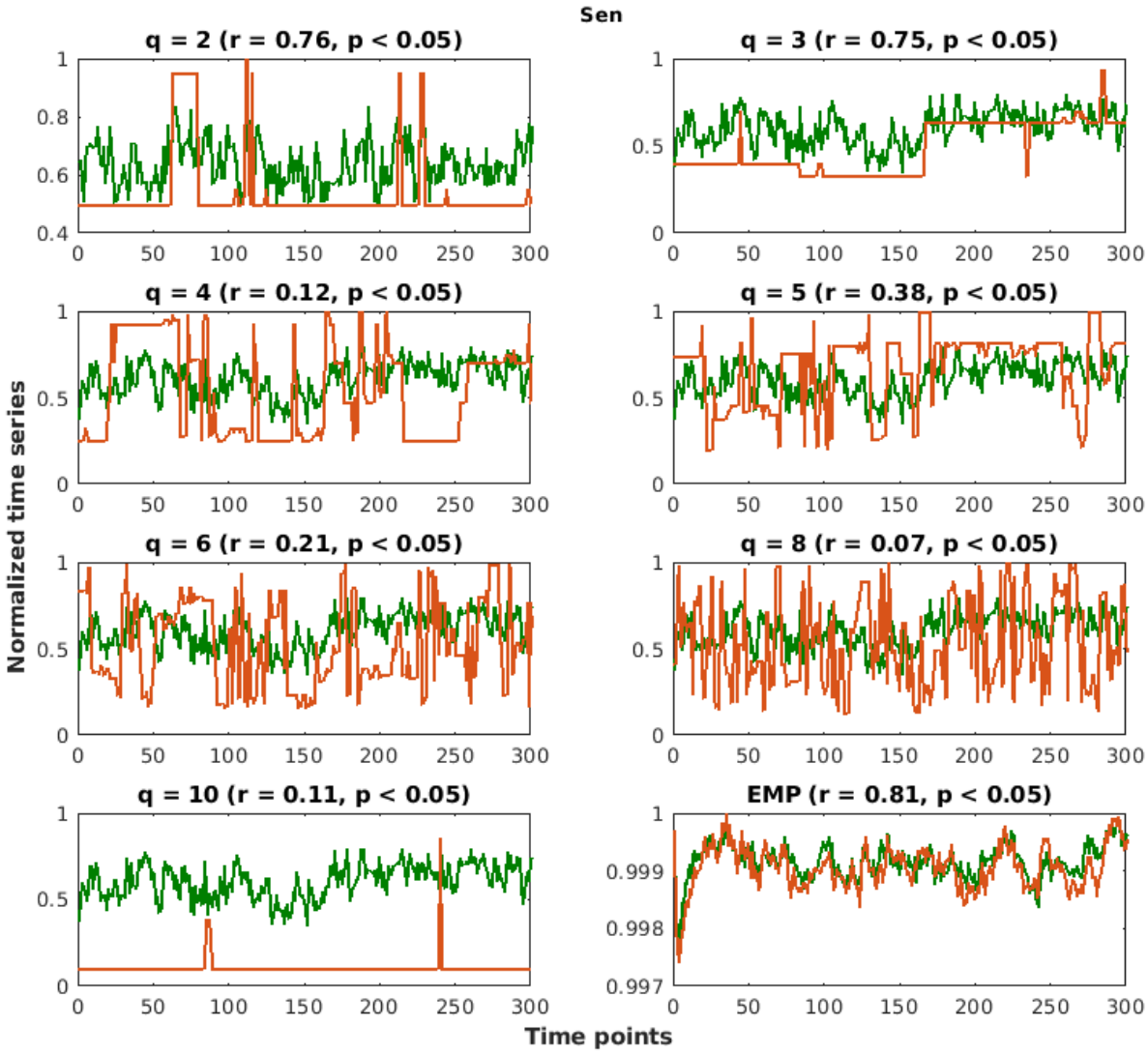

Figure C.10: Average time series for the DMN is presented in green while the time series of the region that has the highest correlation with the average time series is presented in orange for all the models and the empirical data

6. Visual lateral network

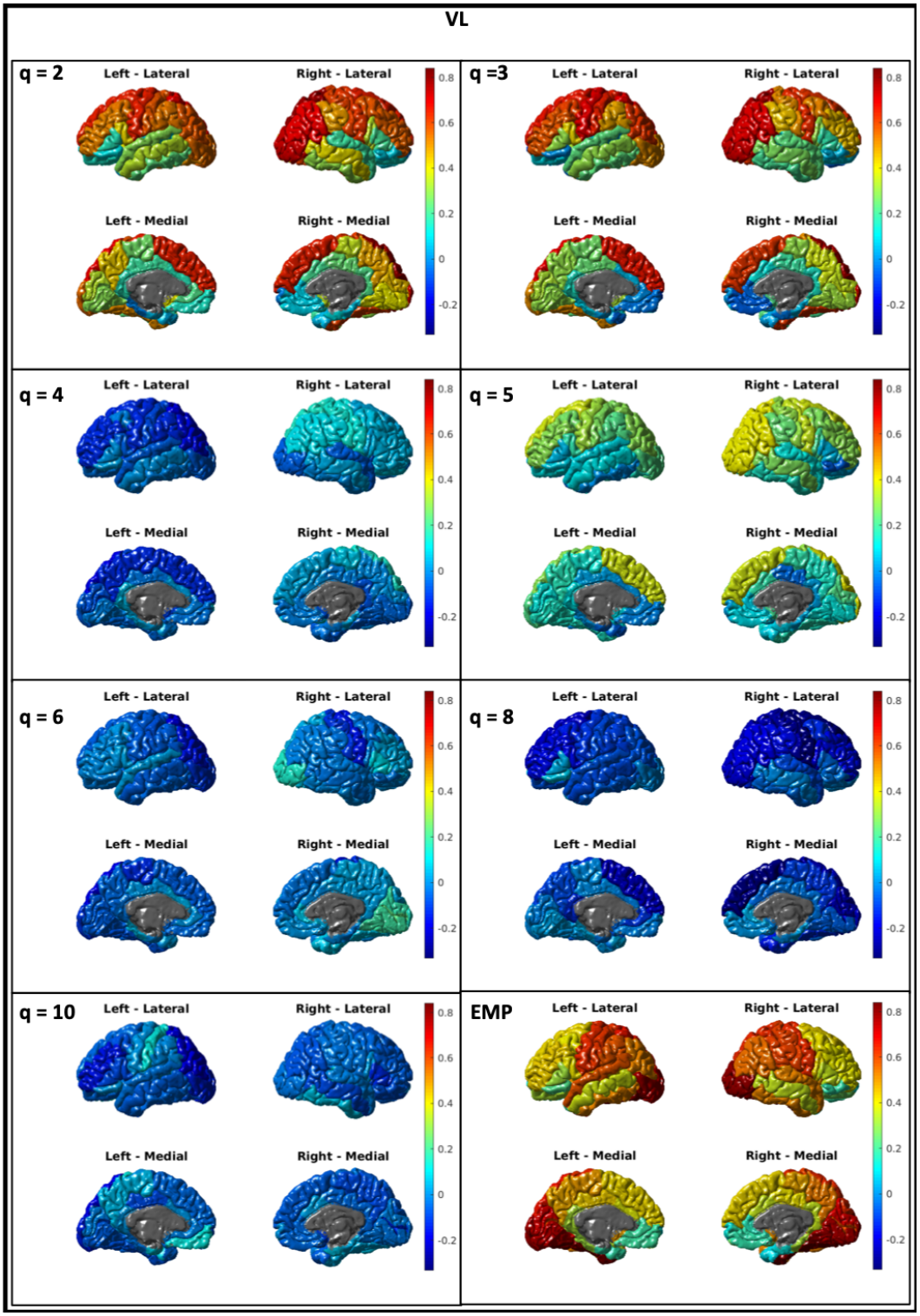

Figure C.11: Brain maps for the visual lateral network from simulated data at T_c for seven models together with the brain map for the empirical data

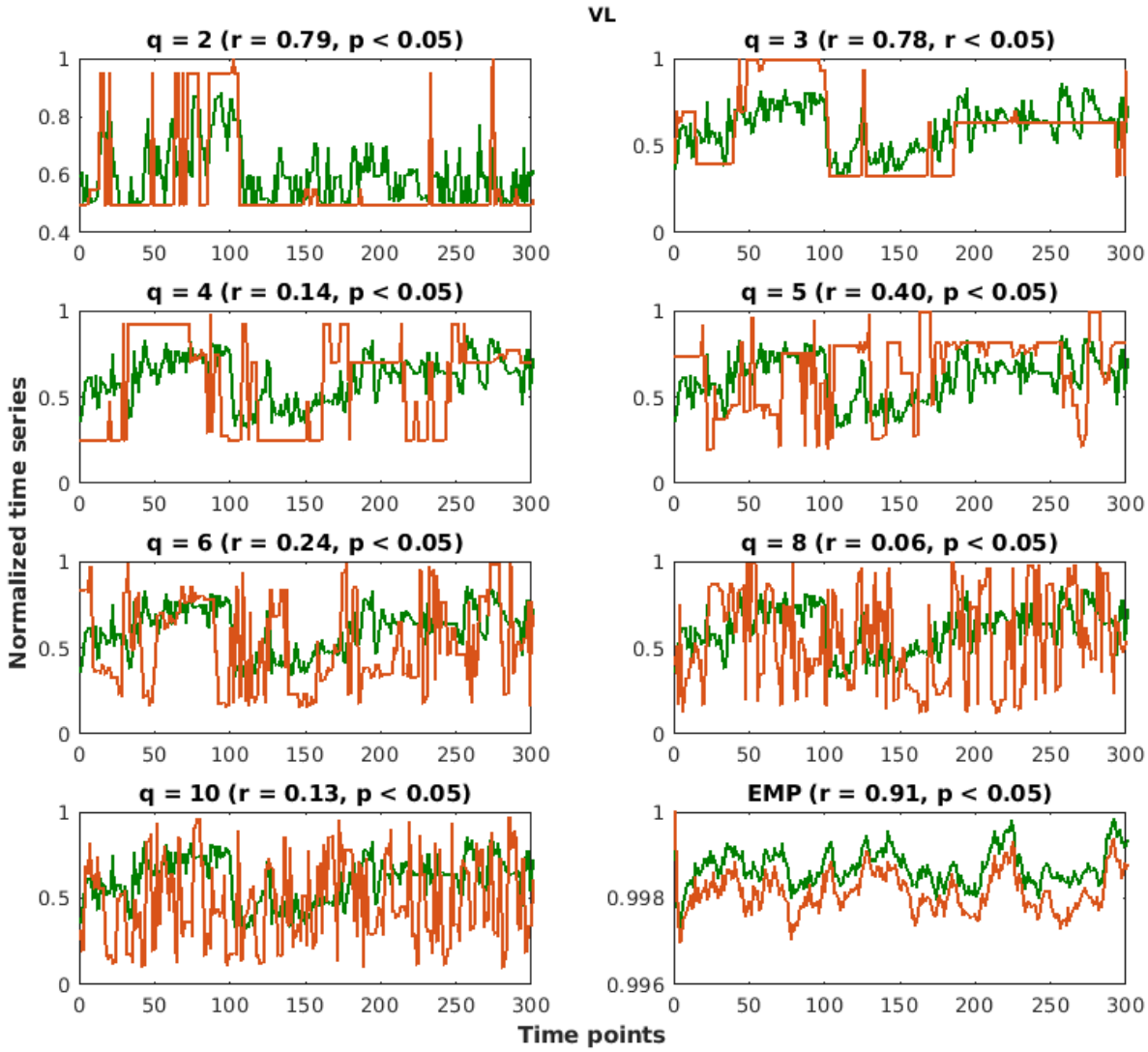

Figure C.12: Average time series for the DMN is presented in green while the time series of the region that has the highest correlation with the average time series is presented in orange for all the models and the empirical data

7. Visual medial network

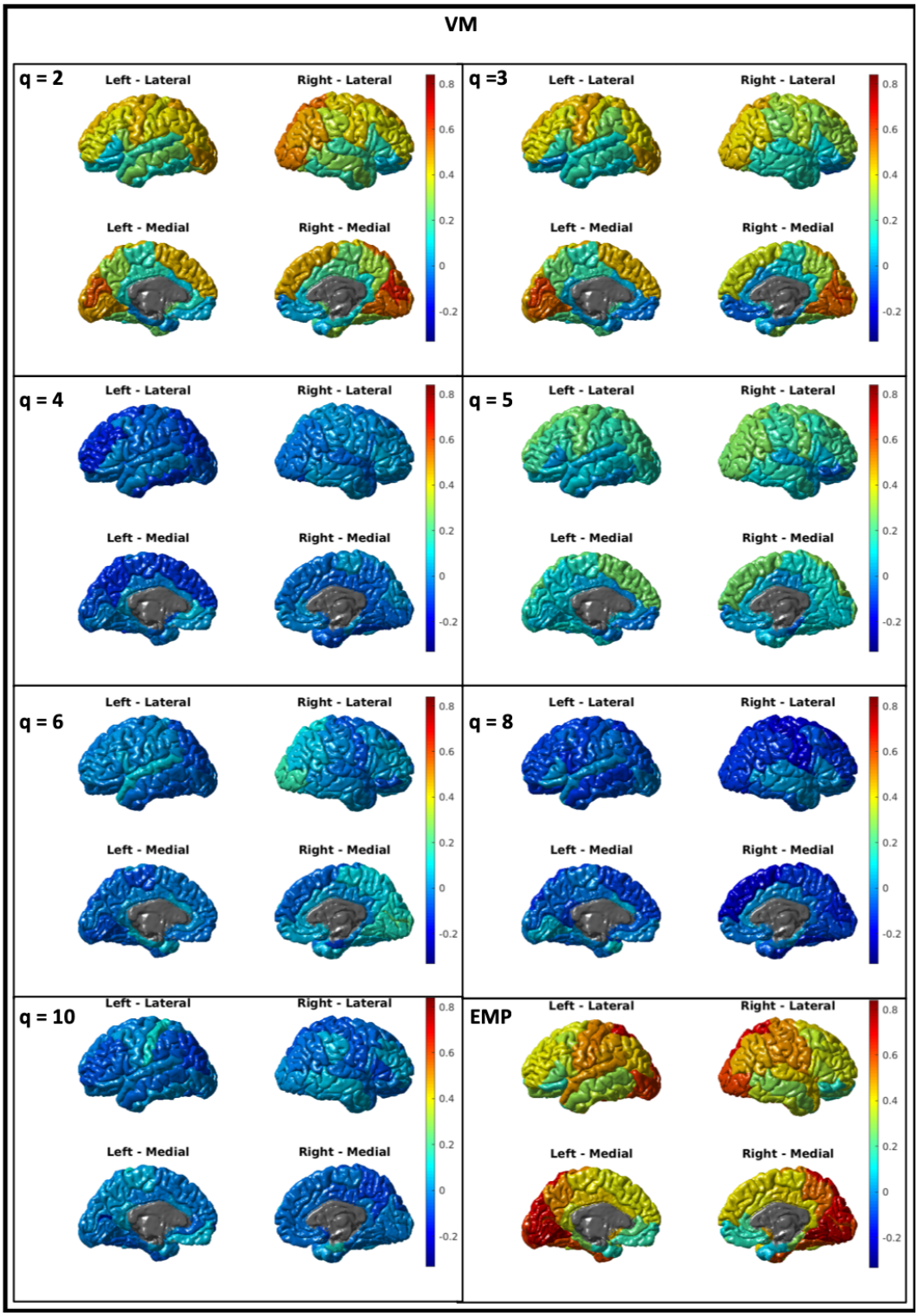

Figure C.13: Brain maps for the visual medial network from simulated data at T_c for seven models together with the brain map for the empirical data

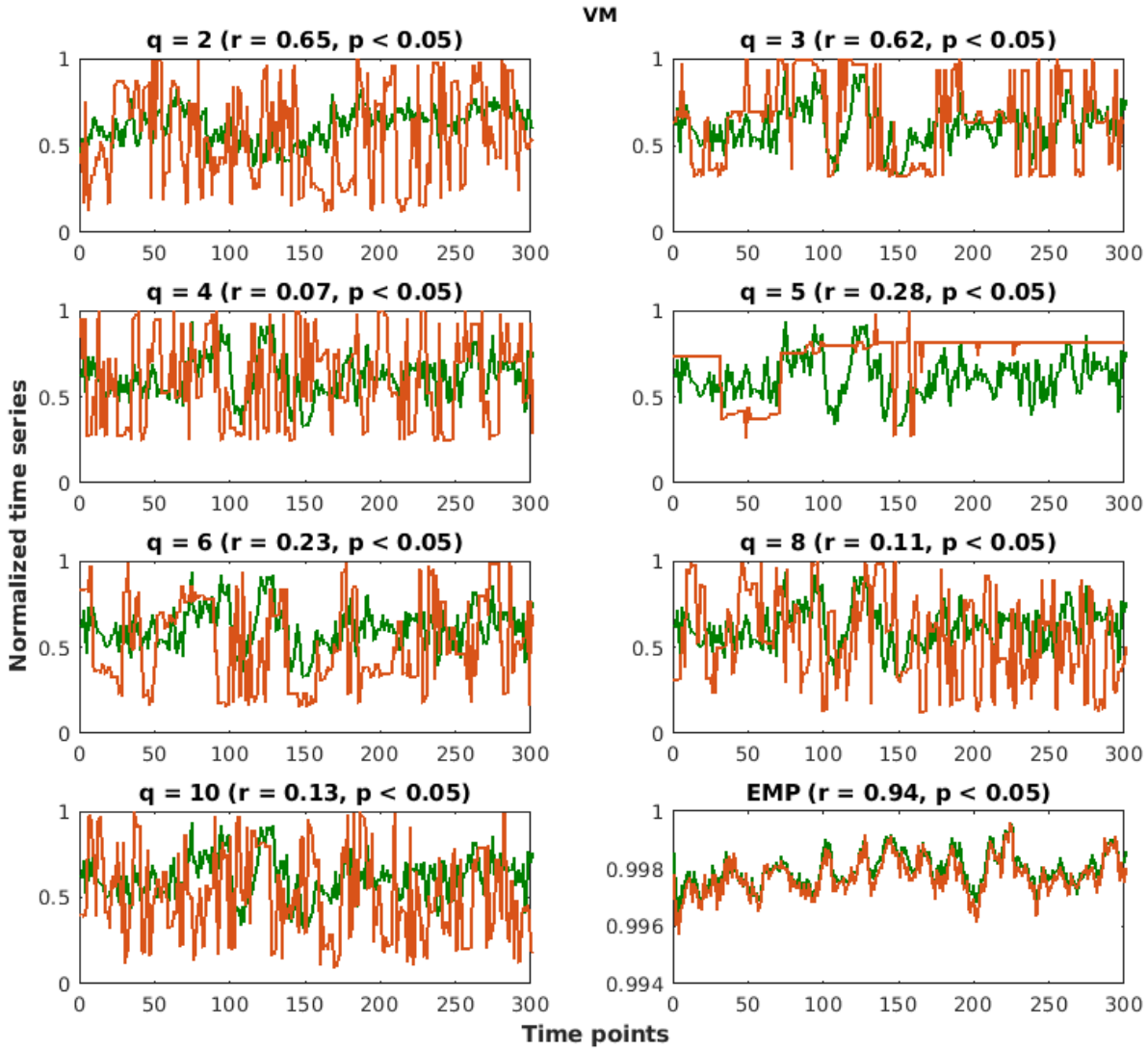

Figure C.14: Average time series for the DMN is presented in green while the time series of the region that has the highest correlation with the average time series is presented in orange for all the models and the empirical data

8. Visual occipital network

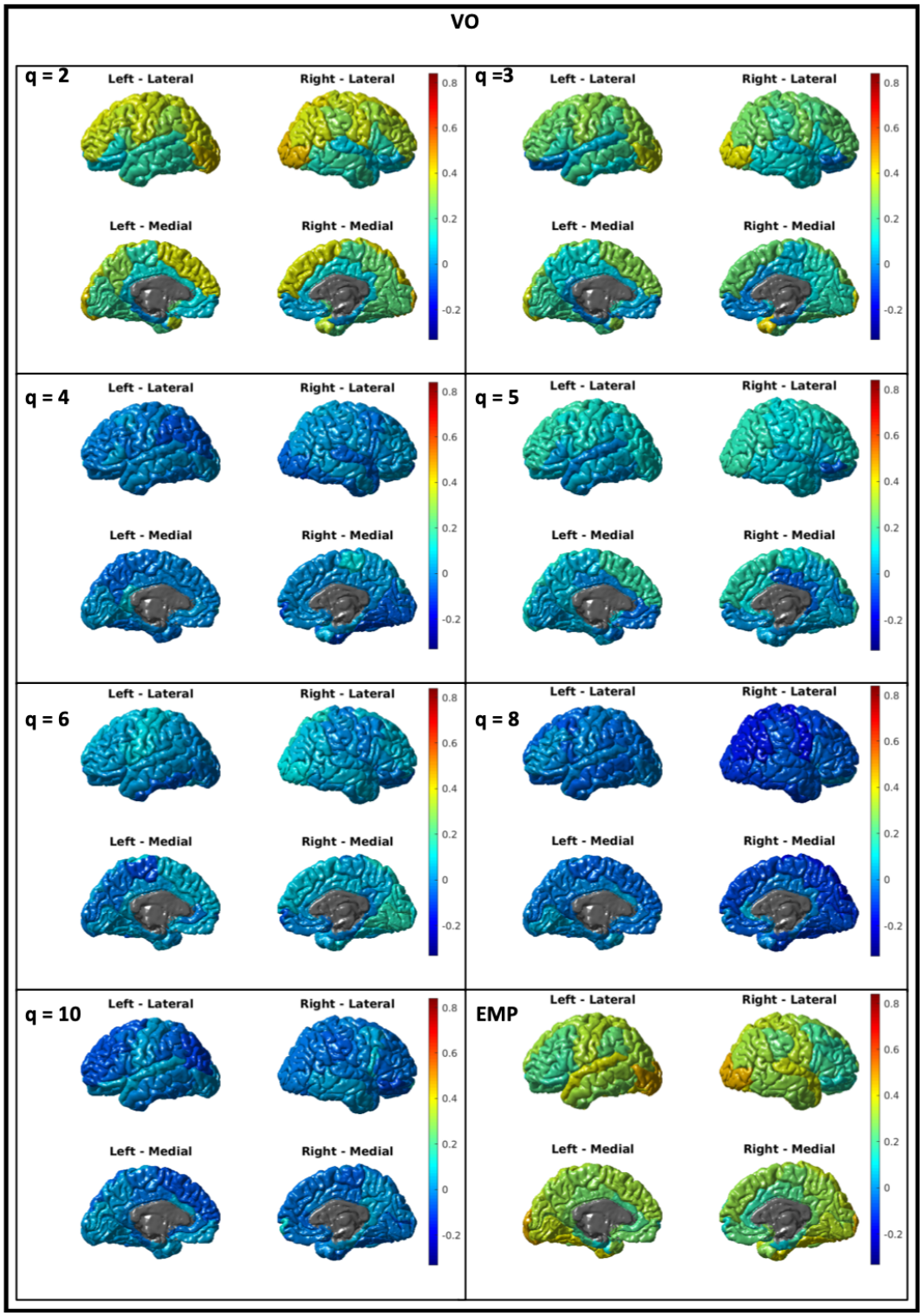

Figure C.15: Brain maps for the visual occipital network from simulated data at T_c for seven models together with the brain map for the empirical data

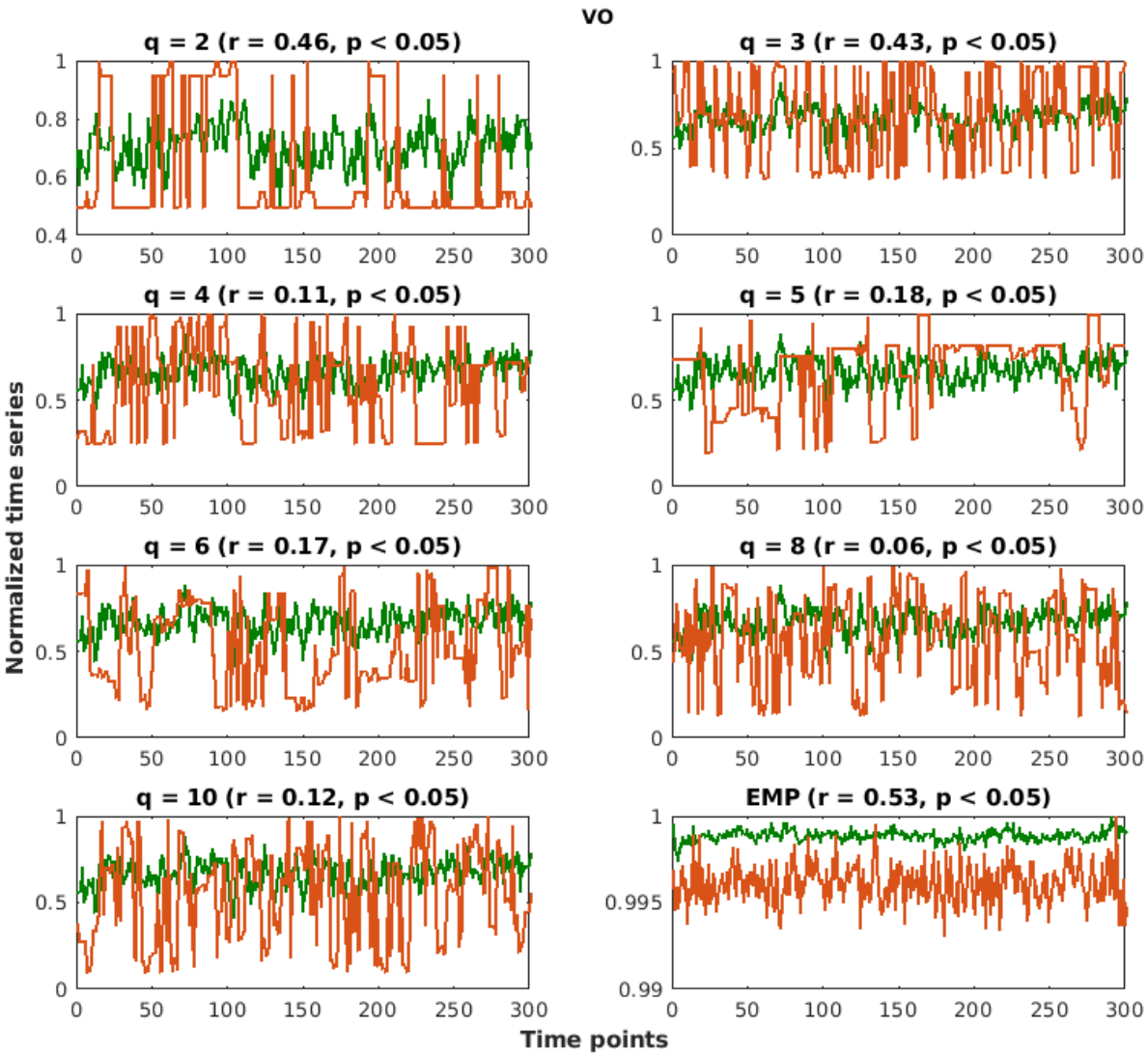

Figure C.16: Average time series for the DMN is presented in green while the time series of the region that has the highest correlation with the average time series is presented in orange for all the models and the empirical data

Curriculum Vitae

Name:	Pubuditha Abeyasinghe
Post-Secondary Education and Degrees:	University of Western Ontario, Canada Ph.D. in Physics 2015 - 2019
	University of Western Ontario, Canada M.Sc. in Physics 2013 - 2015
	University of Sri Jayawardenapura, Sri Lanka B.Sc, Honours degree in Physics (First Class) 2008 - 2012
Honours and Awards:	*Erasmus+ Scholarship* Radbound University, The Netherlands 2018
	Society of Graduate Studies Travel Award The University of Western Ontario, Canada 2018
	Mitacs Globalink Research Award Mitacs, Canada 2017
	Western Graduate Research Scholarship (WGRS) The University of Western Ontario, Canada 2013 - 2019
Related Work Experience:	Teaching Assistant The University of Western Ontario, Canada 2013 - 2019

Research Assistant
The University of Western Ontario, Canada
2013 - 2019

Publications

Abeyasinghe, P.M., de Paula, D.R., Khajehabdollahi, S., Valluri, S.R., Owen, A.M. and Soddu, A., 2018. Role of Dimensionality in Predicting the Spontaneous Behavior of the Brain Using the Classical Ising Model and the Ising Model Implemented on a Structural Connectome. Brain connectivity, 8(7), pp.444-455.

Ribeiro de Paula, D., Ziegler, E., Abeyasinghe, P.M., Das, T.K., Cavaliere, C., Aiello, M., Heine, L., Di Perri, C., Demertzi, A., Noirhomme, Q. and CharlandVerville, V., 2017. A method for independent component graph analysis of restingstate fMRI. Brain and behavior, 7(3), p.e00626.

Abeyasinghe, P.M., Structure-Function Relationship of the Brain: A comparison between the 2D Classical Ising model and the Generalized Ising model, 2015.

Das, T.K., Abeyasinghe, P.M., Crone, J.S., Sosnowski, A., Laureys, S., Owen, A.M. and Soddu, A., 2014. Highlighting the structure-function relationship of the brain with the Ising model and graph theory. BioMed research international, 2014.

Oral presentations

Restoring the functions of the damaged brain, 3-minute thesis presentation presented for the 3MT competition, 2019 March, The Western University, London, ON (one of the 20 finalists in the university competition).

PM Abeyasinghe, Potts Model with Different Spin States, Simulated on a Structural Connectome to Model the Structure- Function relationship of the Human Brain. Presented at: APS April meeting, 2018 April, Columbus, OH.

PM Abeyasinghe, Generalized Ising model and the Dimensionality of the Brain. Presented at: CAP Congress, 2017 May, Queens University, Kingston, ON.

PM Abeyasinghe, Structure-Function relationship of the Brain, 3-minute thesis presentation presented for the 3MT competition, 2016 March, The Western University, London, ON (one of the 20 finalists in the university competition).

PM Abeyasinghe, Modeling the Structure-Function relationship of the brain using the generalized Ising model. Presented at: The interdisciplinary research showcase, 2015 December, The Western University, London, ON. (3-minute thesis presentation).

Poster presentation

Pubuditha M. Abeyasinghe, Marco Aiello, Carlo Cavaliere, Adrian M. Owen, Andrea Soddu. Comparing different methods of DTI-based tractography using the generalized Ising model. Poster presented at the Fallona family interdisciplinary research showcase, 2018 April, The Western University, London, ON.

PM Abeyasinghe, TK Das, DR Paula, AM Owen and A Soddu. Modeling the Relationship between the Anatomical Structure and the Functional Connectivity of the Brain. Poster presented at: The Society of Neuroscience conference: Engineering the Brain: Technologies for Neurobiological Applications, 2015 October, Chicago, IL.

PM Abeyasinghe, DR Paula, S Laureys, AM Owen, TK Das and A Soddu. Modeling the Relationship between the Anatomical Structure and the Functional Connectivity of the Brain. Poster session presented at: The inaugural Brain and Mind Institute symposium, 2015 September, The Western University, London, ON.

PM Abeyasinghe, DR Paula, S Laureys, AM Owen, TK Das and A Soddu. Modeling the Relationship between the Anatomical Structure and the Functional Connectivity of the Brain. Poster session presented at: The interdisciplinary research showcase, 2014 December, The Western University, London, ON.

TK Das, PM Abeyasinghe, A Sosnowski, S Khajehabdollahi, B Ge, S Laureys, AM Owen and A Soddu. Modeling Functional Organizations of the Resting Brain using the Anatomical Structure. Poster session presented at: 34th Annual meeting of the Southern Ontario Neuroscience Association (SONA), 2014 May, The Western University, London, ON.